Title
Metal Oxides for Solid State Electronics: Transparent Electrodes, Photoanodes and Transistors

Author
Park, Hyun Sung

Publication Date
2017

Peer reviewed|Thesis/dissertation

Metal Oxides for Solid State Electronics: Transparent Electrodes, Photoanodes and Transistors

By

Hyun Sung Park

A dissertation submitted in partial satisfaction of the

requirements for the degree of

Doctor of Philosophy

in

Engineering – Mechanical Engineering

in the

Graduate Division

of the

University of California, Berkeley

Committee in charge:

Professor Liwei Lin, Chair
Professor Costas P. Grigoropoulos
Professor Jie Yao

Summer 2017

Abstract
Metal Oxide for Solid State Electronics: Transparent Electrodes, Photoanodes and Transistors

by
Hyun Sung Park
Doctor of Philosophy in Engineering - Mechanical Engineering
University of California, Berkeley
Professor Liwei Lin, Chair

Metal oxides have unique characteristics for a variety of modern applications such as thin films and nano-structured materials in optoelectronic devices and renewable energy productions. In this dissertation, three different metal oxides are developed: solution processed antimony doped tin oxide (ATO) thin films for transparent electrodes; high aspect-ratio ZnO nanowires with ALD (Atomic Layer Deposition) TiO_2 for stabilizations as photo-anodes; and spin-coated SnO_2 films for TFTs (Thin Film Transistors) in the applications of display devices.

In the first part of this dissertation, solution processed ATO electrodes show high conductivity (~21000 S/m) and optical transparency (~95%) suitable for the state-of-art optoelectronic devices such as displays, solar cells, and smart windows. The high quality thin films are made by the low-cost solution-based process with multiple spin-coating steps using sol-gel precursors. In order to obtain better electrical and optical performances, a parametric study has been performed on four key processing parameters: doping concentration, film thickness, ambient gases and temperatures. Studies on the film surface morphology using scanning electron microscopy together with electrical, and optical characterizations elucidate the dominant factors for the conductivity and transmittance of the films. Further examinations under X-ray photoelectron spectroscopy reveal the required annealing temperature to form Sb^{+5} species in the Sn^{+4} lattices. It is found that improved mechanical flexibility is achieved and the elastic modulus of 35GPa is obtained by using the nano-indentation test. A 3D finite element analysis shows ATO films can resist 4x more deformation than those of commercial vacuum-processed indium tin oxide (ITO) films under the four-point bending simulations.

The high aspect-ratio and vertically ordered ZnO nanowires as long as 10μm in length and 50nm in the cross-sectional width are constructed by using a hydrothermal process. A conformal TiO_2 film of 40nm in thickness is deposited afterwards by ALD to stabilize the ZnO nanowires in a solar-powered hydrogen gas harvester. Two key innovations have been achieved using the favorable geometry and high quality nanowires in this work: (1) improved stability over bare ZnO nanowires during the photocatalytic reactions, and (2) excellent low bias voltages.

In the work of using SnO_2 films to make TFTs for display devices, a multiple spin coating is developed in order to obtain better gate modulation properties. The effects of annealing condition on the electrical performances and the surface morphologies of TFTs have been investigated. Experimentally, a value of 6.3cm^2/Vs of the extracted field effect mobility for solution processed SnO_2 TFTs has been achieved and this value is 6x higher than that of a-Si:H TFTs.

ACKNOWLEDGEMENTS

I would like to express my deepest gratitude to my parents and mother-in-law, Jong-nam Park, Insook Choi, and Heesoon Kim. Without their support and encouragement, I could not have completed my Ph.D. degree. I also deeply appreciate my wife, Kyung Sook Kim, whose love, endurance, and support were undeniably the bedrock upon which the past ten years of my life have been built. My children, Sihyun and Siwoo, always have given me much happiness and positive energy to finish this long journey.

My sincerest appreciation goes to my adviser, Prof. Liwei Lin. His guidance was paramount in providing well-rounded experience consistent with my long-term career goals. He always encouraged me with warm and kind words to be an independent thinker. I am also grateful to the members of my committee, Professor Costas P. Grigoropoulos in department of Mechanical Engineering and Professor Jie Yao in department of Materials Science and Engineering, for providing guidance and suggestions.

I would like to thank my fellow doctoral students for their feedback, cooperation and, of course, friendship. Special thanks to Yumeng Liu and Emmeline Kao for numerous conversations about research and life and for sharing all the fun. I also would like to thank Xining Zang for her assistance with the material characterization and experiments. I also want to thank to Ben Eovino for sharing a lot of fun together in two MEMS conferences. I also owe thanks to Caiwei Shen, Takeshi Hayasaka, Levent Beker, Ilbey Karakurt, Eric Sweet, Dongwoo Shin, Jacqueline Elwood, Yue Liang, and Dr. Jin Woo Bae for sharing laughter, frustration, and companionship.

Finally, I am grateful to have had the privilege of attending the prestigious University of California at Berkeley. This experience has afforded me the opportunity to work with a diverse array of talented student colleagues. Thanks for this opportunity.

Table of Contents

Chapter 1. Introduction 1

1.1. Motivation 1
1.2. Dissertation structure 3
1.3. References 5

Chapter 2. Solution Processed Highly Transparent and Conductive Antimony Doped Tin Oxide Thin Films 7

2.1. Overview 7
2.2. Properties of TCOs 8
2.2.1. Electrical conductivity 8
2.2.2. Optical Transmittance 11
2.3. Overview of solution process 18
2.3.1. Sol-gel process 18
2.3.2. Solution processing route 19
2.4. Fabrication process of the solution processed ATO thin films 22
2.4.1. Process overview 22
2.4.2. Experiment 24
2.5. Material characterization of solution processed ATO 24
2.5.1. Energy dispersive X-ray Spectroscopy (EDS) – Element analysis 24
2.5.2. X-ray photoelectron spectroscopy (XPS) – Chemical composition and bonding states 25
2.5.3. Scanning electron microscopy (SEM) - surface morphology 27
2.6. Electrical and optical characteristics of solution processed ATO 30
2.6.1. The effects of doping concentrations 30
2.6.2. The effects of annealing temperatures 31
2.6.3. The effects of ambient gases 33
2.6.4. The effects of thickness of thin films 35
2.7. Summary 37
2.8. References 37

Chapter 3. Improved Mechanical Flexibility of Solution Processed Sb-doped Tin Oxide Films 41

3.1. Overview 41
3.2. Nano indentation 42
3.2.1. Introduction 42
3.2.2. Mechanical properties of solution process ATO thin films 47
3.3. Mechanical stress analysis of solution processed ATO thin films 50
3.3.1. Force controlled stress and strain controlled stress 50
3.3.2. Standard test methods for the flexural properties of the material 51
3.3.3. Finite Element Analysis 53

3.4. Electrical performance changes of the solution processed ATO thin films under mechanical loading 57
3.4.1. ATO deposition on top of a flexible glass substrate 57
3.4.2. Electrical resistance changes under the mechanical loading test 60
3.5. Summary 62
3.6. References 62

Chapter 4. High Aspect Ratio Titanium Dioxide Stabilized Zinc Oxide Nanowires for Photocatalytic Hydrogen Gas Harvester 65

4.1. Introduction 65
4.2. Sustainable, renewable energy sources 65
4.2.1. Motivation 65
4.2.2. Hydrogen production 68
4.3. Photoelectrochemical water splitting 69
4.3.1. Fundamentals of photoelectrochemical water splitting 69
4.3.2. Semiconductor-electrolyte interface 71
4.3.3. Design criteria for PEC cells 76
4.4. Nanostructured metal oxides for PEC cell 78
4.4.1. Metal oxide for photoelectrochemical water splitting 78
4.4.2. Nanostructured materials 79
4.5. Concept and experiments of high aspect ratio TiO_2 stabilize ZnO NWs for photocatalytic hydrogen gas harvester. 80
4.5.1. Concept and material selection 80
4.5.2. Fabrication process and sample preparation 82
4.5.3. Cell efficiency 85
4.6. Characterization 86
4.6.1. Surface morphology - SEM 86
4.7. Results and discussion 89
4.8. Summary 91
4.9. References 92

Chapter 5. Annealing Temperature Effects on Solution Processed SnO_2 Thin Film Transistors (TFTs) 94

5.1. Introduction 94
5.2. Process overview 97
5.3. Material characterization 98
5.4. TFT performance characterizations 101
5.5. Summary 107
5.6. References 108

Chapter 6. Conclusions and Future Work 109

6.1. Conclusions 109
6.2. Future work 110

List of Figures

Chapter 1

Figure 1.1 Number of publications with topics on "oxide" and "nanostructures" and their citations. Image taken from
Figure 1.2 Conceptual illustration of a solar hydrogen refueling station with distributed PEC solar cells producing oxygen and a centralized hydrogen generator
Figure 1.3 Key applications using metal oxides introduced in this dissertation.

Chapter 2

Figure 2.1 Tetragonal structure of SnO_2 with oxygen vacancy and SnO_2 interstitial and schematic energy-level diagram for SnO_2
Figure 2.2 Conceptual schematic of (A) carrier transport paths with strongly directive sp^3 orbitals for covalent bonding semiconductors, so bond angle fluctuation due to dangling bonds and weak bonding states can deteriorate carrier transport by making high density localized states in the band gap. (B) *ns*-orbital sharing with neighboring metal oxide material which makes efficient carrier transport paths even in amorphous phase.
Figure 2.3 (A) Absorption coefficient (α) vs. wavelength (λ) for various semiconductors. **(B)** Band edge position and energy band gap of various materials.
Figure 2.4 Conceptual schematic of light-matter interaction
Figure 2.5 Dielectric function, '$\varepsilon(\omega)$', of free electrons versus frequency in units of the plasma frequency, ω_p. When the dielectric function is positive, electromagnetic waves propagate through the material. Electromagnetic waves are exponential decayed with damping when the dielectric function is negative.
Figure 2.6 Photon energy (eV) versus absorption coefficient. Various absorption factors and transmission window of TCOs.
Figure 2.7 Simplified scheme of sol, gel and aerogel.
Figure 2.8 Flow chart of typical solution processing routes.
Figure 2.9 Illustrates several solution coating and patterning techniques.
Figure 2.10 Schematics of solution process for making ATO thin films **(a)** Metal chloride salt precursors are mixed with alcohol. The mixture undergoes hydrolysis and condensation, resulting in the final coating solution **(b)** Solution deposition process using multiple spinning method. Subsequent thermal annealing densifies the thin films by decomposing the precursors and removing organic solvents. **(c)** Three fabricated transparent electrodes using different annealing gases (N_2, Air and O_2) are placed on top of the printed UC seal to show their transparency
Figure 2.11 Energy dispersive X-ray spectroscopy (EDS) showing chemical composition of ATO thin films and the inset shows the SEM images
Figure 2.12 XPS survey scan of ATO thin films annealed at difference temperatures. The binding energy scales have been referenced to the C1s orbital at 284.6 eV

Figure 2.13 (a) XPS core-level spectra of Sb 2d and **(b)** XPS core-level spectra of Sn 3d showing spin–orbit splitting and chemical shift in ATO samples annealed at different temperatures
Figure 2.14 SEM images of **(a)** 60nm-thick, 10% doping concentration ATO films annealed at different temperatures (300ºC, 400ºC, 500ºC) with oxygen-rich environment **(b)** ATO films different Sb-doping concentration (6%, 8%, 10% and 60nm-thick, annealed at 500ºC with oxygen-rich environment) **(c)** 60nm-thick, 10% doping concentration ATO films annealed at 500ºC with different ambient gases (N_2, Air, O_2) **(d)** 10% Sb-doping ATO films with different thicknesses (90nm, 120nm, 150nm), all samples are annealed at 500ºC with oxygen gas.
Figure 2.15 Measured optical transmittance spectra of ATO thin films from 350 to 800nm: comparison of different doping concentrations of 6%, 8% and 10%. The inset shows the fabricated samples on top of printed UC Seal on a paper.
Figure 2.16 Measured sheet resistance/electrical conductivity of the 60nm-thick ATO samples of different Sb-doping concentration. All samples are annealed at 500ºC with oxygen.
Figure 2.17 Measured optical transmittance spectra of ATO thin films from 350 to 800nm: comparison of different annealing temperature of 300ºC, 400ºC, 500ºC, and 600ºC. The inset shows the fabricated samples on top of printed UC Seal on a paper.
Figure 2.18 Measured sheet resistance/electrical conductivity of the 60nm-thick, 10% Sb-doping concentration ATO samples annealed at different temperature with oxygen-rich environment.
Figure 2.19 Measured optical transmittance spectra of ATO thin films from 350 to 800nm: comparison of different ambient gas during the thermal annealing. The inset shows the fabricated samples on top of printed UC Seal on a paper.
Figure 2.20 Measured sheet resistance/electrical conductivity of the 60nm-thick, 10% Sb-doping concentration ATO samples annealed at 500ºC with different ambient gases
Figure 2.21 Measured optical transmittance spectra of ATO thin films from 350 to 800nm: comparison of different thickness of thin films. The inset shows the fabricated samples on top of printed UC Seal on a paper.
Figure 2.22 Measured sheet resistance/electrical conductivity of the 10% Sb-doping concentration ATO samples annealed at 500ºC in oxygen-rich environment with various thicknesses.

Chapter 3

Figure 3.1 Nano indentation places at several selected points in a microelectronic device.
Figure 3.2 Various shapes of indenter tips.
Figure 3.3 Typical indentation load-displacement data showing experimental quantities.
Figure 3.4 Schematic of the unloading process and parameters for contact geometry.
Figure 3.5 (A) 200nm thick, 10 wt% Sb-doped ATO samples annealed at different temperatures with oxygen-rich environment (B) Hystron nanoindentation machine and controller set up (C) Nanoindenter components
Figure 3.6 Load-penetration depth curves for ATO samples annealed at various temperatures.

Figure 3.7 Hardness and elastic modulus of ATO samples annealed at various temperatures.
Figure 3.8 Schematic of mechanical behavior of thin films under various loading condition.
Figure 3.9 Schematic of four-point bending test for the beam loaded with the forces.
Figure 3.10 FE model of four-point bending test and boundary conditions.
Figure 3.11 Comparative 3D finite element analysis (FEA) showing the deflection of the thin films under force controlled four-point bending.
Figure 3.12 Comparative 3D finite element analysis (FEA) showing the maximum principle stress of the thin films under force controlled four-point bending.
Figure 3.13 Comparative 3D finite element analysis (FEA) showing the deflections of the thin films under force controlled four-point bending.
Figure 3.14 Comparative 3D finite element analysis (FEA) showing the maximum principle stress of the thin films under displacement controlled four-point bending.
Figure 3.15 A 150nm thick ATO thin film on top of flexible glass substrate. Inkjet-printed silver electrode patterns on the ATO thin film.
Figure 3.16 Silver electrode patterned ATO sample with increasing pattern spacing showing electrical resistance between electrodes.
Figure 3.17 Evaluated contact resistance using the transmission line method.
Figure 3.18 Schematic view and built test set-up for measuring the electrical resistance change under the displacement loading.
Figure 3.19 Resistance variation of the ATO thin film under the mechanical loading.

Chapter 4

Figure 4.1 Renewable energy sources. Image taken from *lifefreeenergy.com*
Figure 4.2 U.S. GDP growth versus WTI Oil Price. Image take from *Forbes*
Figure 4.3 The world hydrogen production
Figure 4.4 Photoelectrochemical cell design
Figure 4.5 Simplified illustration of the formation of a space charge region (SCR) at a metal oxide semiconductor when exposed to humid
Figure 4.6 Semiconductor and electrolyte junction diagram (A) before contact (B) after contact
Figure 4.7 Schematic model of the semiconductor/electrolyte interface and the Helmholtz layer.
Figure 4.8 Energy diagram for a PEC with n-type photo-anode and a metal contact. Potential drop due to the Helmholtz layer is presented for both interface (semiconductor/electrolyte and metal/electrolyte).
Figure 4.9 Band edge positions for various semiconductor materials. (in V *vs.* RHE)
Figure 4.10 (A) Formation of the valence and conduction band in covalent semiconductors. (B) Calculated energy band structure of silicon (diamond-cubic crystal structure, the bluish area indicates the occupied states in valence band of the material
Figure 4.11 Molecular-orbital diagram for rutile and anatase of Ti_xO_y
Figure 4.12 Geometry of photoelectrode using nano wires and advantage of nanowires
Figure 4.13 Conceptual illustration of a photocatalytic system. Light induces electron-hole pair generation at the photoanode, oxidizing water to produce hydrogen ions and oxygen

gas. The generated electrons reduce the hydrogen ions at the photocathode producing hydrogen gas.
Figure 4.14 Band position and band bending of TiO_2 at the interface between semiconductor and electrolyte
Figure 4.15 Schematic of fabrication process of high aspect ratio TiO_2/ZnO nanowires
Figure 4.16 Atomic layer deposition system for TiO_2 coating
Figure 4.17 Illustration of photo-anode sample and measurement set up
Figure 4.18 SEM image of (A) zinc oxide nanowires (ZnO NWs) by using hydrothermal growth method; (B) 8nm of TiO_2 coated on ZnO NWs showing partially cover with (C) 40nm of uniformly coated TiO_2 on ZnO NWs using Atomic Layer Deposition (ALD)
Figure 4.19 TEM image of (A) ZnO NW grown by using hydrothermal method; (B) TiO_2 coated ZnO NW using ALD
Figure 4.20 X-ray Diffraction pattern of ZnO nanowires.
Figure 4.21 Photoelectrochemical response of ZnO using the hydrothermal method.
Figure 4.22 Photoelectrochemical response of TiO_2@ZnO using the hydrothermal method.
Figure 4.23 Band gap structure of TiO_2/ZnO nanowires.

Chapter 5

Figure 5.1 Illustration of the simplified cross-sectional view of the p-bulk (n-channel) structures and typical bottom gate TFTs.
Figure 5.2 TFTs for AMLCD and AMOLED display devices as switching transistors and driving transistors.
Figure 5.3 Typical fabrication process of LTPS TFTs with a co-planar top gate structure.
Figure 5.4 Schematics of solution process for making SnO_2 TFTs
Figure 5.5 Optical images of spin coated tin oxide on top of SiO2/n-Si substrate, laser processed shadow mask, and Au electrodes patterning on the semiconductor layer.
Figure 5.6 SEM images of SnO2 thin films annealed at 400ºC with different annealing duration.
Figure 5.7 (A) XPS survey scan of ATO thin films annealed at 400ºC with difference annealing duration (B) XPS core-level spectra of Sn 3d showing spin–orbit splitting.
Figure 5.8 Effects of annealing temperature and duration on gate modulation characteristics of solution processed SnO_2 TFTs.
Figure 5.9 Effects of annealing temperature and duration on the field effect mobility characteristics of solution processed SnO_2 TFTs.
Figure 5.10 Transfer characteristic curves of SnO_2 TFTs
Figure 5.11 Transfer characteristic curves of SnO_2 TFT in a linear scale and log scale showing 10^4 on-off ratios.
Figure 5.12 Output characteristic curves of SnO_2 TFT in a linear scale and log scale showing anomalous diode-like behaviors with a large rectification ratio of 10^9
Figure 5.13 Energy band diagram for (A) before metal and semiconductor contact (B) corresponding Schottky barrier band structure after the contact.
Figure 5.14 Schematic of the bottom gate TFT describing current paths that contribute to the overall current of the device.

List of Tables

Chapter1

Table 1.1 Abundance, cost, production volume, and toxicity of amorphous oxide semiconductor TFT channel layer element cation constituents

Chapter2

Table 2.1 Physical properties of various solvents

Chapter3

Table 3.1 Values for power law fitting constants characterizing unloading curves as observed in nanoindentation experiments with a Berkovich indenter.
Table 3.2 Measured mechanical properties, geometry factors and power law coefficients.

Chapter4

Table 4.1 Gravimetric and volumetric energy densities of several fuels at 1 bar

Chapter 1. Introduction

1.1. Motivation

Metal oxides are an important class of materials in both science and engineering and presenting interesting opportunities due to their rich properties. Especially, there have been a lot of interests in metal oxide thin films and nano structured metal oxide materials for devices applications, such as transparent electrodes, high-mobility transistors, energy harvesters, memory devices, and gas sensors [1]–[11]. **Fig. 1.1** shows the exponential growth of recent publications in the literature and the large numbers of citations.

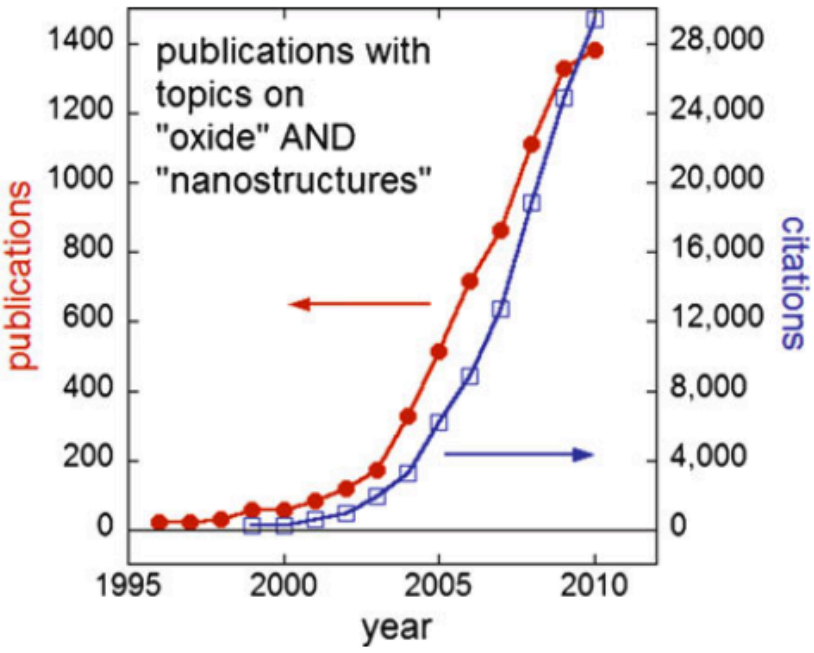

Figure 1.1 Number of publications with topics on "oxide" and "nanostructures" and their citations. Image taken from [12]

Among various modern applications of metal oxides, solid state electronics and ionics devices are considered as some of the most important applications in view of information technology and energy research. Metal oxides thin films especially play a pivotal role in the field of opto-electronic applications due to their unique properties in electrical conductivity and optical transmittance in the visible light spectrum. Although indium tin oxide (ITO) is commonly used as the transparent electrode in many applications, it has several issues for emerging opto-electronic devices. Specifically, Indium is one of the most expensive rare earth elements on the

market and its supply can be controlled by one or two countries. **Table 1.1** presents the abundance, cost, and production volume of various oxide materials.

Element	*Abundance (ppm by mass)*	*Cost ($/ton)*	*World-wide Production (tons/year)*	*Toxic*
Bi	0.0000004	11,100	5,700	No
Ga	2	443,000	73	No
Ge	0.0001	950,000	90	No
In	**0.0002**	**918,000**	**581**	**Yes**
Sb	0.000004	5,250	134,000	No
Sn	0.2	12,500	302,000	No
Zn	8	3,500	9,520,000	No

Table 1.1 Abundance, cost, production volume, and toxicity of amorphous oxide semiconductor TFT channel layer element cation constituents [13]

With regard to oxide materials for semiconductors, In-Ga-Zn-O (IGZO) has become the main stream TFT material since Nomura et al. (2004) reported the first transparent amorphous oxide semiconductor. However, given the rapid growth in the display industry, new candidate materials to make transparent semiconductors are required to replace the expensive indium-based materials. Additionally, a cost-effective technology must be developed to cope with the emerging paradigm of the 'Internet of Things (IoT)', where large quantities of data will be collected and processed by wearable sensors and devices. In this dissertation, we aim to develop a cost- effective material and fabrication process based on solution-processed transparent conductive oxides (TCOs) and oxide semiconductors.

Another important application of metal oxides is in the area of renewable energy sources. For example, the photoelectrochemical (PEC) water splitting process is a technology that can directly convert water and sunlight to hydrogen and oxygen gas [14]. The efficiency and stability of the photo-electrodes are key factors for hydrogen generation in the PEC system. In this respect, metal oxide semiconductors have become attractive materials as high performance photo-electrodes in PEC cells. **Figure 1.2** shows the conceptual illustration of the solar-hydrogen fuel station.

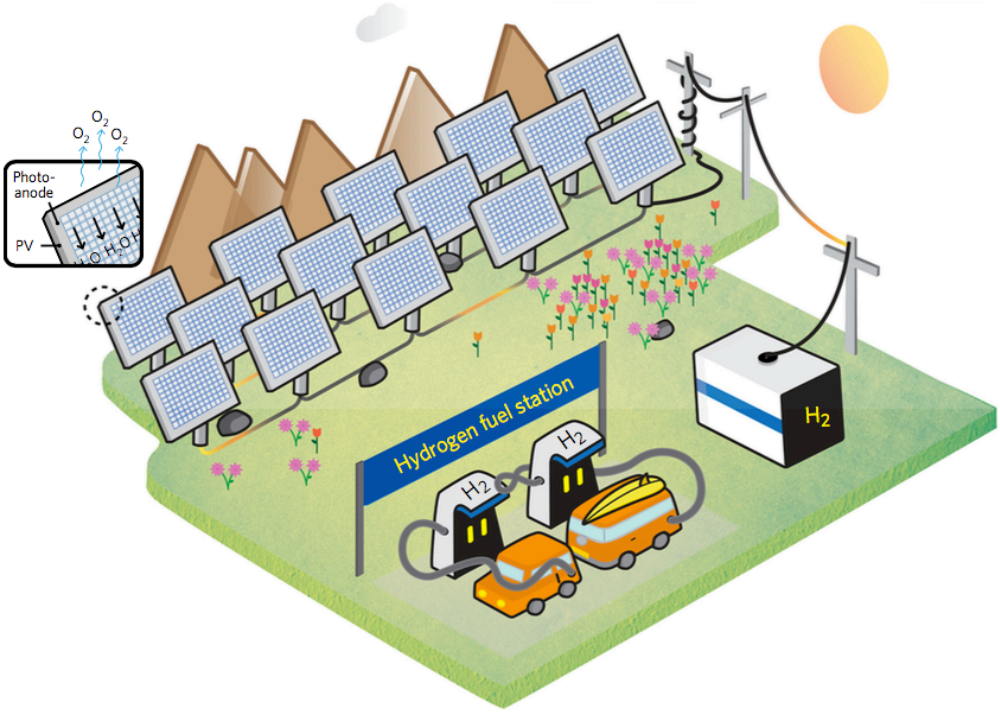

Figure 1.2 Conceptual illustration of a solar hydrogen refueling station with distributed PEC solar cells producing oxygen and a centralized hydrogen generator [15].

Recently, there has been a growing interest in nano-structured metal oxides [16]–[18] for photo-electrodes. Various types of nano-structured metal oxides offer advantages over their bulk counterparts for photo-electrode applications due to the very large specific surface area, short diffusion length, and low reflectivity [19]. Among various types of nano-structures geometries, much attention has been focused on high-aspect ratio nano-wires metal oxides. As such, a novel method to grow high-aspect ratio metal oxide nanowire and their photoelectrochemical performances are detailed in this dissertation.

1.2. Dissertation structure

This dissertation introduces metal oxide materials and their modern applications in the field of information technology and renewable energy production in four major chapters in the following manner. The key intellectual contributions are illustrated in **Figure 1.3**, including solution-processed highly conductive and optically transparent ATO thin films, improved mechanical flexibility of ATO thin films, high aspect ratio TiO_2 nano-array for photoelectrochemical water splitting and solution-processed SnO_2 TFTs for display devices.

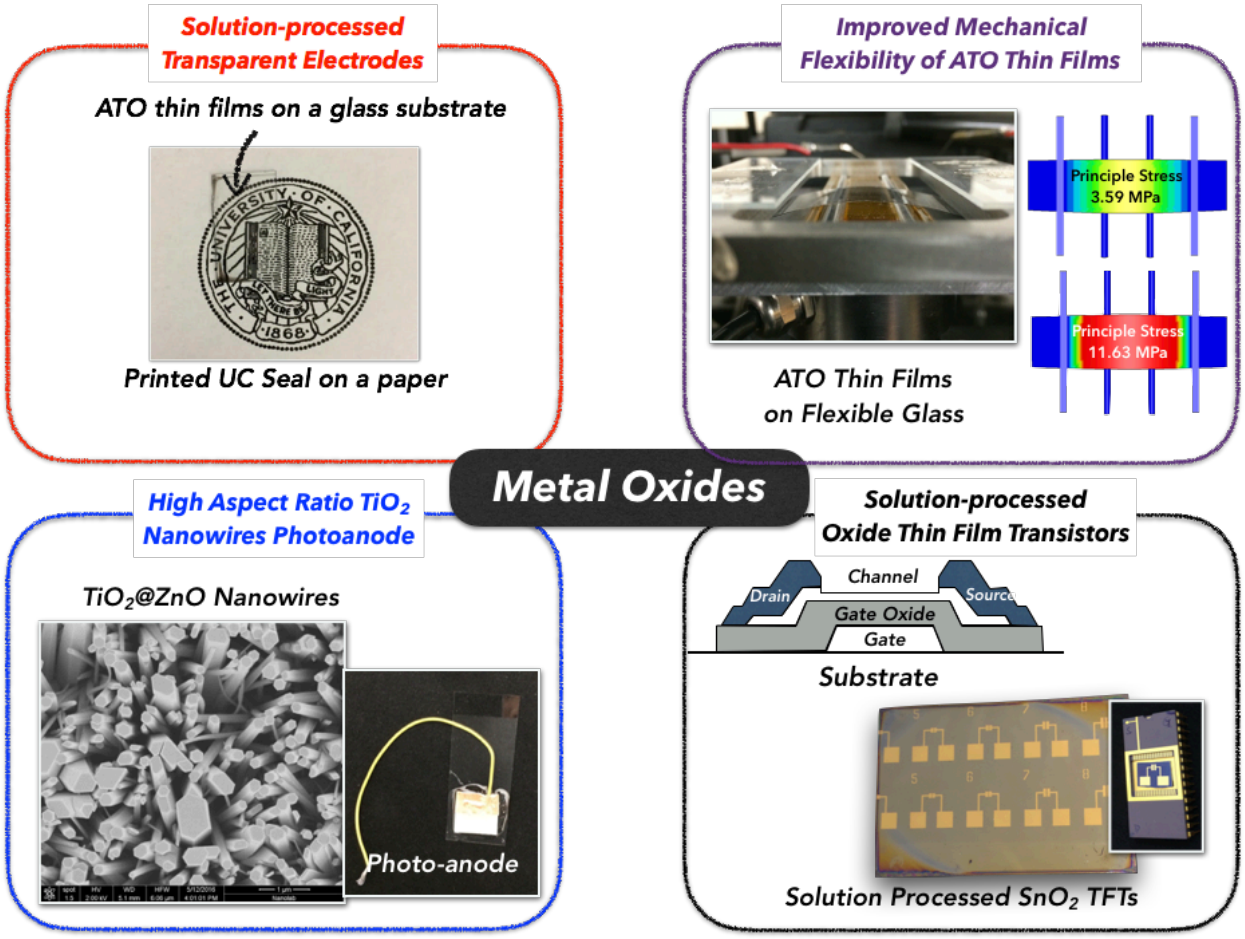

Figure 1.3 Key applications using metal oxides introduced in this dissertation.

Chapter 2 is the development of a solution-processed conductive and transparent tin oxide (ATO) electrode with Sb as the dopant for usages in transparent electrodes for emerging opto-electronic devices such as display devices, solar cells, and smart windows. This chapter also gives the fundamentals of physical properties of transparent conductive oxides (TCOs) and details the fabrication process based on the solution fabrication processes.

In chapter 3, the mechanical properties of solution-processed TCOs are introduced using the scheme of nano-indentation. In addition, 3D finite element analysis is introduced to compare the mechanical stress responses and mechanical flexibility of the thin films. Background information about nano-indentation and finite element analysis results is also discussed.

Chapter 4 introduces a modern energy application of metal oxide materials with a brief introduction on the renewable energy source and conventional hydrogen production. The fundamentals of the photoelectrochemical water splitting process to produce hydrogen and metal oxide photoanode are also described. The high aspect-ratio and vertically ordered TiO_2-stabilized ZnO nanowires using the hydrothermal/ALD process for the use of a solar-powered hydrogen gas harvester is detailed.

Chapter 5 describes the details on the fabrication process and characterization results of the SnO_2 TFTs by using the solution-based process of using multiple spin-coating steps. The effects of annealing temperature on TFT performances and material characterizations is also discussed.

Chapter 6 concludes the thesis and outlines the potential future works.

1.3. References

[1] J. Hu and R. G. Gordon, "Textured fluorine-doped ZnO films by atmospheric pressure chemical vapor deposition and their use in amorphous silicon solar cells," *Sol. Cells*, vol. 30, no. 1–4, pp. 437–450, 1991.

[2] H. Enoki, T. Nakayama, and J. Echigoya, "The Electrical and Optical Properties of the ZnO-SnO , Thin Films Prepared by RF Magnetron Sputtering," *Phys. Status Solidi*, vol. 129, pp. 181–191, 1992.

[3] T. Minami, H. Sonohara, T. Kakumu, and S. Takata, "Highly Transparent and Conductive $\bf Zn_{2}In_{2}O_{5}$ Thin Films Prepared by RF Magnetron Sputtering," *Jpn. J. Appl. Phys.*, vol. 34, no. Part 2, No. 8A, pp. L971–L974, 1995.

[4] J. M. McGraw, P. A. Parilla, D. L. Schulz, J. Alleman, X. Wu, W. P. Mulligan, D. S. Ginley, and T. J. Coutts, "Pulsed laser deposition of cadmium stannate, a spinel-type transparent conducting oxide," *Mater. Res. Soc. Symp. - Proc.*, vol. 388, pp. 51–56, 1995.

[5] T. Minami, H. Sonohara, S. Takata, and H. Sato, "Highly Transparent and Conductive Zinc-Stannate Thin Films Prepared by RF Magnetron Sputtering," *Japanese J. Appl. Phys. Part 2-Letters*, vol. 33, no. 12A, pp. L1693–L1696, 1994.

[6] I. Safi and R. P. Howson, "The properties of reactively-sputtered, stoichiometry-controlled and optimum-conductivity transparent indium oxide films as a function of their titanium, aluminium and zinc content; comparisons with the use of tin as a dopant," *Thin Solid Films*, vol. 343–344, no. 6090, pp. 115–118, 1999.

[7] M. Orita, H. Ohta, M. Hirano, S. Narushima, and H. Hosono, "Amorphous transparent conductive oxide $InGaO_3(ZnO)_m$ ($m \leq 4$): a Zn4s conductor," *Philos. Mag. Part B*, vol. 81, no. 5, pp. 501–515, 2001.

[8] E. Fortunato, P. Barquinha, and R. Martins, "Oxide semiconductor thin-film transistors: A review of recent advances," *Adv. Mater.*, vol. 24, no. 22, pp. 2945–2986, 2012.

[9] M. Prezioso, F. Merrikh-Bayat, B. D. Hoskins, G. C. Adam, K. K. Likharev, and D. B. Strukov, "Training and operation of an integrated neuromorphic network based on metal-oxide memristors," *Nature*, vol. 521, no. 7550, pp. 61–64, 2015.

[10] D. Seok Jeong, I. Kim, M. Ziegler, and H. Kohlstedt, “Towards artificial neurons and synapses: a materials point of view,” *RSC Adv.*, vol. 3, no. 10, p. 3169, 2013.
[11] W. Göpel, “Chemisorption and Charge Transfer at Ionic Semiconductor Surfaces: Implifications in Designing Gas Sensors,” *Prog. Surf. Sci.*, vol. 20, no. 1, pp. 9–103, 1985.
[12] S. Ramanathan, *Thin Film*. Cambridge: Springer.
[13] J. F. Wager, “15 . 1 : Invited Paper : Amorphous Oxide Semiconductor Thin-Film Transistors : Performance & Manufacturability for Display Applications,” *SID*, pp. 181–183, 2009.
[14] M. G. Walter, E. L. Warren, J. R. McKone, S. W. Boettcher, Q. Mi, E. A. Santori, and N. S. Lewis, “Solar Water Splitting Cells.,” *Chem. Rev. (Washington, DC, United States)*, vol. 110, no. 11, pp. 6446–6473, 2010.
[15] A. Landman, H. Dotan, G. E. Shter, M. Wullenkord, A. Houaijia, A. Maljusch, G. S. Grader, and A. Rothschild, “Photoelectrochemical water splitting in separate oxygen and hydrogen cells,” *Nat. Mater.*, vol. 16, no. March, 2017.
[16] V. Berube and M. Dresselhaus, “Nano-structured materials to address challenges of the hydrogen initiative,” vol. 1041, pp. 51–61, 2008.
[17] A. Kudo and Y. Miseki, “Heterogeneous photocatalyst materials for water splitting,” *Chem. Soc. Rev.*, vol. 38, no. 1, pp. 253–278, 2009.
[18] S. S. Mao, S. Shen, and L. Guo, “Nanomaterials for renewable hydrogen production, storage and utilization,” *Prog. Nat. Sci. Mater. Int.*, vol. 22, no. 6, pp. 522–534, 2012.
[19] X. Yang, A. Wolcott, G. Wang, A. Sobo, R. C. Fitzmorris, F. Qian, J. Z. Zhang, and Y. Li, “Nitrogen-doped ZnO nanowire arrays for photoelectrochemical water splitting,” *Nano Lett.*, vol. 9, no. 6, pp. 2331–2336, 2009.

Chapter 2. Solution Processed Highly Transparent and Conductive Antimony Doped Tin Oxide Thin Films

2.1. Overview

There are growing interests in the fields of transparent conductive oxides (TCOs) since they have excellent properties in both electrical conductivity and optical transparency in the visible light spectrum [1]. As such, they have been key elements in many state-of-art opto-electronic devices such as solar cells, displays and electrochromic windows [2].

Transparent conducting materials have large energy band gaps so that visible light can pass through. On the other hand, they also need to have high concentration of carriers with decent mobility for good electrical conductivity [3]. In general, the trade-offs between the transmittance and carrier concentration decide the suitability of the transparent conducting materials. For example, a large number of free carriers can result in high plasma frequency absorptions in the visible light range to make the material opaque. As such, there are very few material candidates to meet the properties of both transparency and conductivity.

There are two types of metal oxides for TCOs: pure metal oxides and compound metal oxides such as: indium oxide (In_2O_3), tin oxide (SnO_2), and zinc oxide (ZnO). Their energy band gaps are greater than 3.1 eV [4] such that they are transparent to visible light. They also have high concentrations of intrinsic free carriers due to oxygen vacancies and defects. However, these pure metal oxides films are not suitable for practical use due to their high electrical resistivity and instability [5]. In most cases, extrinsic dopants are added for optic-electronic applications. For example, the most widely used TCO is dc magnetron sputtered tin doped indium oxide (ITO) deposited for its good optical transmittance and favorable electrical conductivity [3]. However, ITO has several drawbacks for outdoor systems such as digital signs, smart windows and automobile displays. First, indium is an expensive rare earth material [6]. Second, it is not stable under high temperature and humid environment [7]. Third, vacuum-based processes are expensive for large-scale processes. As such, various research labs have been looking into new oxide materials to replace ITO with low-cost deposition processes [8].

Previously, J. Hu et al. demonstrated fluorine-doped ZnO films by using atmospheric pressure chemical vapor deposition to make high quantum efficiency TCO films for solar cell applications [9]. J. M. McGraw et al. presented Cd_2SnO_4 films by the pulsed laser depositions for thermo-voltaic plasma filter applications [10]. D. J. Seo et al. deposited In_2O_3: Mo (IMO) films on glass substrates by using the spray pyrolysis method [11]. Among various TCO materials, antimony doped tin oxide (ATO) thin films have attracted a lot of interest due to its outstanding properties in thermal, chemical, and mechanical stability [12]–[14]. Among various deposition methods, chemical solution deposition has lately become a subject of interest due to its ease of fabrication, scalability, as well as the potential to lower device-manufacturing costs [15].

Solution-processed ATO thin films have been previously reported without detailed studies. This work report results on high quality ATO film depositions with detailed material characterizations.

2.2. Properties of TCOs

In this section, the fundamentals of electrical and optical properties of TCOs are discussed. There are two factors determining the electrical conductivity of materials: free carrier concentration and carrier mobility. For the optical transparency, energy bandgap and plasma frequency are the key factors. From a traditional band-structure perspective, electrical conductivity and optical transparency seem in conflict with each other [16]. However, a lot of metal oxide materials show both high conductivity and optical transparency due to strong interactions between the '*2p*' orbital in oxygen and '*s*' orbital in metal cations [17]. This section will summarize the general physical properties of TCO materials including their unique carrier transport mechanism.

2.2.1. Electrical conductivity

In a constant electric field, $\boldsymbol{E}$, the force, $\boldsymbol{F}$, acting on an electron of charge, e, is $e\boldsymbol{E}$. When the collision time for scattering is τ, Newton's second law of motion becomes

$$m\frac{d\vec{v}}{dt} = eE - \frac{m}{\tau}\vec{v} \tag{2-1}$$

assuming the velocity of electrons reach to the constant terminal velocity $\boldsymbol{v_t}$

$$eE = \frac{m}{\tau}v_t \tag{2-2}$$

so that the terminal velocity of electrons in a material is defined as

$$v_t = \frac{eE\tau}{m} \tag{2-3}$$

the electrical current density is

$$j = nev_t \tag{2-4}$$

where $\boldsymbol{n}$ is the carrier concentration (# cm^{-3}), by plugging equation (2-3) into (2-4), we obtain

$$j = \frac{ne^2\tau}{m}E \tag{2-5}$$

according to the Ohm's law, the electrical conductivity is defined by $\boldsymbol{j=\sigma E}$,

$$\sigma = \frac{ne^2\tau}{m} \tag{2-6}$$

and the carrier mobility can be described as the velocity to the field ratio:

$$\mu = \frac{|\vec{v}|}{|\vec{E}|} = \frac{e\tau}{m} \tag{2-7}$$

so, by substituting equation (2-7) into (2-6), electrical conductivity can be described as

$$\sigma = ne\mu \tag{2-8}$$

Eq. (2-6) implies that in order to increase the electrical conductivity, free carrier concentration or carrier mobility should be increased.

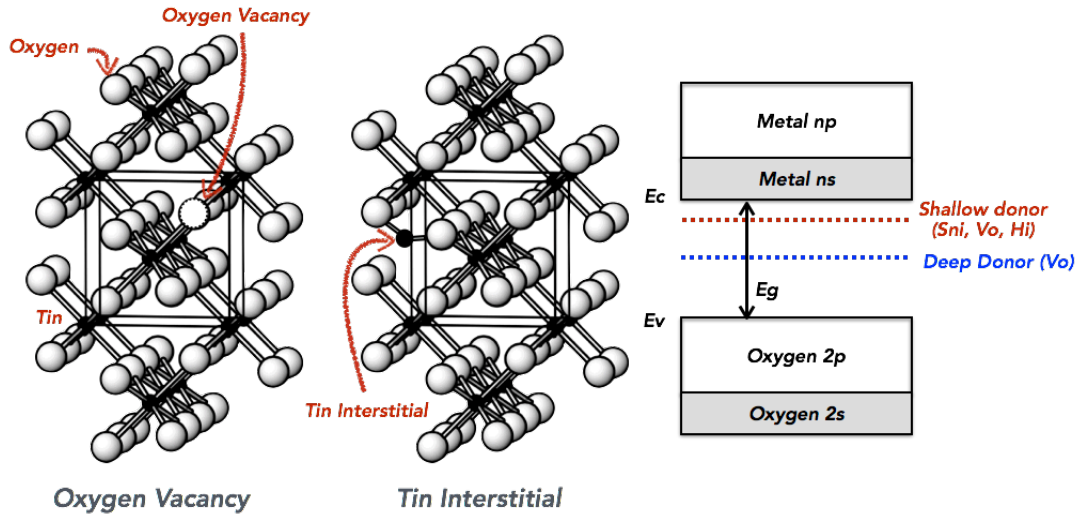

Figure 2.1 Tetragonal structure of SnO_2 with oxygen vacancy and SnO_2 interstitial and schematic energy-level diagram for SnO_2.

To increase the free carrier concentration, there are two types of carrier generations, intrinsic carrier formation and extrinsic carrier formation for the oxide materials. For the pure, defect free material at T=0K, all electrons occupy their ground states. However, for a temperature above 0 K, native point defects such as vacancies, interstitials, or substituents can be formed by intrinsic defect-chemical reactions or by a change in the lattice stoichiometry **(Fig. 2.1)**. Such a process for the oxygen reduction reaction in oxides can be described using the Kröger-Vink notation [15]:

$$O_O^x = V_O^{**} + \frac{1}{2}O_2(g) + 2e' \tag{2-9}$$

This equation shows that by introducing oxygen vacancies, incorporated dopant concentration increases due to the free carrier generations. Even though the intrinsically formed free carriers can enhance the electrical conductivity, for most binary metal oxide materials, free carrier generations due to oxygen vacancy itself is not sufficient for good conductivity. Carriers concentration also can be increased extrinsically by introducing substitutional atoms of different valence. In the case of In-doped ZnO, the presence of In^{+3} occupying Zn^{+2} sites gives rise to free carrier generation to keep the charge neutrality. The equilibrium reaction can be written in as [15]:

$$In_2O_3 \xrightarrow{ZnO} 2In_{Zn}^{*} + 2O_O^x + \frac{1}{2}O_2(g) + 2e' \tag{2-10}$$

Another factor for electrical conductivity is the carrier mobility. **Eq. (2-7)** exhibits that in order to enhance the carrier mobility, the collision time for scattering must be increased or the effective mass must be decreased. Effective mass is related to new material development and the scattering time involves film quality. As carriers pass through a TCO material, they meet a lot of obstacles such as impurities, phonon modes, grain boundaries and defects. Generally, anything that impedes the carrier transport in the material decreases scattering time, τ, and carrier mobility. According to the Matthiesens rule [18], resistivity (the reciprocal of the conductivity) arises from independent, additive scattering processes such as scattering by impurities, grain boundaries and defects:

$$\frac{1}{\mu_{Total}} = \frac{1}{\mu_{imp}} + \frac{1}{\mu_{gb}} + \frac{1}{\mu_{def}} \ldots \tag{2-11}$$

The most important scattering sources that hinder the carrier transport process are ionized impurity scattering and phonon scattering. For TCO thin films made by solution-processing, porosity in the material after thermal annealing is an important scattering source; pores can be formed during the decomposition of precursors and the removal of the organic solvents.

Grain boundaries and crystal size also affect the properties of semiconductor materials. However, the carrier transport process in metal oxides is different than that of the Si-based semiconductors. For example, in Si-based materials, the carrier mobility in a-Si:H (about 1 $cm^2V^{-1}s^{-}1$) is two or three orders of magnitude lower than that of the crystalline silicon (over 200 $cm^2V^{-1}s^{-1}$ for carrier concentration ~$10^{19}cm^{-3}$). This huge difference is mainly attributed to their chemical bonding states **(Fig. 2.2)**. In the covalent-bonding semiconductors, conduction band minimum (CBM) and valence band maximum (VBM) are defined by the hybridized sp^3 σ-bonding and sp^3 σ*-anti- bonding states. The carrier transport is strongly associated with the directivity of the sp^3 orbital. In the a-Si:H, there exists high density of localized and deep tail states due to the dangling bonds and weak bond states. Therefore, the major carrier transport mechanism for the a-Si:H is hopping and trapping between localized tail-states while the band conduction is achieved in crystalline silicon [19], [20].

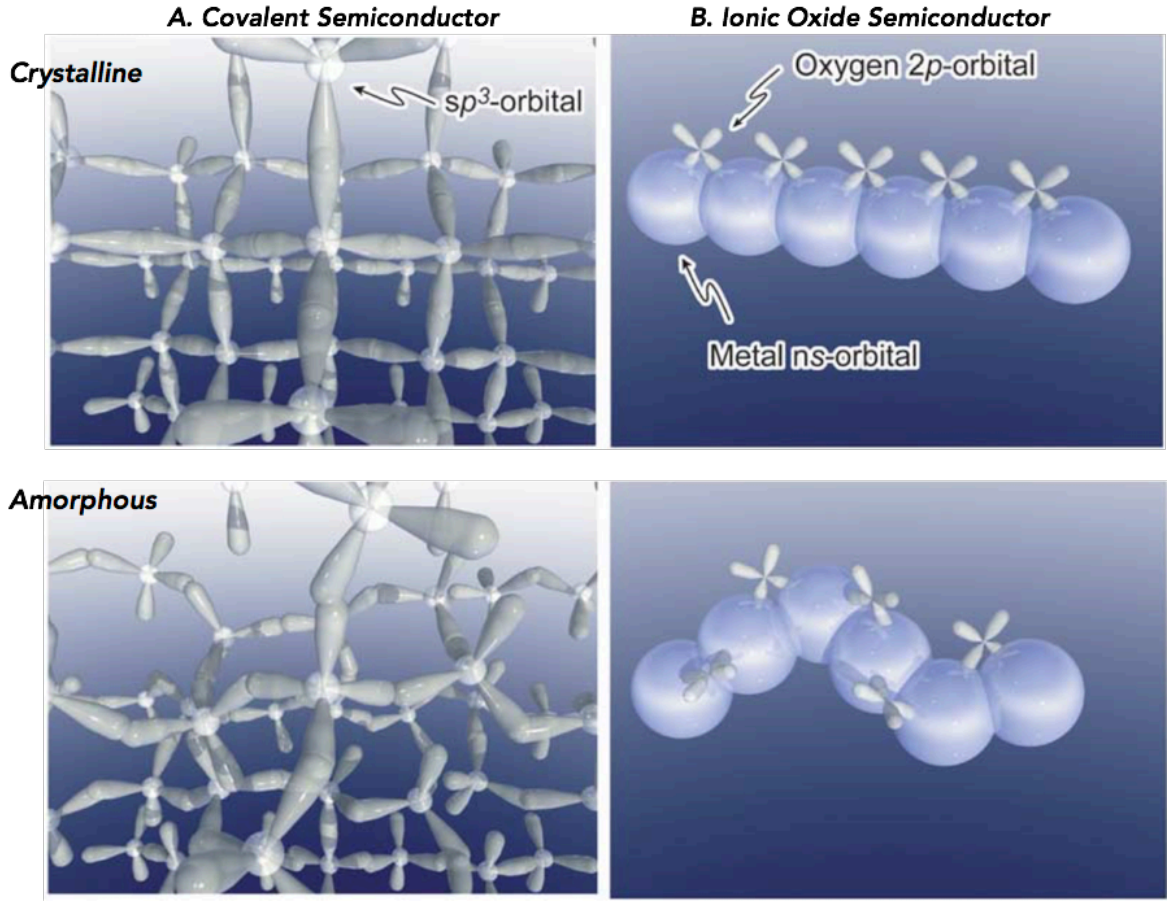

Figure 2.2 Conceptual schematic of (A) carrier transport paths with strongly directive sp3 orbitals for covalent-bonding semiconductors, (B) The ns-orbital sharing with neighboring metal oxide material. Image taken from [19].

Unlike the covalent-bonding semiconductors in which crystallinity is an important issue for the carrier mobility, crystallinity in the metal oxide material is not a necessity for high conductivity. The valence band of the oxide material is typically composed of occupied 2*p* oxygen anti-bonding states, and the conduction band is mainly unoccupied *ns* metal bonding states [21]. **Fig. 2.2** illustrates the spherically symmetrical *ns*-orbital overlapping with neighboring metal *ns*-orbital in the metal oxide material. This *ns*-orbital overlapping arrangement makes the carrier transport path insensitive to lattice distortion, thus, efficient electron transport is available even in amorphous materials [22], [23].

2.2.2. Optical Transmittance

For optical transparency of the material, there are two important factors: the energy band gap and plasma frequency. The wavelength of the visible light is around 400 to 700nm, and their corresponding energies are 1.63 eV and 3.1 eV. When visible light is shined on a material in which the energy band gap is smaller than 3.1 eV, electrons in the valence band can be excited

from the valence band to the conduction band by absorbing the energy from the visible light. However, for the material whose energy bandgap is larger than 3.1 eV, incident visible light will mostly pass through the material and only small amounts of absorption will happen due to the free carriers. Thus, transparent materials have energy band gap larger than 3.1 eV.

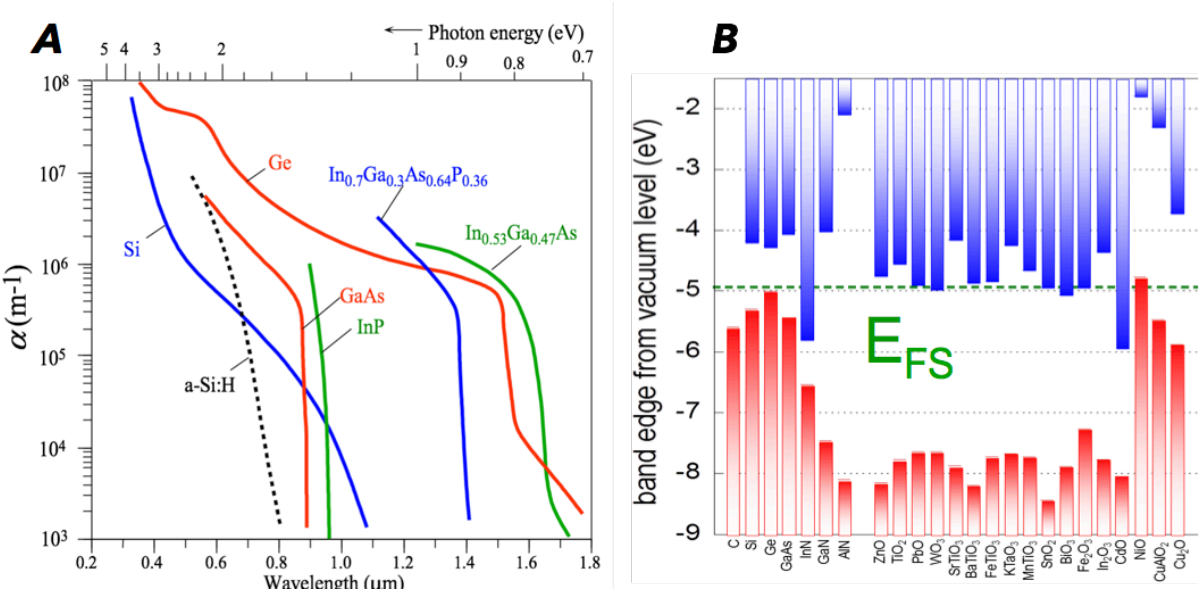

Figure 2.3 (A) Absorption coefficient (α) vs. wavelength (λ) for various semiconductors. **(B)** Band edge position and energy band gap of various materials [24], [25].

Fig. 2.3(A) shows the absorption spectra of various semiconductors used for optoelectronic devices. Physical meaning of the absorption coefficient, *a*, is the distance the light can travel from the surface before the intensity is attenuated by a factor of '*e*'. For Si, the absorption length becomes longer for the incident light with wavelength longer than 1.1 μm (1.12 eV). This means that a long absorption length is needed for the incident light with energy smaller than 1.12 eV and less light will be absorbed. Thus, this 1.12 eV indicates the energy band gap of Si. **Fig. 2.3(B)** illustrates that the band edge position and energy band gap of various semiconductor materials and metal oxide materials. Generally, the energy band gap of a material can be determined by lattice constant and ionicity. When the lattice constant decreases, energy band gap increases due to its increased electron negativity. Ionicity is also an important factor for determining the energy band gap of the material as the band gap increases when the iconicity increases. As such, many metal oxide materials exhibit large energy band gaps for transparent conductive oxides.

The second factor for the optical transparency of the material is plasma frequency. According to the Drude free electron model [26], when the frequency of the visible light (ω) is smaller than the plasma frequency (ω_p) (where the frequency of the oscillation free electrons in the material is the same as the frequency of the incident light), electrons can interact with the electric field of the incident light, thereby decreasing the optical transmittance at the plasma frequency due to the light absorption caused by the light-matter interactions (**Fig. 2.4**).

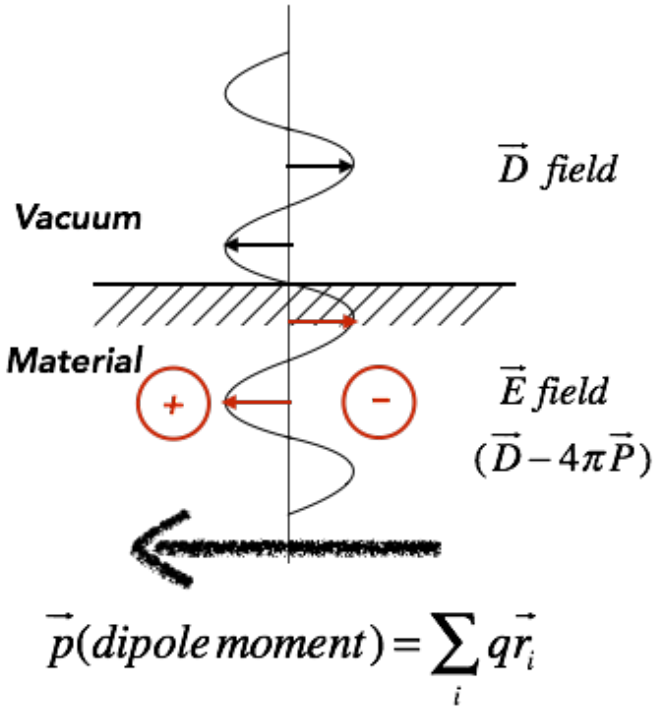

Figure 2.4 Conceptual schematic of light-matter interaction

The dielectric constant, ε, can be defined using electric field, $\boldsymbol{E}$, and the polarization, $\boldsymbol{P}$. When the light, the oscillation of an electromagnetic wave, shines on a material with free carriers, the dipole moment, due to interaction between free carriers and electromagnetic field, will be attenuated by '$4\pi\boldsymbol{P}$'. The electric field in the material can be expressed by introducing the displacement field '$\boldsymbol{D}$' (electric filed in vacuum) [18]

$$\boldsymbol{D} = \boldsymbol{E} + 4\pi\boldsymbol{P} = \varepsilon\boldsymbol{E}\ \ (CGS); \qquad \boldsymbol{D} = \varepsilon_0\boldsymbol{E} + \boldsymbol{P} = \varepsilon\varepsilon_0\boldsymbol{E}\ (SI) \tag{2-12}$$

$$\varepsilon(\omega) = \left(1 + \frac{4\pi\boldsymbol{P}}{\boldsymbol{E}}\right), \qquad \frac{\boldsymbol{P}}{\boldsymbol{E}} = \chi\ (Susceptibility) \tag{2-13}$$

Since the dielectric constant is a function of frequency of the incident light (ω), it is important to figure out polarization at some frequency (ω) in response to an electric field. When the $\boldsymbol{v}$, $\boldsymbol{r}$ and $\boldsymbol{E}$ have time dependency, $\boldsymbol{e^{i\omega t}}$, then [26]

$$\boldsymbol{v} = v_o \cdot e^{-i\omega t} \tag{2-14}$$

$$\boldsymbol{r} = \int \boldsymbol{v}\, dx = \int v_o \cdot e^{-i\omega t}\, dt = \frac{v_o \cdot e^{-i\omega t}}{-i\omega} = \frac{\boldsymbol{v}}{-i\omega} \tag{2-15}$$

$$\boldsymbol{v} = -i\omega\boldsymbol{r} \tag{2-16}$$

the dipole moment of one electron is

$$\boldsymbol{p} = -e\boldsymbol{r} \tag{2-17}$$

and by plugging **Eq. (2-15)** and **Eq. (2-17)**, the polarization, defined as the dipole moment per unit volume, can be expressed as

$$\boldsymbol{P} = n \cdot \boldsymbol{p} = \left(\frac{\#}{Vol.}\right) \cdot \left(\frac{polarization}{electron}\right) = n \cdot -e \cdot \frac{\boldsymbol{v}}{-i\omega} = \frac{\boldsymbol{j}}{-i\omega} = \frac{\boldsymbol{\sigma}}{-i\omega}\boldsymbol{E} \tag{2-18}$$

Since the conductivity for the alternation current (AC) is defined as

$$\boldsymbol{\sigma} = \frac{ne^2 \cdot \tau}{m(1 - i\omega\tau)} \tag{2-19}$$

The dielectric function at frequency, ω, follows from **Eq. (2-13), (2-18)** and **(2-19)**

$$\varepsilon(\omega) = \left(1 + \frac{4\pi\boldsymbol{P}}{\boldsymbol{E}}\right) = \left(1 - \frac{4\pi\boldsymbol{\sigma}}{i\omega}\right) = 1 - \frac{4\pi \cdot ne^2 \cdot \tau}{mi(1 - i\omega\tau)} = 1 - \frac{4\pi \cdot ne^2}{m\omega^2\left(1 + \frac{i}{\omega\tau}\right)} \tag{2-20}$$

For the high frequency charges such as conduction electrons, the dielectric function can be expressed as

$$\varepsilon(\omega) = 1 - \frac{4\pi \cdot ne^2}{m\omega^2\left(1 + \frac{i}{\omega\tau}\right)} = 1 - \frac{4\pi \cdot ne^2}{m\omega^2} \tag{2-21}$$

and the plasma frequency, ω_p, is defined by the relation

$$\omega_P = \sqrt{\frac{4\pi ne^2}{m^*}} \tag{2-22}$$

thus, we can rewrite the dielectric function (2-21) as

$$\varepsilon(\omega) = 1 - \frac{4\pi \cdot ne^2}{m\omega^2} = 1 - \frac{\omega_p^2}{\omega^2} \tag{2-23}$$

The refractive index of a material, *N*, is defined as ratio of the speed of light in a vacuum to the speed of light in the material [26].

$$N = \frac{c}{c_m} \tag{2-24}$$

where c is the speed of light in a vacuum and c_m, of the material. From the Maxwell equation, the wave equation in three dimensions for the vacuum can be deduced as:

$$\nabla^2 E = \mu_0 \varepsilon_0 \frac{\partial^2 E}{\partial t^2} \tag{2-25}$$

where μ_0 is the permeability in a vacuum and by considering the 1-D equivalent, **Eq. (2-25)** can be simplified as

$$\frac{\partial^2 E}{\partial x^2} = \mu_0 \varepsilon_0 \frac{\partial^2 E}{\partial t^2} \tag{2-26}$$

a solution to this equation is a sinusoidal wave of wavelength, λ, and speed, c,

$$E = E_0 \sin\left(2\pi \frac{x - ct}{\lambda}\right) \tag{2-27}$$

by applying **Eq. (2-27)** into **Eq. (2-26)**, we get

$$-E_0 \left(\frac{2\pi}{\lambda}\right)^2 \sin\left(2\pi \frac{x - ct}{\lambda}\right) = -\mu_0 \varepsilon_0 E_0 \left(\frac{2\pi c}{\lambda}\right)^2 \sin\left(2\pi \frac{x - ct}{\lambda}\right) \tag{2-28}$$

and the speed of light, c, in a vacuum can be expressed as

$$\frac{1}{c^2} = \mu_0 \varepsilon_0 \tag{2-29}$$

Similarly, the speed of light in a material also can be described as

$$\frac{1}{c_m^2} = \mu \varepsilon \tag{2-30}$$

where μ' is not the electron mobility but the permeability in a material. For the non-magnetic material, the permeability is 'μ_0', therefore;

$$\frac{1}{c_m^2} = \mu_0 \varepsilon \tag{2-31}$$

using **Eq. (2-24), (2-29)** and **(2-31)**, the refractive index 'N' becomes:

$$N = \frac{c}{c_m} = \left(\frac{\mu_0 \varepsilon_0}{\mu_0 \varepsilon}\right)^{-\frac{1}{2}} = \left(\frac{\varepsilon}{\varepsilon_0}\right)^{\frac{1}{2}} \tag{2-32}$$

As shown in **Eq. (2-32**), the refractive index in a material is a function of the dielectric constant. For the material with refractive index, N, the wave number of light, k_0, in a vacuum changes to '$k=Nk_0$' in a material. In **Eq. (2-23)**, when the plasma frequency, ω_p, is larger than the frequency of the incident beam, ω, the dielectric function, $\varepsilon(\omega)$, becomes a negative number and, hence, the refractive index, N, and the wave number, k, can be written as

$$N = i|N|, \quad k = i|N|k_0 \tag{2-33}$$

and, due to the imaginary part in the wave number, the light wave becomes

$$e^{ikx} = e^{-i|N|k_0 x} \tag{2-34}$$

thus, incident light in the material will be exponentially attenuated. On the other hand, when the dielectric function is a positive number (the plasma frequency, ω_p, is smaller than the frequency of the incident beam, ω), the light wave has only real part and, therefore, will propagate through the material. **Fig. 2.5** shows that how the plasma frequency plays an important role in separating the region of attenuation and the region of propagation by changing the dielectric function and affecting the transmittance in a material.

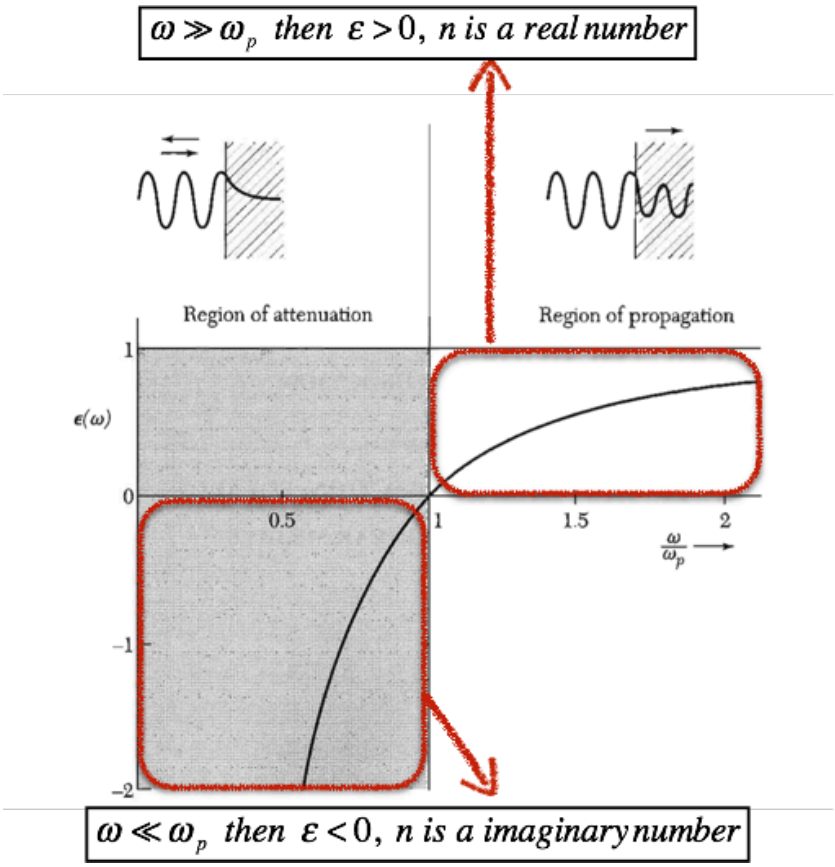

Figure 2.5 Dielectric function, $\varepsilon(\omega)$, of free electrons versus frequency in units of the plasma frequency, ωp. Image taken from [26]

As shown in **Equation (2-22)**, the plasma frequency is not a constant value but changes with the free carrier concentration. With more or fewer free carriers in a material, the plasma frequency also becomes larger or smaller. Here, we have a conflict between optical transmittance and electrical conductivity. While higher concentrations of free carriers are able to enhance the electrical conductivity, it also deteriorates the optical transmittance by shifting the plasma frequency to the higher value. For optical transmittance, a smaller plasma frequency value is desirable for entering the region of propagation in **Fig. 2.5**.

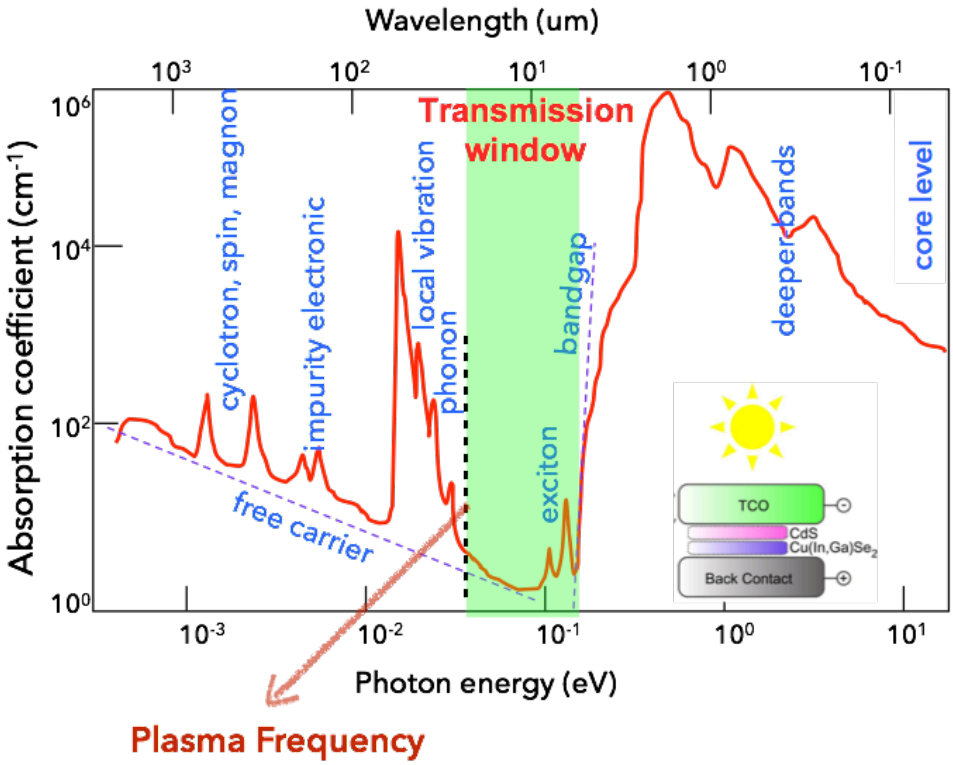

Figure 2.6 Photon energy (eV) versus absorption coefficient. Various absorption factors and transmission window of TCOs. Image taken from [27]

Fig. 2.6 indicates the dilemma of TCOs. There are the two limiting factors that make the narrow transmission window of TCOs: the energy band gap and the plasma frequency. The light waves are absorbed into the material when the photon energy is higher than the energy band gap of the material. When the energy of the light wave is smaller than the energy at the plasma frequency, the light wave will decay exponentially. To have a wider width of the transmission window of TCOs, a large energy band gap and a lower free carrier concentration is needed, these two conditions will decrease the electrical conductivity. Although there are a lot of metal oxide materials in nature, finding the balance between the optical transparency and the electrical conductivity of TCO materials has been an issue. This trade-off relation explains why only a few TCO materials have evolved to practical commercial products.

2.3. Overview of solution process

2.3.1. Sol-gel process

A sol is a colloidal suspension of particles in a liquid. The particle size typically ranges from 1 nm to 1000 nm so that gravitational forces are negligible and van der Waals attraction and electrical charges on a surface are dominant in a sol. The main difference between a sol and a non-colloidal liquid is that the nano-size particles in a sol are well dispersed in solvent due to

their electrical charges so they can be precipitated out by a centrifuge, but non-colloidal liquid solutions like salt dissolved in water cannot be precipitated. The most famous example of a sol is carbon black dispersed in water (black ink for inkjet printing).

A gel is a substance that contains a continuous interconnected solid network in macroscopic dimensions so that it spans throughout the solution. The interconnection in a gel is not bonding, rather covalent linking: gelatin gels are linked by the entanglements of chains, while the van der Waals force also can establish the particular gel formation. Typically, gel process begins with the formation of fractal aggregates that grow until they begin to impinge on one another [28]. Aqua gels or hydrogels use pure water or mostly water solvent (when the solvent is alcohol, it is called an alcogel). After the removal of solvent, it is called an aerogel or dry gel. The most famous example of a gel is "JELL-O gelatin". **(Fig. 2.27)**

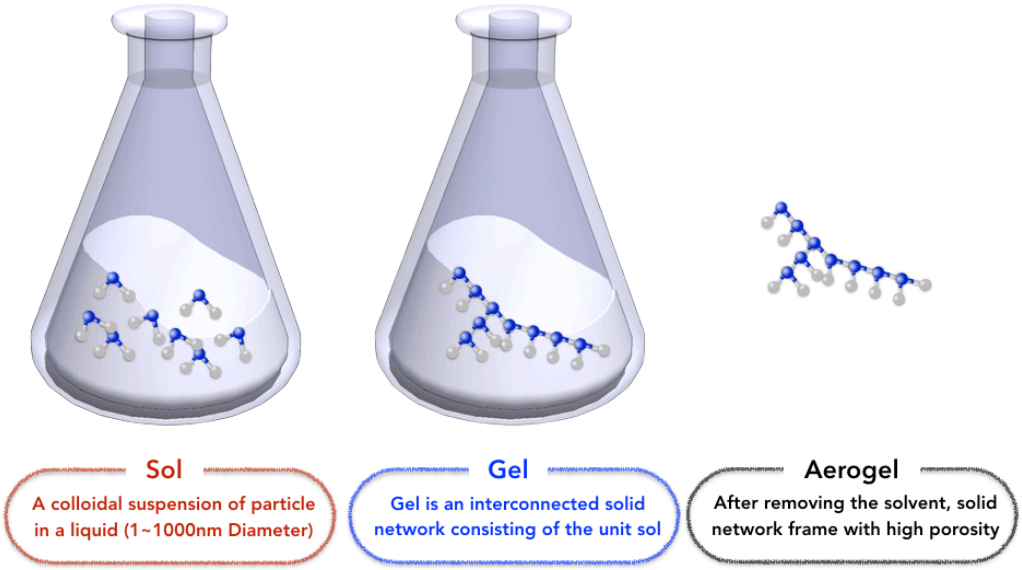

Figure 2.7 Simplified scheme of sol, gel and aerogel.

2.3.2. Solution processing route

A chemical deposition process begins with a precursor. The selection of precursors depends on the solvent and deposition process. Three types of metal salt precursors are most commonly employed for the solution process; acetates, nitrates and chlorides due to their cheap price and commercial availability. Combination of two or three different precursors can change the sol, pore and crystal size by improving the different chemical reactions. **Fig. 2.8** displays the typical solution deposition process.

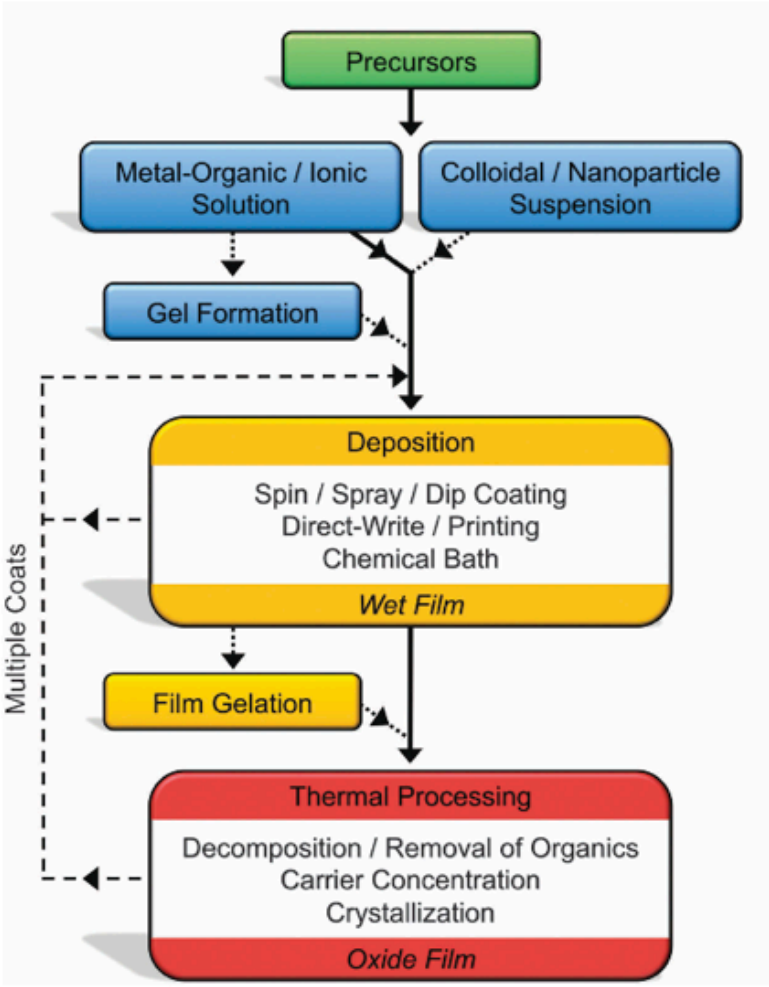

Figure 2.8 Flow chart of typical solution processing routes. Image taken from [15]

For making a stable sol, the selection of suitable solvent is important to each precursor. Solvent can be classified into polar, non-polar, protic (containing or can donate a hydrogen ion – a labile proton) or aprotic. In terms of solvation ability, there are three important characteristics of solvents; polarity, dipole moment, and the availability of labile protons. The ability to solvate polar or nonpolar species is mainly determined by the polarity of the solvent. Normally, the polar solvent can solvate polar species more easily and less polar solvent can be used for less polar species. The permanent dipole moment of a solvent determines how far the species can detect the surrounding species. For a solvent with lower dipole moment, it can sense the other species far more and has more effective electrostatic stabilization. The availability of labile protons is related with the solvation of anions or cations through hydrogen bonding. Whereas protic solvents can make hydronium ions more electrophilic, aprotic solvent can make hydroxyl ions more nucleophilic [28]. **Table 2.1** summarizes the physical properties of various solvents used in sol-gel processing.

Solvent	*Type*	*Molecular weight*	*Dielectric constant*	*Viscosity*	*Dipole moment*
Water (H_2O)		18.01	78.5	10.1	1.84
Methanol (CH_3OH)		32.04	32.6	5.4	1.70
Ethanol (C_2H_5OH)	Protic	46.07	24.3	10.8	1.69
2-ethoxyethanol ($C_4H_{10}O_2$)		90.12	-	-	2.08
Formamide (CH_3ON)		45.04	110	33.0	3.7
Dimethylformamide (C_3H_2NO)		73.10	36.7	7.96	3.86
Dioxane 1, 4 ($C_4H_8O_2$)	Aprotic	88.12	2.21	10.87	0
Tetrahydrofuran (C_4H_8O)		72.12	7.3	-	1.63

Table 2.1 Physical properties of various solvents.

In the formation of the coating solution, solution proceeds through three chemical reaction steps: Metal alkoxides formation, hydrolysis of metal alkoxides, and condensation. Metal alkoxide is an intermediate phase with the chemical formula $M(OR)_z$ when the alcohol is used as a solvent. Metal alkoxide is very reactive due to the presence of highly electronegative OR groups that stabilize M in its highest oxidation state and render M very susceptible to nucleophilic attack. During the hydrolysis process, charge will transfer from the filled '$3a_1$' bonding orbital (symmetric species of bonding orbital of water) of the water molecule to the empty '*d*' orbitals of the transition metal. The following equilibria show the hydrolysis process [29], [30]:

$$[M(OH_2)]^{Z+} \leftrightarrows [M-OH]^{(Z-1)+} + H^+ \leftrightarrows [M=O]^{(Z-2)+} + 2H^+ \tag{2-35}$$

Another chemical reaction is condensation and two nucleophilic mechanisms are involved in condensation process: nucleophilic substitution and nucleophilic addition.

$$M_1 - OX + M_2 - OY \rightarrow \underset{\underset{X}{|}}{M_1 - O} - M_2 + OY. \tag{2-36}$$

$$M_1 - OX + M_2 - OY \rightarrow \underset{\underset{X}{|}}{M_1 - O} - M_2 - OY. \tag{2-37}$$

Generally, the hydrolysis and condensation processes proceed continuously and quickly until interconnected networks are formed.

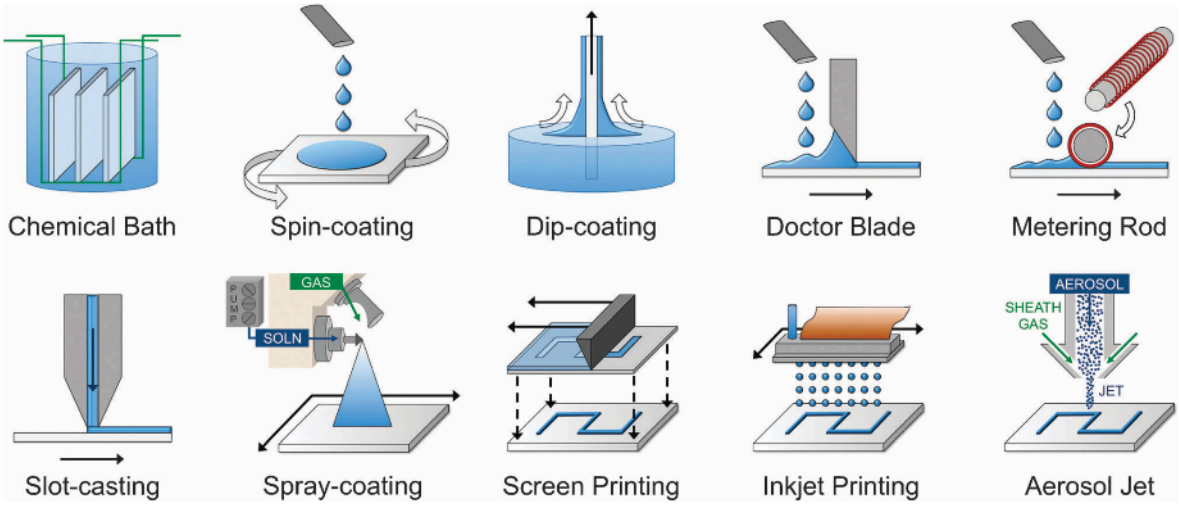

Figure 2.9 Flow chart of typical solution processing routes. Image taken from [15].

The sol-gel process allows for various film deposition methods at atmospheric pressure with low equipment cost since it does not require expensive vacuum chambers. For smaller and the laboratory-scale device processing, spin coating is the most popular method due to its simple and reproducible process. Spray-coating is also attractive for large scale devices and can be classified into two types of technique: a liquid coating method or a direct growth method (spray pyrolysis). Generally, an atomized droplet of solution can be generated by the pneumatic or ultrasonic method and then deposited onto a substrate with sheath gas. To obtain the uniformity of the thin film by using the spray coating process, there are several parameters to be considered such as viscosity, boiling point and surface tension. Perednis and Gauckler has reviewed the effect of parameters on film quality [31], and Patil has discussed the spray pyrolysis deposition of oxide thin films [32]. Recently, there has been a growing interest in spray-coating assisted by electric field due to their ability for liquid atomization and good uniformity on a surface [33]. For making a better film quality in the electrospray coating process, the mode of spraying is one important factor, and it differs during the process of meniscus formation and jetting from the meniscus [34]–[39]. Not only the process conditions such as electric field, ambient temperature, and humidity but also liquid properties such as conductivity, surface tension, and viscosity can affect the droplet size and the mode of spraying. Patterning by solution has traditionally been conducted by the screen printing process with a mask and direct-write methods such as inkjet printing or DOD (drop-on-demand) have attracted a lot attention due to the fast and cost effective process [40]. **Fig. 2.9** illustrates several solution coating and patterning techniques.

2.4. Fabrication process of the solution processed ATO thin films

2.4.1. Process overview

Fig. 2.10 shows the fabrication process flow for the solution-processed ATO thin films. As we discussed in the previous section, the choice of the precursor depends on many factors,

including solvent, formulation, and the specific processing routes. Chloride salts are one of the most commonly used materials as TCO precursors due to their low price and availability. As such, tin (II) chloride dehydrate ($SnCl_2$-$2H_2O$) and antimony (III) chloride ($SbCl_3$) were chosen as the starting materials. The coating solution was formulated by adding solvent and other additives with the precursors as the intermediate state called "alkoxides", compounds with formula also shown in **Fig. 2.10 (a)**. Two chemical reactions, "hydrolysis" and "condensation", were involved in the solution formulation and the coating process was then carried out. Among various coating techniques such as printing, spray coating and spin coating, we chose the spin coating process due to simplicity and reproducibility. A procedure of multiple spin coating was conducted on top of a glass substrate to increase the thickness of high quality thin films **(Fig. 2. 10 (B))**. Afterwards, the prototype samples were thermally annealed to decompose the precursors and remove organic residues in order to control the electronic carrier concentration. **Fig. 2. 10 (C)** shows a fabricated TCO sample placed on top of the printed UC seal to show their transparency using different ambient gases of N_2, O_2 and air during the annealing process. These optical photos demonstrate that these films are all transparent as the light can penetrate them.

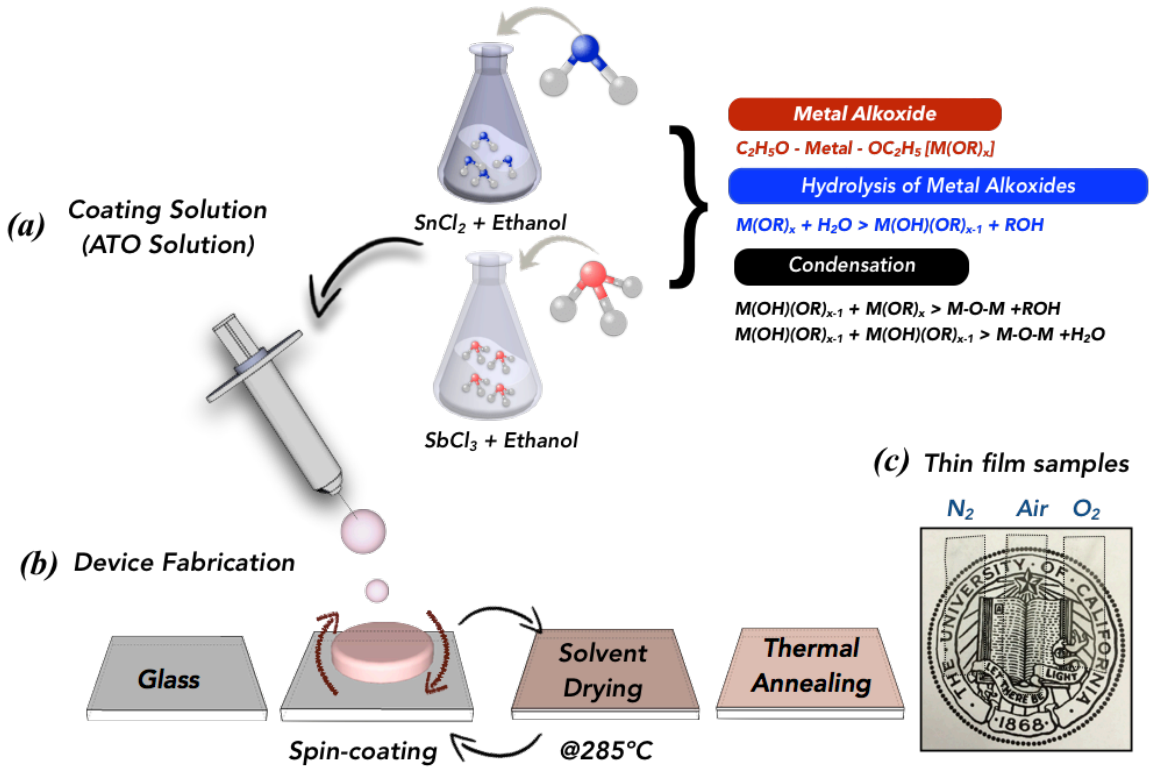

Figure 2.10 Schematics of solution process for making ATO thin films **(a)** Metal chloride salt precursors are mixed with alcohol. The mixture undergoes hydrolysis and condensation, resulting in the final coating solution **(b)** Solution deposition process using multiple spinning method. Subsequent thermal annealing densifies the thin films by decomposing the precursors and removing organic solvents. **(c)** Three fabricated transparent electrodes using different

annealing gases (N_2, Air and O_2) are placed on top of the printed UC seal to show their transparency.

2.4.2. Experiment

The solution process begins by mixing metal chloride precursors with ethanol. Tin (II) chloride dehydrate ($SnCl_2$-$2H_2O$, Sigma Aldrich) and antimony (III) chloride ($SbCl_3$, Sigma Aldrich) were dissolved separately in 10 ml of ethanol. The coating solution is prepared by adding variable amount of 0.1 M Antimony chloride solution to 10 mL of 0.1 M Tin chloride solution for controlling the dopant concentration. We prepared four different types of coating solutions with 6%, 8%, 10%, 12% Sb-doped concentrations. After adding the chloride salts into the ethanol, alkoxide is formed and followed by subsequent hydrolysis and condensation. Before starting the spin coating process, ultrasonic cleaning and surface treatment using ozone plasma were performed to increase the surface tension of the glass substrate. In order to make high quality ATO thin films, we introduced the multiple spin coating and solvent removal process. Each time, only a 10 nm-thick layer was coated onto the borosilicate glass substrate at 3000 rpm for 30 seconds and dried on top of a hotplate at 285^{o}C for 1 minute to remove solvents. In this multiple spin coating process, subsequent spin coatings filled pores left from the previous solvent drying process. By changing the number of the spin coating process, four different thicknesses (60nm, 90nm, 120nm, 150nm) of high quality ATO thin films were prepared. After depositing the final layer, the film is thermally annealed in different ambient gas environment (Thermo Electron Corp., model Lindberg/Blue M® three-zone tube) to densify the films by decomposing the precursors and removing the organic solvents. Three different gases (air, O_2 and N_2) and four different temperatures (300^{o}C, 400^{o}C, 500^{o}C and 600^{o}C) are investigated to study the effects on the electrical conductivity and optical transmittance.

2.5. Material characterization of solution processed ATO

2.5.1. Energy dispersive X-ray Spectroscopy (EDS) – Element analysis

Energy Dispersive X-Ray Spectroscopy (EDS) is a chemical element analysis technique used together with scanning electron microscopy (SEM). When the electron beams from the SEM bombard the sample, characteristic X-ray is radiated [41]. The initiation process of characteristic x-ray begins with the ejection of the electron from the inner shell to form a vacancy. An X-ray is generated with an energy equal to the difference between the energies of the electron shell [42]. The EDS technique characterizes the composition of elements by detecting the emitted characteristic X-rays from the sample. When an incident X-ray hits the detector, it creates the electrical charge which is proportional to the energy of the X-ray. The EDS X-ray detector measures the amplified electrical charge and evaluates the spectrum of the X-ray energy versus the counts of the emitted X-rays.

Fig. 2.11 shows the chemical composition of the ATO samples that contained mainly oxygen (O), silicon (Si) and tin (Sn), along with smaller amounts of other elements such as antimony (Sb)

and carbon (C). The presence of aluminum (Al) peaks in the EDS spectrum is owed to the boro-aluminosilicate glass substrate which contains aluminum oxide to enhance its thermal reliability. Two different thickness of samples were investigated (60nm, 120nm) and the other process conditions were the same (10% Sb doping, Annealed at 500ºC with oxygen rich environment). **Fig. 2.11** confirms that the solution process successfully synthesize the Sb doped Sn oxide thin films.

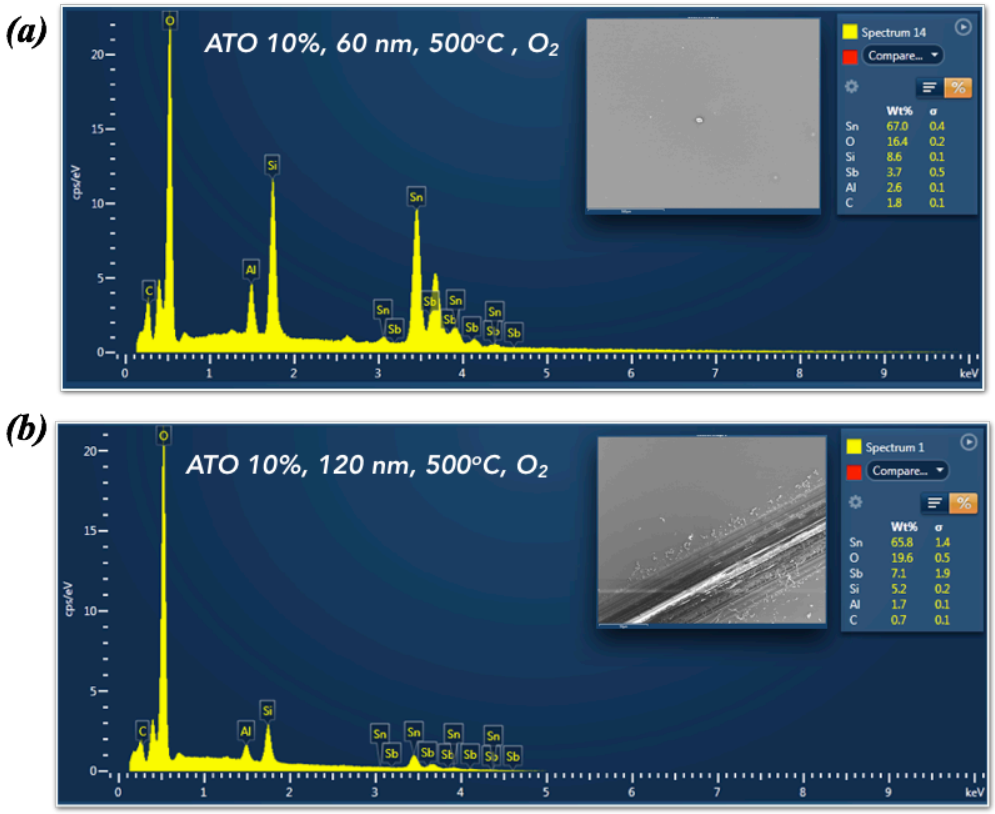

Figure 2.11 Energy dispersive X-ray spectroscopy (EDS) showing the chemical composition of ATO thin films and the inset shows the SEM images.

2.5.2. X-ray photoelectron spectroscopy (XPS) – Chemical composition and bonding states

X-ray photoelectron spectroscopy (XPS) is used to analyze the chemical composition and bonding states. **Fig. 2.12** shows the wide-energy range scan consisting of tin, antimony, oxygen, and carbon (surface impurities) peaks for the ATO samples prepared at different annealing temperatures. The binding energy scales have been referenced to the C1s orbital at 284.6 eV with the margin of error of ±0.6 eV.

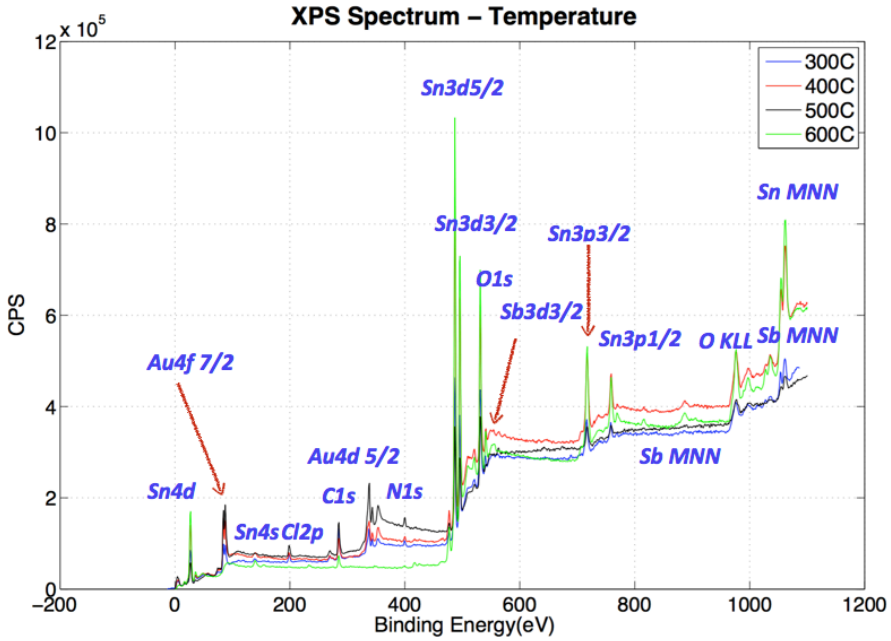

Figure 2.12 XPS survey scan of ATO thin films annealed at difference temperatures. The binding energy scales have been referenced to the C1s orbital at 284.6 eV.

Two sub-peaks in the binding energy of the Sb 3d orbital at 531.3 eV and 540.5 eV in **Fig. 2.13(a)** indicate the spin–orbit splitting due to the electromagnetic interaction. The spin–orbit split of 9.2 eV in the binding energy and peak positions demonstrate that the Sb species exist in the form of Sb^{+5}. For the Sb 3d5/2 and Sb 3d3/2 core levels, 0.4 eV of chemical shift toward the lower binding energy is observed repeatedly. The samples annealed at 400 ºC, 500 ºC, 600 ºC show higher binding energy than the sample annealed at 300 ºC, implying that Sb 3d decreases due to the oxidation, producing another chemical state of antimony, Sb^{+3}. **Fig. 2.13(b)** also shows the spin–orbit splitting and chemical shift of the Sn 3d core levels. The intensity peaks are found at 487.2 eV for Sn 3d5/2 and 495.7 eV for Sn3d3/2 for samples annealed at high temperatures (>300 ºC). This 8.5 eV of spin–orbit split for the Sn 3d core levels agrees well with those found in the literature [43], [44]. The smaller magnitude of spin–orbit splitting for Sn 3d as compared to that of Sb 3d is expected from the increased distance from the nucleus. On the other hand, the chemical shift of 0.6 eV in the Sn 3d peaks for the sample annealed at 300 ºC was larger than that of Sb 3d. This difference in the chemical shifts of Sb and Sn correlates with their oxidation states. The different valency directly affects the magnitude in the chemical shift by changing the total effective charge of elements [45], [46]. The obtained chemical shift and peak positions in this work agree with previous research [47] and indicate the existence of Sn^{+2}(SnO) in the sample annealed at 300 ºC and Sn^{+4}(SnO_2) species in samples going through higher temperature annealing processes. The material characterizations using XPS confirm that the minimum annealing temperature for forming highly conductive (Sb^{+5} ions in Sn^{+4} lattices), transparent ATO films in this work using the solution process is between 300 ºC and 400 ºC.

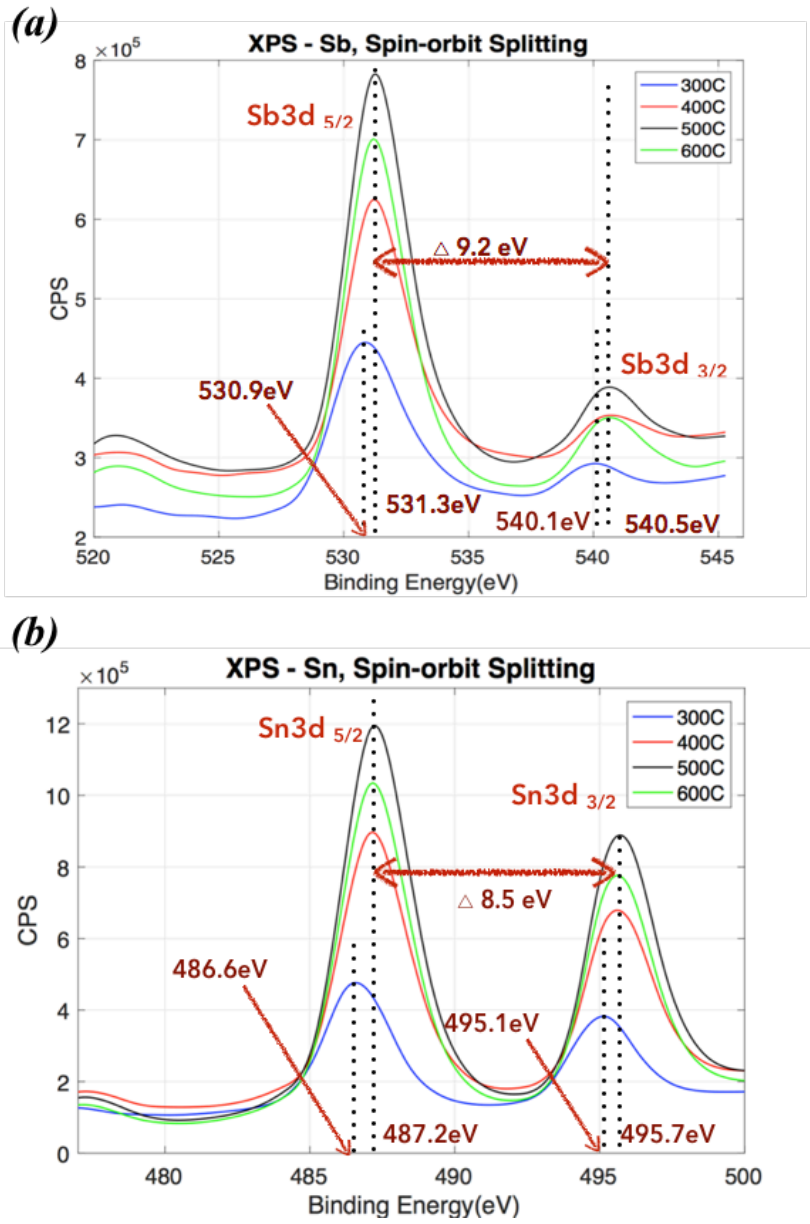

Figure. 2.13 (a) XPS core-level spectra of Sb 2d and **(b)** XPS core-level spectra of Sn 3d showing spin–orbit splitting and chemical shift in ATO samples annealed at different temperatures

2.5.3. Scanning electron microscopy (SEM) - surface morphology

Fig. 2. 14 illustrates the high magnification SEM (LEO 1550 Schottky field emission SEM) images of surface area of ATO thin films prepared with different annealing temperature, Sb doping concentration, ambient gases and thicknesses.

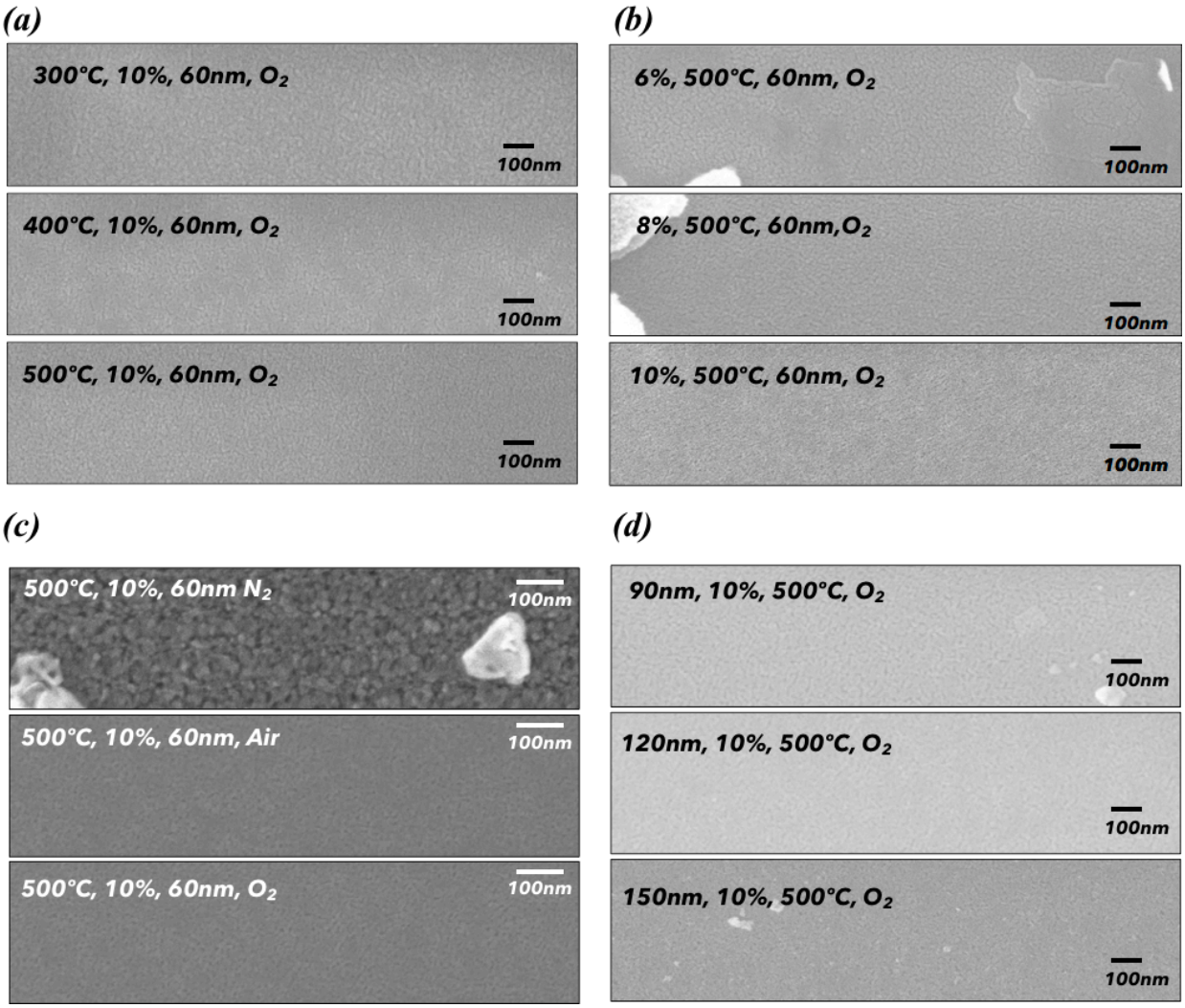

Figure. 2.14 SEM images of **(a)** 60nm-thick, 10% doping concentration ATO films annealed at different temperatures (300ºC, 400ºC, 500ºC) with oxygen-rich environment **(b)** ATO films different Sb-doping concentration (6%, 8%, 10% and 60nm-thick, annealed at 500ºC with oxygen-rich environment) **(c)** 60nm-thick, 10% doping concentration ATO films annealed at 500ºC with different ambient gases (N_2, Air, O_2) **(d)** 10% Sb-doping ATO films with different thicknesses (90nm, 120nm, 150nm), all samples are annealed at 500ºC with oxygen gas.

As the annealing temperature increased (300ºC, 400ºC, 500ºC, 600ºC) while the other parameters are fixed (60 nm-thick, 10% Sb doping concentration and oxygen-rich ambient gas), the particle sizes become slightly smaller and more densely packed surface morphology is observed (**Fig. 2. 14 (a)**). This observation explains that the changes in surface morphology do not arise from the grain size differences but from the densification of porosity in ATO thin films. Generally, grain size becomes larger as the annealing temperature increases and larger grain size of solidified structures should have higher conductivity than the smaller grain sized ones due to less electron scattering [48]. However, since the smaller surface morphologies in the ATO samples annealed at high temperature result from the decomposition of precursors and removal

of residual organic solvents, it is therefore expected that the lower resistance for the sample annealed at high temperature and confirmed by the sheet resistance measurement.

Fig. 2.14 (b) displays the high magnification SEM images of ATO samples with different Sb doping concentration (6%, 8%, 10% and 60 nm-thick, annealed at 500ºC with O_2). The smaller surface morphology in the high doping concentration sample was observed but no substantial differences were observed. **Fig. 2.14 (c)** compares the SEM images of 60 nm-thick, 10% Sb doping ATO samples annealed at 500ºC with different ambient gases (nitrogen, air and oxygen). It is found that under the nitrogen environment, large particles ~20 nm in size can be seen uniformly distributed on the surface. On the other hand, as the oxygen content increases, the particle size becomes smaller in the air and O_2 environment. Unlike the other parameters, no surface morphology changes were found for the samples with different thicknesses **(Fig. 2.14 (d))**. For the general thin films, the grain size becomes larger as the thickness increases during the thermal annealing process; this result also explains that the changes in surface morphology dose not arise from the grain size differences.

2.6. Electrical and optical characteristics of solution processed ATO

2.6.1. The effects of doping concentrations

Fig. 2.15 shows the optical transmittance spectra tests acquired from each prototype sample groups with different doping concentrations. The base condition is 500ºC of annealing temperature and 60 nm in thickness; and oxygen as the annealing gas environment. It is found that all samples have very good transmittance with around 95% at 550 nm, which is comparable to that of commercially available sputtered ITO thin films [16]. Furthermore, **Fig. 2. 15** clearly shows that transmittance is related to the doping concentration and the increase in Sb-doping concentration in the ATO films results in the decrease of transmittance. This measurement result can be explained via relationship between the absorption coefficient and free carrier density, *n* [49].

$$\alpha = \frac{\omega}{c}\sqrt{\frac{8\pi n e^2 \tau}{m\omega}} \tag{2-38}$$

Where ω, c, m, and τ represent the frequency of the incident light wave, the speed of light, the effective mass of free carriers and relaxation time. Consequently, as the free carrier density in the material increases, the absorption coefficient also increases and, therefore, the transmittance of the material attenuates.

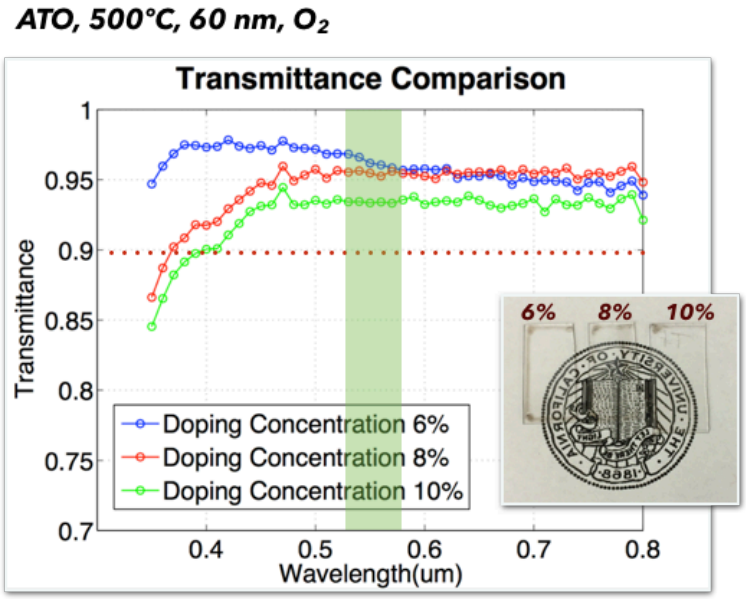

Figure 2.15 Measured optical transmittance spectra of ATO thin films from 350 to 800nm: comparison of different doping concentrations of 6%, 8% and 10%. The inset shows the fabricated samples on top of printed UC Seal on a paper.

Figure 2.16 (a) shows that the measured sheet resistance (R_s) decreases proportionally as the Sb-doping concentration increases. Since we measured the thickness of the ATO samples, this sheet resistance can be easily converted to the electrical conductivity by using the following equation

$$R = \left(\frac{\rho}{t}\right)\left(\frac{L}{W}\right) = R_S\left(\frac{L}{w}\right) \tag{2-39}$$

$$\sigma = \frac{1}{R_S \cdot t} \tag{2-40}$$

where 'ρ' is the material's resistivity (the reciprocal of conductivity 'σ') and 't' is the thickness of the sample. **Fig. 2. 16 (b)** indicates that the converted electrical conductivity increases with increasing Sb-doping concentration. This trend can be explained via the **Eq. (2-8)** in which the electrical conductivity is proportional to the free carrier concentration and implies solution-processed ATO films are conductive enough to act as transparent conductive electrodes (>10,000 S/m).

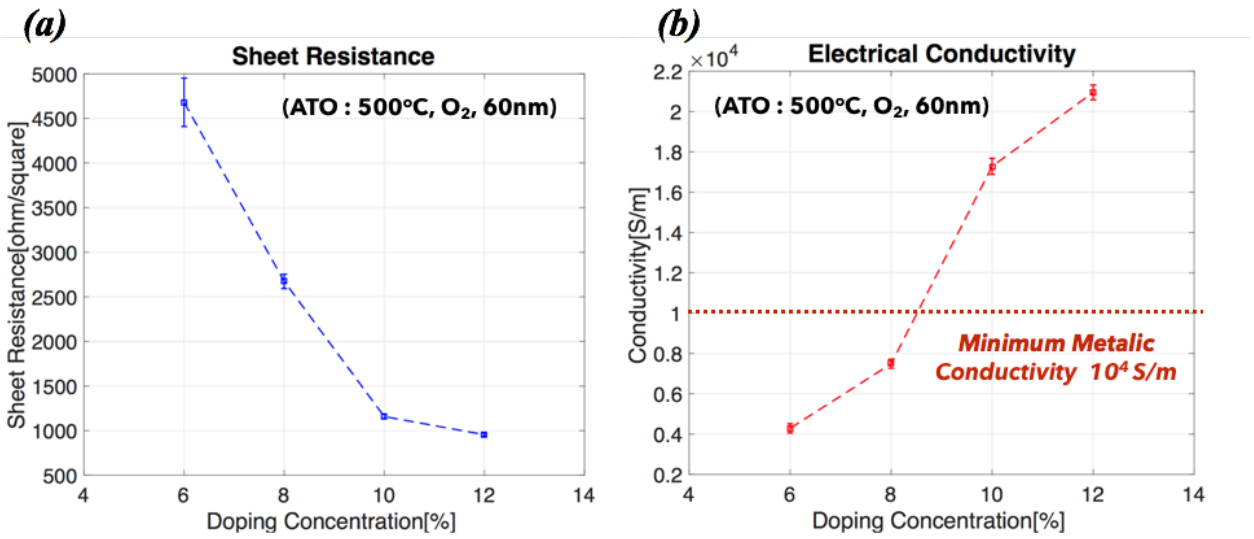

Figure 2.16 Measured sheet resistance/electrical conductivity of the 60nm-thick ATO samples of different Sb-doping concentration. All samples are annealed at 500ºC with oxygen.

2.6.2. The effects of annealing temperatures

Fig. 2.17 shows the optical transmittance spectra measurement of 10% Sb-doping concentration, 60 nm-thick of ATO samples annealed at different annealing temperatures (300ºC, 400ºC, 500ºC, 600ºC) in an oxygen-rich environment. It also clearly shows that all samples have very good transmittance over 90% at 550 nm; This is comparable to commercial, vacuum-processed ITO films of similar thickness. In **Fig. 2.17**, transmittance is enhanced slightly as the

annealing temperature is raised (<5% increase), which is attributed to the increase in the oxygen content of ATO samples.

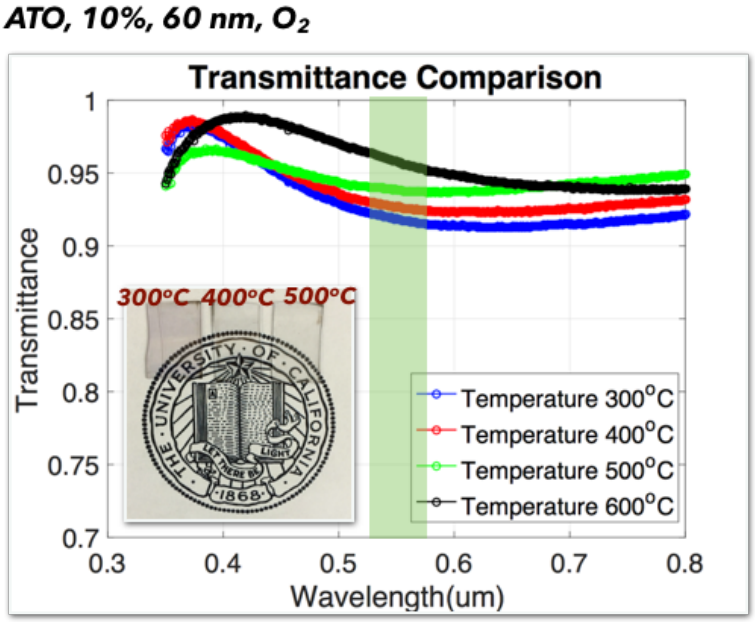

Figure 2.17 Measured optical transmittance spectra of ATO thin films from 350 to 800nm: comparison of different annealing temperature of 300ºC, 400ºC, 500ºC, and 600ºC. The inset shows the fabricated samples on top of printed UC Seal on a paper.

Figure 2.18 illustrates that the measured sheet resistance and electrical conductivity. Unlike the ATO samples annealed over 400ºC, the electrical conductivity for the sample annealed at 300ºC has not been measured due to its high resistance. As we already discussed, to synthesize the conductive ATO thin films, the presence of Sb^{+5} ions in Sn^{+4} lattice is required. Formation of Sb^{+5} from the Sb^{+3} species depends on the annealing temperature. By observing the chemical shift of spin-orbit splitting of Sn and Sb using XPS, we confirm that the minimum annealing temperature for synthesizing highly conductive and transparent ATO thin films using sol-gel method is between 300ºC and 400ºC. **Fig. 2.18 (b)** displays that the electrical conductivity increases with increasing thermal annealing temperature. This tendency can be also explained using the **Eq. (2-8)**. As the annealing temperature increases, the number of Sb^{+5} species also increases due to the oxidation and, thus, more free carriers are generated. Consequently, ATO films annealed at high temperature show high conductivity due to the free carrier generation. But the annealing temperature will be limited by the glass transition temperature (T_g) of the glass substrate.

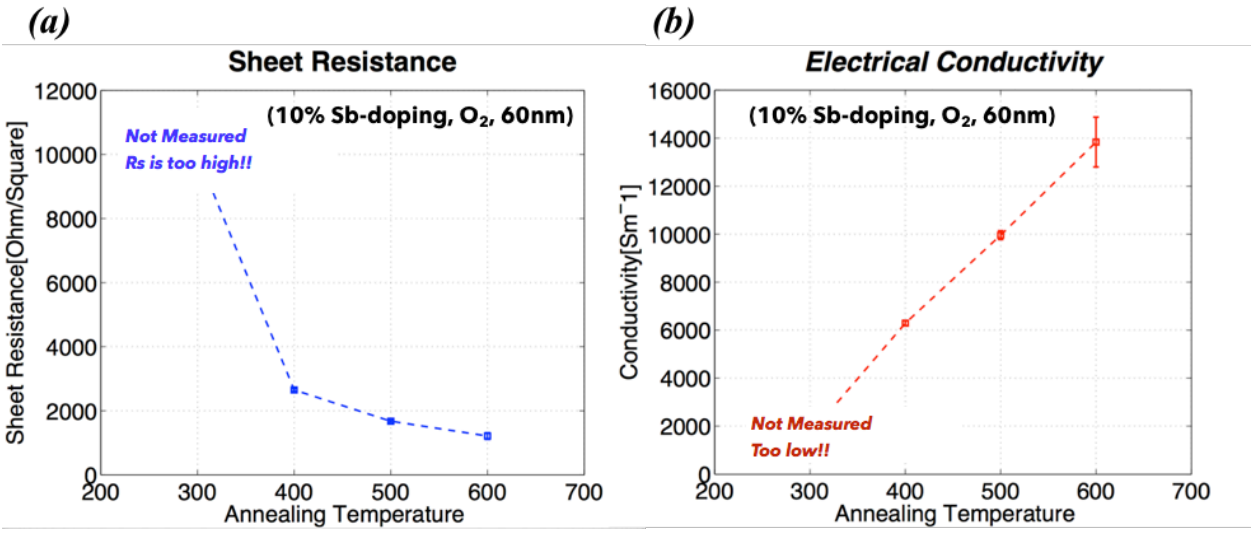

Figure 2.18 Measured sheet resistance/electrical conductivity of the 60nm-thick, 10% Sb-doping concentration ATO samples annealed at different temperature with oxygen-rich environment.

2.6.3. The effects of ambient gases

The optical transmittance spectra of the ATO samples (60 nm thick) with different ambient gases is shown in **Fig. 2.19**. ATO films of 10% Sb-doping concentration were deposited by the multiple spin coating process and then annealed at 500ºC in the furnace for an hour. Even though all samples have good optical transmittance over 90% at 550 nm, relatively lower transmittance was observed in the sample annealed with nitrogen gas. This measurement results indicates that transmittance is related to the oxygen contents and the increase in oxygen content in the ATO films results in the enhancement of transmittance.

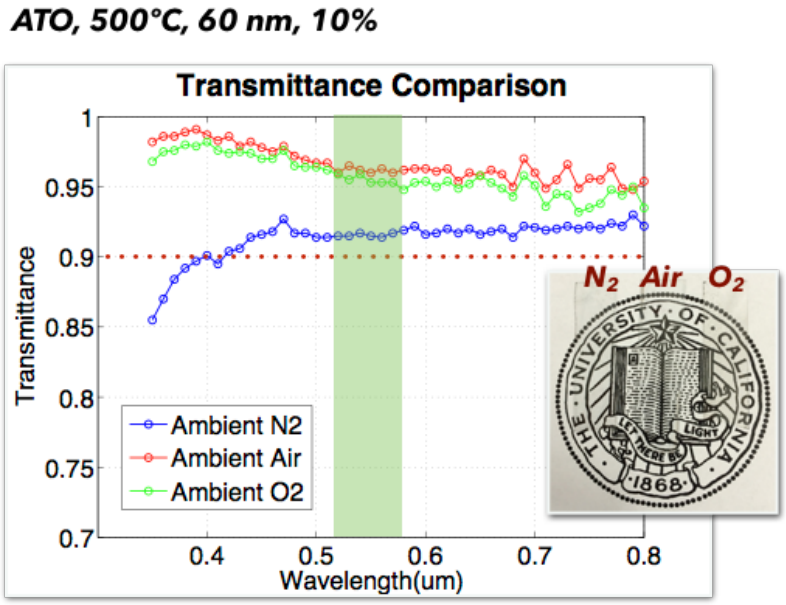

Figure 2.19 Measured optical transmittance spectra of ATO thin films from 350 to 800nm: comparison of different ambient gas during the thermal annealing. The inset shows the fabricated samples on top of printed UC Seal on a paper.

The variation in sheet resistance and electrical conductivity of the ATO thin films with different ambient gases (N_2, Air, O_2) during the thermal annealing process is summarized in **Fig. 2.20.** As we discussed in section 2.2, there are two types of free carrier generation, intrinsic carrier formation and extrinsic carrier formation. For the pure metal oxide material such as ZnO, SnO and In_2O_3, introducing oxygen vacancies into material is the main carrier generation mechanism, thus, decreasing oxygen partial pressure (*e. g.* with N_2 or forming gas) during the film deposition process or thermal annealing process can enhance the electrical conductivity by generating more oxygen vacancies in the material. However, for the binary metal oxide material such as ATO, the free carriers are mainly formed by introducing substitutional atoms, therefore, the amount of free carrier generation is proportional to the amount of Sb^{+5} oxidized from Sb^{+3} in the samples. Consequently, thin film deposition or thermal annealing with an increased oxygen partial pressure environment can enhance the electrical conductivity of the ATO thin films by introducing more carriers. **Fig. 2.20** clearly shows that the increased oxygen partial pressure environment (*e. g.* with Air or O_2) during the thermal annealing process increased the electrical conductivity of the solution processed ATO thin films 2 to 3 times.

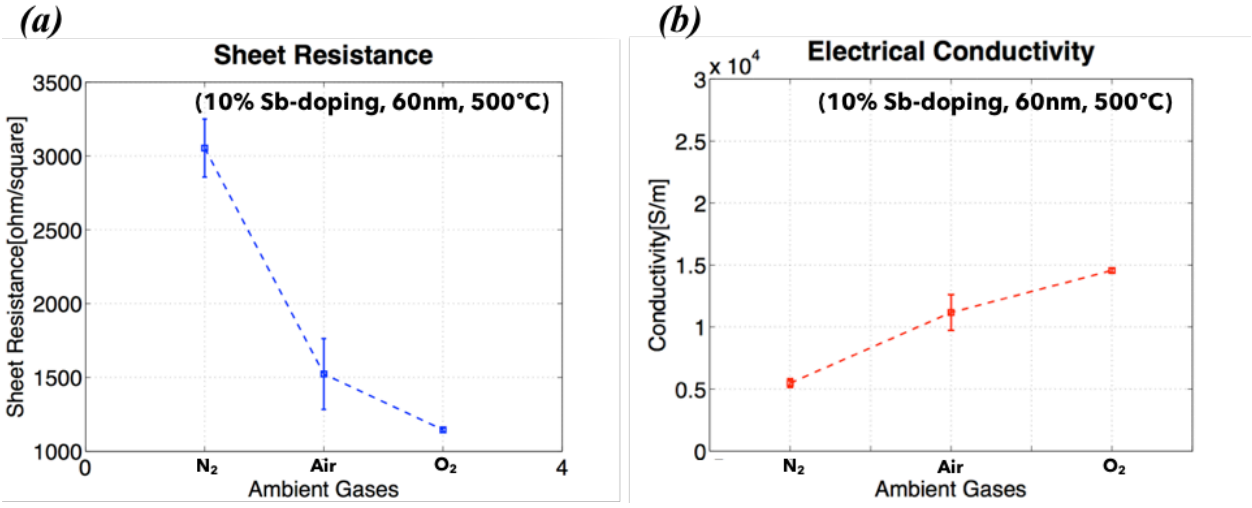

Figure 2.20 Measured sheet resistance/electrical conductivity of the 60nm-thick, 10% Sb-doping concentration ATO samples annealed at 500ºC with different ambient gases

2.6.4. The effects of thickness of thin films

Fig. 2.21 displays that the optical transmittance spectra of the ATO samples (10% Sb-doping, O_2, 500ºC) with various thickness. Even though all samples have good optical transmittance over 90% at 550 nm, relatively lower transmittance was observed in the sample annealed with nitrogen gas. This measurement results indicate that transmittance is related to the oxygen content. It shows that all ATO samples show good optical transmittance over 90% at 550 nm and are comparable with commercial ITO thin films. Even though there is no substantial difference in the transmittance obtained by varying the thickness of the ATO thin films. It shows that the transmittance for the ATO thin film with 150 nm thickness is slightly decreased. This attenuation in transmittance with the increasing thickness of the sample can be explained by using the Beer Lambert law as follows:

$$I(z) = I_0 e^{-\alpha(\omega)z} \tag{2-41}$$

where *I(z)* is the light intensity after traveling a thickness, z, of material as compared with the incident intensity, I_0, and 'α' is the absorption coefficient. This equation explains how the intensity of the incident light attenuates through the material the light is travelling. The absorption coefficient is dependent on the free carrier density, direct inter-band transitions, and indirect inter-band transitions [50].

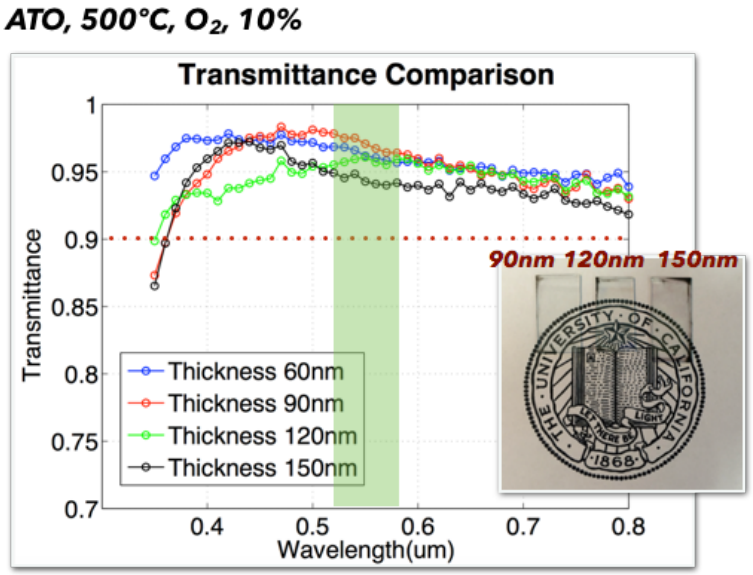

Figure 2.21 Measured optical transmittance spectra of ATO thin films from 350 to 800nm: comparison of different thickness of thin films. The inset shows the fabricated samples on top of printed UC Seal on a paper.

Figure 2.22 shows that the measured sheet resistances and electrical conductivities of the ATO samples with various thicknesses. It indicates that the sheet resistance of the ATO samples decreases proportionally as the thickness increases. This trend can be easily explained by using Ohm's law in which the resistance of the material is inversely proportional to the cross-sectional area of the material. However, unlike other process parameters such as the Sb-doping concentrations, the annealing temperatures, and the ambient gases, the changes in conductivity due to changes in thickness of the ATO sample are negligible. This measurement result reveals that the thickness of the sample is not a factor for affecting the grain size in the material and, thus, no enhancement of the electrical conductivity is found. This observation also explains that no surface morphology changes are found for the samples in the previous SEM measurement. Consequently, it is found that the thickness of the ATO thin film is not a process parameter which can affect the electrical characteristics.

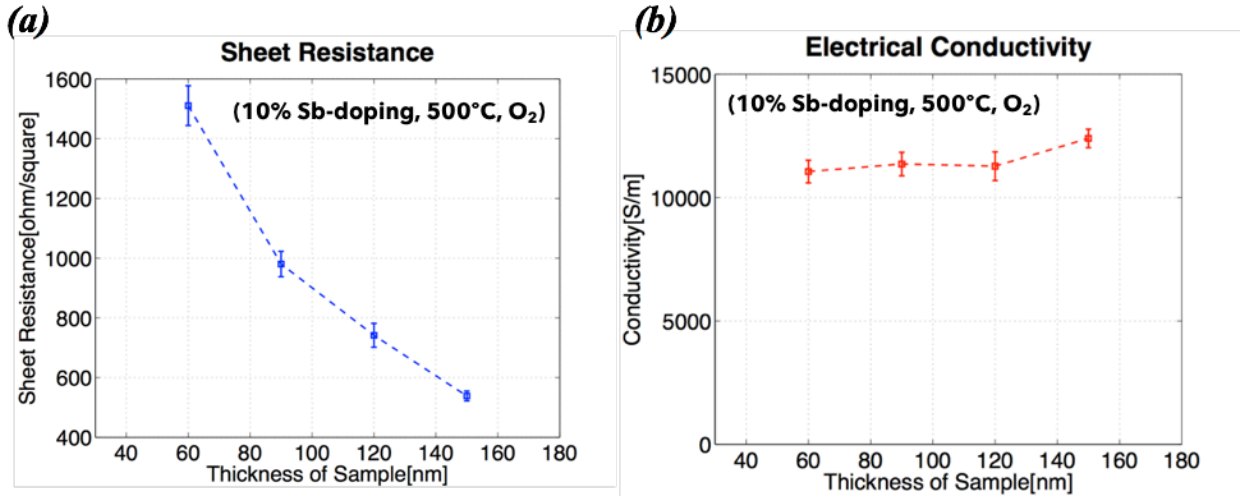

Figure 2.22 Measured sheet resistance/electrical conductivity of the 10% Sb-doping concentration ATO samples annealed at 500ºC in oxygen-rich environment with various thicknesses.

2.7. Summary

In this chapter, we introduced the properties of TCO materials, the solution processes and the basic theory used for the sol-gel process in this thesis work. Next, we discussed the design, fabrication and experimental characterization processes for the transparent ATO films. The solution-processed ATO thin films are introduced for outdoor opto-electronic applications where the conventional transparent films such as ITO have reliability issues. Highly transparent (~95%) and metallic (~20000 S/m) thin films with a thickness of 60-150 nm have been fabricated using a solution-based process. For making high quality ATO thin films, multiple spin-coating was introduced. A parametric study has been performed on four key process factors: doping concentration, thickness, ambient gas and temperature, in order to achieve high electrical conductivity and transparency. Studies on the surface morphology, crystallinity, electrical, and optical properties of prototype ATO films have also been conducted. These investigation results provide useful information for future research directions, namely, to enhance the conductivity of the ATO films by improving the crystallinity. In summary, the ATO thin film fabrication process is simple, fast and effective for potential applications in the area of emerging opto-electronic devices

2.8. References

[1] H. L. Hartnagel, A. L. Dawar, A. K. Jain, and C. Jagadish, *Semiconducting Transparent Thin Films*. Institute of Physics Publishing, 1995.

[2] D. Ginley and C. Bright, "Transparent onducting O xides," *MRS Bull.*, pp. 15–18, 2000.

[3] B. G. Lewis and D. C. Paine, “Applications and Processing of Transparent Conducting Oxides,” *MRS Bull.*, vol. 25, no. 8, pp. 22–27, 2000.
[4] K. Ellmer, “Resistivity of polycrystalline zinc oxide films: current status and physical limit,” *J. Phys. D. Appl. Phys.*, 2001.
[5] J. W. Fergus, “Doping and defect association in oxides for use in oxygen sensors,” *J. Mater. Sci.*, vol. 38, no. 21, pp. 4259–4270, 2003.
[6] J. F. Wager, “15 . 1 : Invited Paper : Amorphous Oxide Semiconductor Thin-Film Transistors : Performance & Manufacturability for Display Applications,” *SID*, pp. 181–183, 2009.
[7] T. M. Coughlin, *Digital Stroage in Consumer Electronics*. Oxford: Elsevier, 2007.
[8] T. Minami, “Transparent conducting oxide semiconductors for transparent electrodes,” *Semicond. Sci. Technol.*, vol. 20, no. 4, pp. S35–S44, 2005.
[9] J. Hu and R. G. Gordon, “Textured fluorine-doped ZnO films by atmospheric pressure chemical vapor deposition and their use in amorphous silicon solar cells,” *Sol. Cells*, vol. 30, no. 1–4, pp. 437–450, 1991.
[10] J. M. McGraw, P. A. Parilla, D. L. Schulz, J. Alleman, X. Wu, W. P. Mulligan, D. S. Ginley, and T. J. Coutts, “Pulsed laser deposition of cadmium stannate, a spinel-type transparent conducting oxide,” *Mater. Res. Soc. Symp. - Proc.*, vol. 388, pp. 51–56, 1995.
[11] D. J. Seo and S. H. Park, “Structural, electrical and optical properties of In2O3:Mo films deposited by spray pyrolysis,” *Phys. B Condens. Matter*, vol. 357, no. 3–4, pp. 420–427, 2005.
[12] B. R. Koo and H. J. Ahn, “Structural, electrical, and optical properties of Sb-doped SnO2 transparent conductive oxides fabricated using an electrospray technique,” *Ceram. Int.*, vol. 40, no. 3, pp. 4375–4381, 2014.
[13] H. B. Lee S.U., “Effects of annealing on the characteristics of ATO films prepared by using the RF magnetron sputtering method for transparent electrodes,” *J. Korean Phys. Soc.*, vol. 55, no. 5 PART 1, pp. 1915–1919, 2009.
[14] T. R. Giraldi, M. T. Escote, M. I. B. Bernardi, V. Bouquet, E. R. Leite, E. Longo, and J. A. Varela, “Effect of thickness on the electrical and optical properties of Sb doped SnO2 (ATO) thin films,” *J. Electroceramics*, vol. 13, no. 1–3, pp. 159–165, 2004.
[15] R. M. Pasquarelli, D. S. Ginley, and R. O’Hayre, “Solution processing of transparent conductors: from flask to film,” *Chem. Soc. Rev.*, vol. 40, no. 11, p. 5406, 2011.
[16] R. N. Chauhan, C. Singh, R. S. Anand, and J. Kumar, “Effect of sheet resistance and morphology of ITO thin films on polymer solar cell characteristics,” *Int. J. Photoenergy*, vol. 2012, 2012.
[17] E. K. Shokr, M. M. Wakkad, H. a. Abd El-Ghanny, and H. M. Ali, “Sb-doping effects on optical and electrical parameters of SnO2 films,” *J. Phys. Chem. Solids*, vol. 61, no. 1, pp. 75–85, 2000.

[18] C. Kittel, *Introduction to Solid State Physics, 8th edition*, 8th ed. New York: John Wiley and Sons, 2005.
[19] K. Nomura, H. Ohta, A. Takagi, T. Kamiya, M. Hirano, and H. Hosono, "Room-temperature fabrication of transparent flexible thin-film transistors using amorphous oxide semiconductors," *Nature*, vol. 432, no. 7016, pp. 488–492, 2004.
[20] T. Kamiya, K. Nomura, and H. Hosono, "Origins of High Mobility and Low Operation Voltage of Amorphous Oxide TFTs: Electronic Structure, Electron Transport, Defects and Doping," *J. Disp. Technol.*, vol. 5, no. 7, pp. 273–288, 2009.
[21] X. Yul, T. J. Marks, and A. Facchetti, "Metal oxides for optoelectronic applications," *Nat. Mater.*, vol. 15, no. 4, pp. 383–396, 2016.
[22] N. F. Mott, "Silicon dioxide and the chalcogenide semiconductors; similarities and differences," *Adv. Phys.*, vol. 26, no. 4, pp. 363–391, 1977.
[23] S. Narushima, M. Orita, M. Hirano, and H. Hosono, "Electronic structure and transport properties in the transparent amorphous oxide semiconductor 2CdO · GeO2," *Phys. Rev. B*, vol. 66, no. 3, p. 35203, 2002.
[24] E. D. Palik, *Handbook of Optical Constants of Solids*. Academic Press NY, 1985.
[25] C. G. Van De Walle, "Universal alignment of hydrogen levels in semiconductors and insulators," *Phys. B Condens. Matter*, vol. 376–377, no. 1, pp. 1–6, 2006.
[26] D. J. Griffiths, *Introduction to Electrodynamics*, 4th ed. Prentice Hall.
[27] T. Nakada, Y. Hirabayashi, T. Tokado, D. Ohmori, and T. Mise, "Novel device structure for Cu(In,Ga)Se2 thin film solar cells using transparent conducting oxide back and front contacts," *Sol. Energy*, vol. 77, no. 6, pp. 739–747, 2004.
[28] C. J. Brinker and G. W. Scherer, *Sol-Gel Science*. San Diego: Academic Press INC, 1990.
[29] J. Livage, M. Henry, and C. Sanchez, "Sol-gel chemistry of transition metal oxides," *Prog. Solid State Chem.*, vol. 18, no. 4, pp. 259–341, 1988.
[30] R. Papiernik, L. G. Hubert-pfalzgraf, M. C. Henriques, and B. Goncalves, "Synthesis and characterization of new titanium hexanuclear oxo carboxylato alkoxides.," *J. Chem. Soc. Dalt. Trans.*, vol. 6, no. 186, pp. 2285–2287, 1998.
[31] D. Perednis and L. J. Gauckler, "Thin Film Deposition Using Spray Pyrolysis," *J. Electroceramics*, pp. 103–111, 2005.
[32] P. S. Patil, "Versatility of chemical spray pyrolysis technique," *Mater. Chem. Phys.*, vol. 59, no. 3, pp. 185–198, 1999.
[33] C. H. Park and J. Lee, "Effects of expandable graphite and modified ammonium polyphosphate on the flame-retardant and mechanical properties of wood flour-polypropylene composites," *Polym. Polym. Compos.*, vol. 21, no. 7, pp. 449–456, 2013.
[34] M. Cloupeau and B. Prunet-Foch, "Electrostatic spraying of liquids: Main functioning modes," *J. Electrostat.*, vol. 25, no. 2, pp. 165–184, 1990.
[35] M. Cloupeau and B. Prunet-Foch, "Electrohydrodynamic spraying functioning modes: a critical review," *J. Aerosol Sci.*, vol. 25, no. 6, pp. 1021–1036, 1994.

[36] A. Jaworek and A. Krupa, “Classification of the modes of EHD spraying,” *J. Aerosol Sci.*, vol. 30, no. 7, pp. 873–893, 1999.
[37] A. Jaworek and A. Krupa, “Jet and drops formation in electrohydrodynamic spraying of liquids. A systematic approach,” *Exp. Fluids*, vol. 27, no. 1, pp. 43–52, 1999.
[38] I. Hayati, A. Bailey, and T. . Tadros, “Investigations into the mechanism of electrohydrodynamic spraying of liquids,” *J. Colloid Interface Sci.*, vol. 117, no. 1, pp. 205–221, 1987.
[39] I. Hayati, A. Bailey, and T. F. Tadros, “Investigations into the mechanism of electrohydrodynamic spraying of liquids. II. Mechanism of stable jet formation and electrical forces acting on a liquid cone,” *J. Colloid Interface Sci.*, vol. 117, no. 1, pp. 222–230, 1987.
[40] S. Magdassi, *The Chemistry of Inkjet Inks*. World Scientific Publishing Co, 2010.
[41] K. Kenneth, *Modern Physics*. John Wiley and Sons, 1983.
[42] L. C. Wagner, *Failure Analysis of Integrated Circuit*. Springer, 1999.
[43] S. J. Gnanamuthu, I. K. Punithavathy, S. J. Jeyakumar, K. Usharani, and A. R. Balu, “Properties of nanostructured Ni-doped Sn_2S_3 thin films – doping concentration effect,” *Mater. Res. Innov.*, vol. 20, no. 5, pp. 395–399, 2016.
[44] J. M. Themlin, M. Chtaïb, L. Henrard, P. Lambin, J. Darville, and J. M. Gilles, “Characterization of tin oxides by x-ray-photoemission spectroscopy,” *Phys. Rev. B*, vol. 46, no. 4, pp. 2460–2466, 1992.
[45] C. L. Lau, “Oxidation of tin: An ESCA study,” *J. Vac. Sci. Technol.*, vol. 15, no. 2, p. 622, 1978.
[46] R. Izquierdo, E. Sacher, and A. Yelon, “X-ray photoelectron spectra of antimony oxides,” *Appl. Surf. Sci.*, vol. 40, no. 1–2, pp. 175–177, 1989.
[47] M. Fondell, M. Gorgoi, M. Boman, and A. Lindblad, “An HAXPES study of Sn, SnS, SnO and SnO2,” *J. Electron Spectros. Relat. Phenomena*, vol. 195, pp. 195–199, 2014.
[48] A. F. Mayadas and M. Shatzkes, “Electrical-resistivity model for polycrystalline films: The case of arbitrary reflection at external surfaces,” *Phys. Rev. B*, vol. 1, no. 4, pp. 1382–1389, 1970.
[49] A. M. Fox, *Optical Properties of Solids*. New York: Oxford university press, 2001.

Chapter 3. Improved Mechanical Flexibility of Solution Processed Sb-doped Tin Oxide Films

3.1. Overview

As discussed in the previous chapter, solution processed ATO films have several attractive features: (1) it does not use the expensive rare earth material, indium, nor the expensive vacuum-based processes; (2) ATO is both chemically and thermally stable among various TCO materials. However, past research has only focused on its electrical and optical properties, without detailed studies on mechanical properties and stress analyses. Since vacuum-process TCO materials generally have limited mechanical flexibility and stress tolerance, they are not suitable for optoelectronic devices operating environments.

In this chapter, we present improved mechanical flexibility of solution-processed conductive oxide thin films. We first introduce the nano indentation technique (Berkovich tip indenter) to measure the elastic modulus and hardness of thin films. Next, the extracted elastic modulus of the oxide thin films is compared with that of the conventional vacuum processed ITO thin films and finite element analysis (FEA) is performed to compare the stress responses under a 4-point-bending simulation. Finally, the electrical performance changes under the mechanical loads are discussed.

3.2. Nano indentation

3.2.1. Introduction

One popular method of measuring mechanical properties (elastic modulus, hardness) of thin films is to make a small deformation on the surface of the sample. Nanoindentation, with a sharp indenter, has been an attractive technology for measuring the mechanical properties of thin films [1]–[3]. There are two advantages to using the nanoindentation system. First, various mechanical properties can be investigated without separating the film from the substrate for easy sample preparation. Second, it has the ability to investigate the surface at multiple points and draw a map of mechanical properties. As such, the nanoindentation technology has been applied to many research fields such as hard coatings, optical coatings and laser treatments [4], [5]. **Fig. 3.1** shows the multiple indentation marks in a microelectronic device.

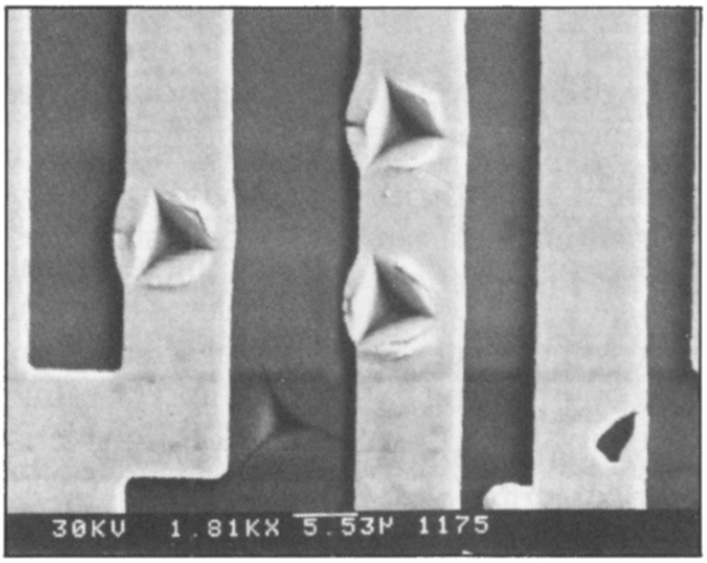

Figure 3.1 Nano indentation places at several selected points in a microelectronic device. Image taken from [6].

The Berkovich, Vickers and conical indentation are the typical indenter shapes and various reports have been published on the influence of their geometrical shape on the load-indentation depth results [7], [8]. **Fig. 3.2** shows the various geometry of the tips of the indenters. The most popular indenter is the Berkovich diamond, which has a triangular shape with the same depth-to-area ratio. The Berkovich indenter is preferred than the Vickers indenter due to the ease in grinding the three-sided faces.

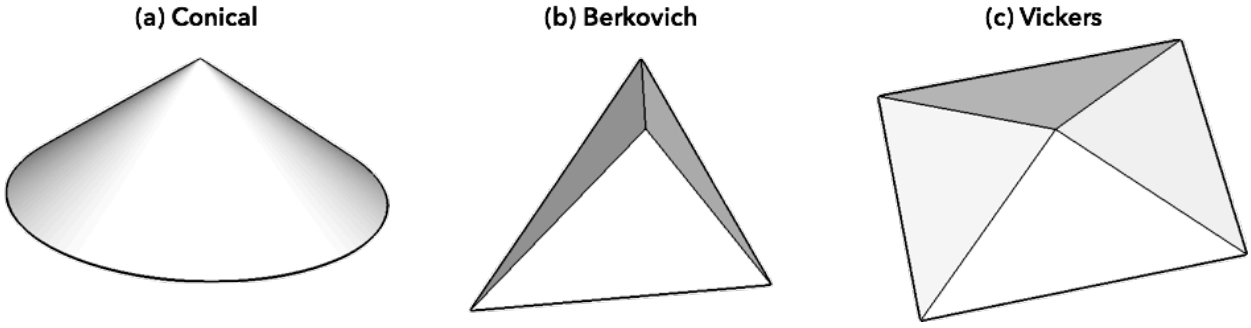

Figure 3.2 Various shapes of the indenter tips.

For these indenter tips, the specimen is expected to be under elastic and plastic deformation due to the permanent hardening of the specimen. During the nanoindentation measurements, the contact area is initially small and constantly changes as the indenter penetrates into the specimen; only the elastic displacements are recovered during unloading. Even though the behavior of the sharp indenter tip has more complexity in analyzing the measurement data, there are two reasons for having sharp indenter tips in the nanoindentation system. First, a high degree of spatial resolution can be achieved by making the contact area as small as possible. Second, with a flat-ended indenter tip, it is hard to assure the uniformity between the tip and the specimen due to the misalignment of the indenter tip and the surface roughness of the specimen.

Fig. 3.3 shows the schematic of a typical nanoindentation load-displacement data set obtained with a Berkovich indenter. There are three critical quantities that need to be characterized from the P–h curves: the maximum indentation load, P_{max}, the displacement at the peak load, h_{max}, and the initial contact elastic stiffness, $S=dP/dh$ (i.e., the slope of the initial portion of the unloading curve). Other key quantities are the displacement found by linearly extrapolating the initial portion of the unloading curve to zero load, h_o, and the final depth, h_f, or the permanent penetration depth after the indenter is fully unloaded. In the early experiments of nanoindentation [9], [10], one important observation is that the resulting deformation by the indenter tips on the specimen has the same shape of the indenter geometry. Therefore, the shape of the entire unloading curve and the recovered displacement is associated with the elastic modulus of the specimen and the size and geometry of the resulting deformation on the specimen.

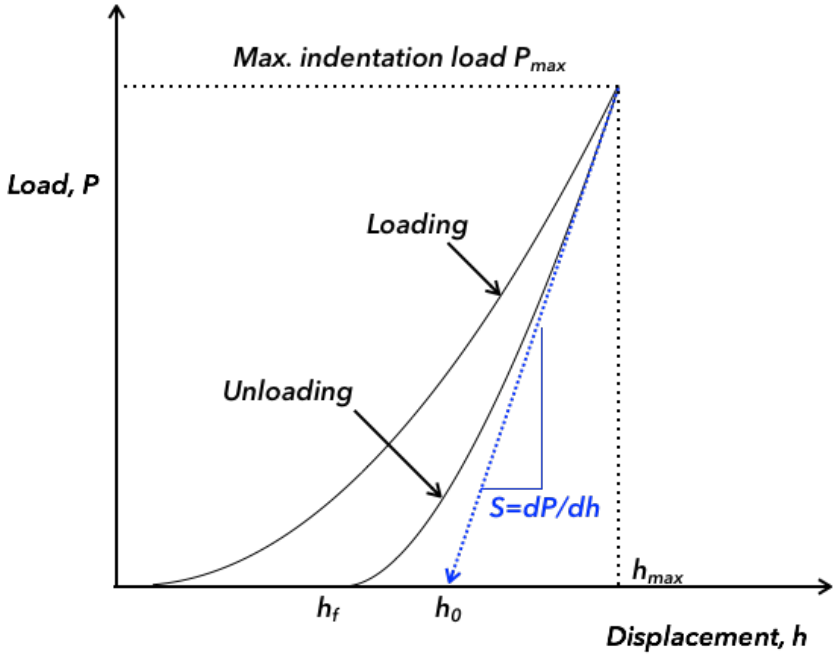

Figure 3.3 Typical indentation load-displacement data showing experimental quantities.

Fig. 3.4 illustrates the geometrical changes that occur during nanoindentation process and indicates the parameters for characterizing the contact geometry. As the indenter is driven into the thin film, the thin film experiences both elastic and plastic deformation. The plastic deformation leads to the formation of the permanent deformation that follows the shape of the indenter. To estimate the contact area at the peak load in the nanoindentation process, the contact depth, h_c, needs to be evaluated. Doerner and Nix used the flat punch approximation in which the contact area remains constant as the indenter is retreated and, thus, the contact depth can be estimated by extrapolating the initial linear part of the unloading curve [11]. As shown in the **Fig. 3.4**, to determine the contact depth from the experimental data, it is written as:

$$h_c = h - h_s \tag{3-1}$$

where 'h' is the total displacement, measured experimentally, and 'h_s' is the sink-in depth of the surface at the perimeter of the contact. The key factor to obtain is the sink-in depth at the contact perimeter from the load-displacement data. From the Sneddon's expression for a conical indenter [12], the area of the contact can be written as

$$h_s = \frac{(\pi - 2)}{\pi}(h - h_f) \tag{3-2}$$

Where the 'h_f' is the final depth, representing the amount of the permanent plastic deformation. Since the Sneddon's equation can only be applied to the elastic deformation of the components, the quantity *'$(h\text{-}h_f)$'* is used instead of 'h' in the **Eq. (3-2)**.

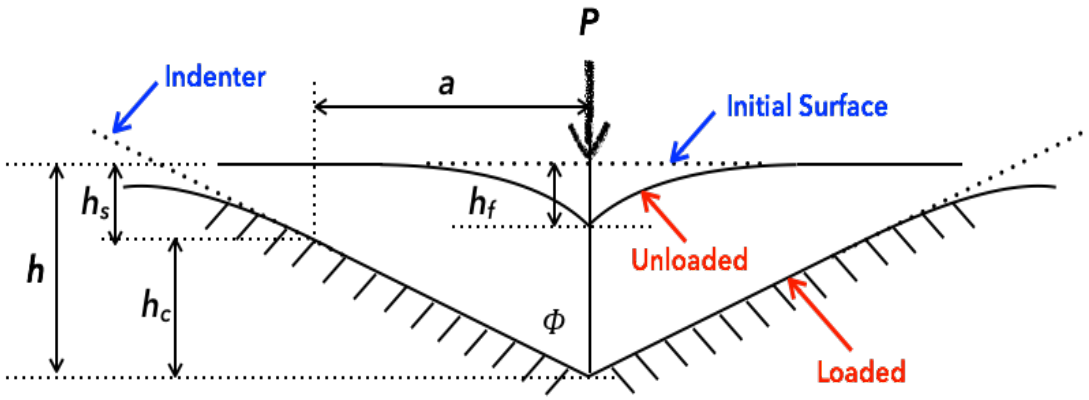

Figure 3.4 Schematic of the unloading process and parameters for the contact geometry.

From the Sneddon's expression, the force-displacement relationship for the conical indenter tip can be described as

$$(h - h_f) = 2\frac{P}{S} \tag{3-3}$$

substituting **Eq. (3-3)** into the **Eq. (3-2),** the amount of the sink-in, h_s, can be obtained as

$$h_s = \epsilon\frac{P_{max}}{S} \tag{3-4}$$

where 'ϵ' is a factor that represents the geometry of the indenter. 'ϵ' for a conical indenter is given by:

$$\epsilon = \frac{2(\pi - 2)}{\pi} \tag{3-5}$$

or 'ϵ=0.72'. For the paraboloid of revolution, 'ϵ' is 0.75 and for the flat punch, 'ϵ=0.72' [13]. Therefore, the relationship between the contact depth at peak loading is:

$$h_c = h - \epsilon\frac{P_{max}}{S} \tag{3-6}$$

The contact area can be determined by evaluating the area function at depth h_c. The area function, also called indenter shape function, describes the cross-sectional area of the indenter at a distance, *d,* from the apex of the tip as defined by:

$$A = F(h_c) \tag{3-7}$$

Once the contact area is determined, the hardness is evaluated from

$$H = \frac{P_{max}}{A} \tag{3-8}$$

Note that this definition of hardness assumes that elastic recovery during unloading is negligible. The effective elastic modulus can be analyzed by using the relationship between the contact area and the measured unloading stiffness. For any axisymmetric indenter [14], the relation is

$$S = \frac{dP}{dh} = \frac{2}{\sqrt{\pi}} E_r \sqrt{A}, \tag{3-9}$$

Here, $S=dP/dh$ is the experimentally measured stiffness at the initial part of unloading curve; E_r is the reduced elastic modulus which takes into account the effect of the non-rigid indenters.

$$\frac{1}{E_r} = \frac{(1-\nu^2)}{E} + \frac{(1-\nu_i^2)}{E_i} \tag{3-10}$$

where E_i (1140 GPa) and ν_i (0.07) are the elastic modulus and Poisson's ratio for the indenter tip, respectively; E and ν are the same quantity for the thin film.

In the flat punch approximation proposed by Doerner and Nix, the contact area remains as a constant as the indenter tip is withdrawn and the unloading curve is linear. However, in a real load-displacement curve, the unloading curves are evidently curved in a way that the flat punch approximation cannot account for. To consider this curved unloading trend, a power law relation is usually applied to the load-displacement relationship and can be conveniently written as:

$$P = \alpha(h - h_f)^m \tag{3-11}$$

where 'α' and 'm' are the power law fitting constants [14]. Values for the common indenter tip geometries are $m=1$ for flat cylinder, $m=1.5$ for paraboloids of revolution and $m=2$ for cones. **Table 3.1** shows the values of fitting constant observed by Oliver and Pharr. The wide range of variation of fitting constant, m, from 1.2 to 1.6 indicates that the flat punch approximation is not adequate and the indenter behaves like a paraboloid of revolution.

Material	***α (mN/nm^m)***	***m***	***Correlation coefficient, R***
Aluminum	0.265	1.38	0.999938
Soda-lime glass	0.0279	1.37	0.999997
Sapphire	0.0435	1.47	0.999998
Fused silica	0.0500	1.25	0.999997
Tungsten	0.141	1.51	0.999986
Silica	0.0215	1.43	0.999985

Table 3.1 Values for power law fitting constants characterizing unloading curves as observed in nanoindentation experiments with a Berkovich indenter. Table taken from [12]

3.2.2. Mechanical properties of solution process ATO thin films

Nanoindentation test using Berkovich diamond tip (Hystron Triboindenter) has been performed to investigate the mechanical properties (elastic modulus, hardness) of solution processed ATO thin films. Generally, the most influential factor affecting the mechanical property of solution processed thin films is the annealing temperature. To verify the effect of annealing temperature on mechanical properties of ATO thin films, three ATO samples annealed at different temperatures (400ºC, 500ºC, and 600ºC) are prepared. As described in the previous chapter for the ATO thin films, 10 wt% Sb-doping concentration in the coating solution with the multiple spin-coating method is used for a final thickness of 250 nm and the thin films are annealed in the furnace with oxygen-rich environment. **Fig. 3.5** shows the prepared ATO samples and nanoindentation apparatus.

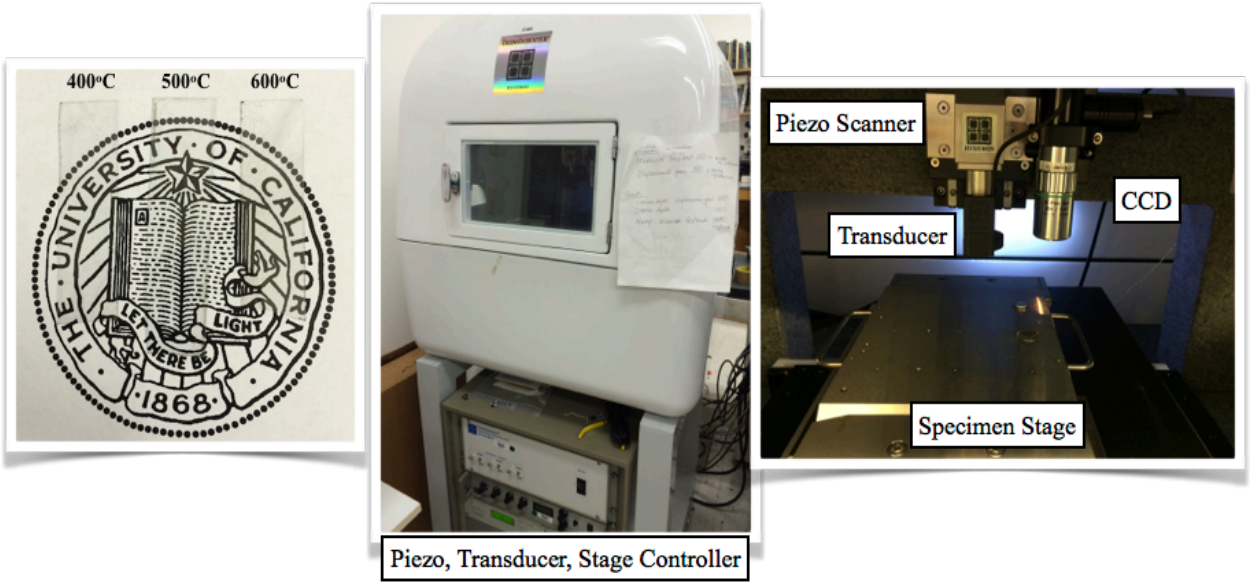

Figure 3.5 (A) 200 nm thick, 10 wt% Sb-doped ATO samples annealed at different temperatures with oxygen-rich environment (B) Hystron nanoindentation machine and controller set up (C) Nanoindenter components.

The load-penetration depth curves for ATO samples annealed at different temperatures are shown in **Fig. 3.6 (A)**. The maximum indentation load is set as 1000 μN and the maximum penetration depth of the ATO samples was 138 nm. From the load-penetration curves, the reduced elastic moduli were extracted by the initial linear portion of the unloading curves and elastic moduli were evaluated from **Eq. (3-10)**. For the elastic modulus (E_i) and Poisson's ratio

(ν_i) of the diamond Berkovich indenter tip, 1140 GPa and 0.07 were used, respectively, and $\nu = 0.25$, representing the Poisson's ratio for ATO thin films was applied [15]. The nanoindentation test results indicate that the elastic modulus increases from 30.95 GPa to 45.77 GPa as the annealing temperature increases. Hardness of the ATO samples were also obtained by using **Eq. (3-8)** and **Fig. 3.7** shows the variations of the hardness from 3.43 GPa to 4.94 GPa and the elastic moduli as the annealing temperature increases. Both the elastic moduli and hardnesses of the samples evaluated in this work exhibit much smaller values than those of vacuum-processed TCO films [14]. For the commercial TCO thin films (ITO, IZO) deposited by RF magnetron sputtering using argon gas, the average elastic modulus and hardness are around 100 GPa~140 GPa and 6.5 GPa ~10 GPa, respectively [15].

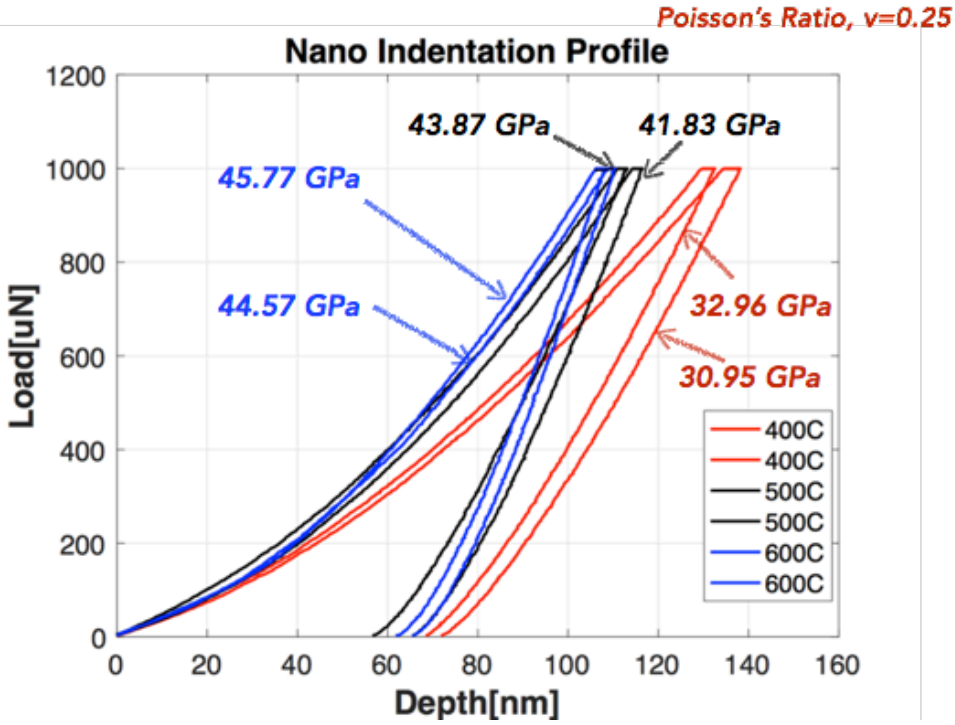

Figure 3.6 Load-penetration depth curves for ATO samples annealed at various temperatures.

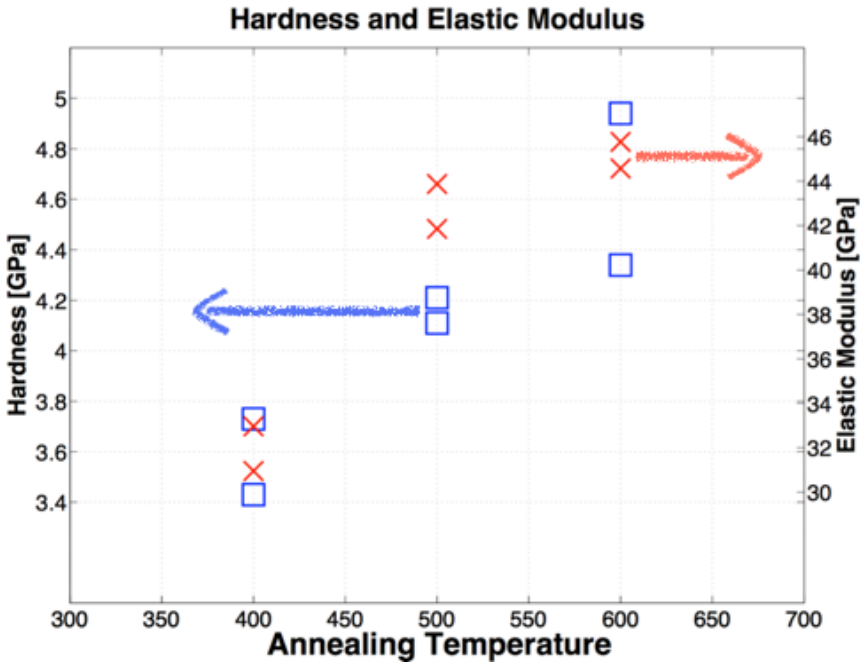

Figure 3.7 Hardness and elastic modulus of ATO samples annealed at various temperatures.

Table 3.2 lists the extracted mechanical properties (the reduced elastic modulus, hardness and other critical quantities for calculating the mechanical properties of the ATO thin films. It is found that the penetration depth of ATO thin films at the maximum indentation load (1000 μN) range from 113.1 nm to 138.2 nm and decreases as the annealing temperature increases. The contact area, A, and contact depth, h_c, also decrease as the annealing temperature increases. Power law constants for calculating the modified load for nanoindentation are also listed in Table 2 and the average, m, is around 1.29.

Loading μN	*E_r (GPa)*	*H (GPa)*	*h_{max} (nm)*	*A, h_c (nm^2, nm)*	*Power law coefficients (α, h_f, m)*
1000	46.83	4.34	116.6	2.297E5, 86.9	7.412, 66.96, 1.257
1000	45.65	4.94	113.1	2.015E5, 80.4	5.873, 57.616, 1.280
1000	44.96	4.21	115.7	2.245E5, 82.3	5.972, 62.36, 1.277
1000	42.95	4.11	121.6	2.424E5, 89.7	5.28, 66.31, 1.31
1000	32.09	3.43	138.2	2.904E5, 99.6	3.68, 70.088, 1.329
1000	34.11	3.73	132.6	2.669E5, 94.8	4.62, 67.846, 1.289

Table 3.2 Measured mechanical properties, geometry factors and power law coefficients.

3.3. Mechanical stress analysis of solution processed ATO thin films

3.3.1. Force controlled stress and strain controlled stress

The mechanical stress in thin films is known to be the main cause for reliability problems in microelectronic devices. Mechanical stress can especially affect not only the life time but also the performance for optoelectronic devices by changing the properties of birefringence. With the advancements of the optoelectronic devices such as flat panel displays, solar cells and electrochromic smart windows, attention must be paid to the mechanical flexibility and stress of thin films

For the thin films such as TCOs, there are two different types of mechanical stress. The first one is the intrinsic stress which comes from the defects such as dislocations in the film. On the other hand, the extrinsic stress of a thin film mainly comes from the adhesion to its substrate. A thin film and its substrate usually have different coefficients of thermal expansion (CTE), such that the temperature changes during deposition processes or thermal annealing processes can produce the mechanical stress due to CTE mismatch. When the force or displacement is exerted on the thin film on top of a substrate, its major deformation is determined by the much thicker substrate. Thus, the mechanical stress of the thin films is mainly the displacement controlled stress as shown in **Fig. 3.8**.

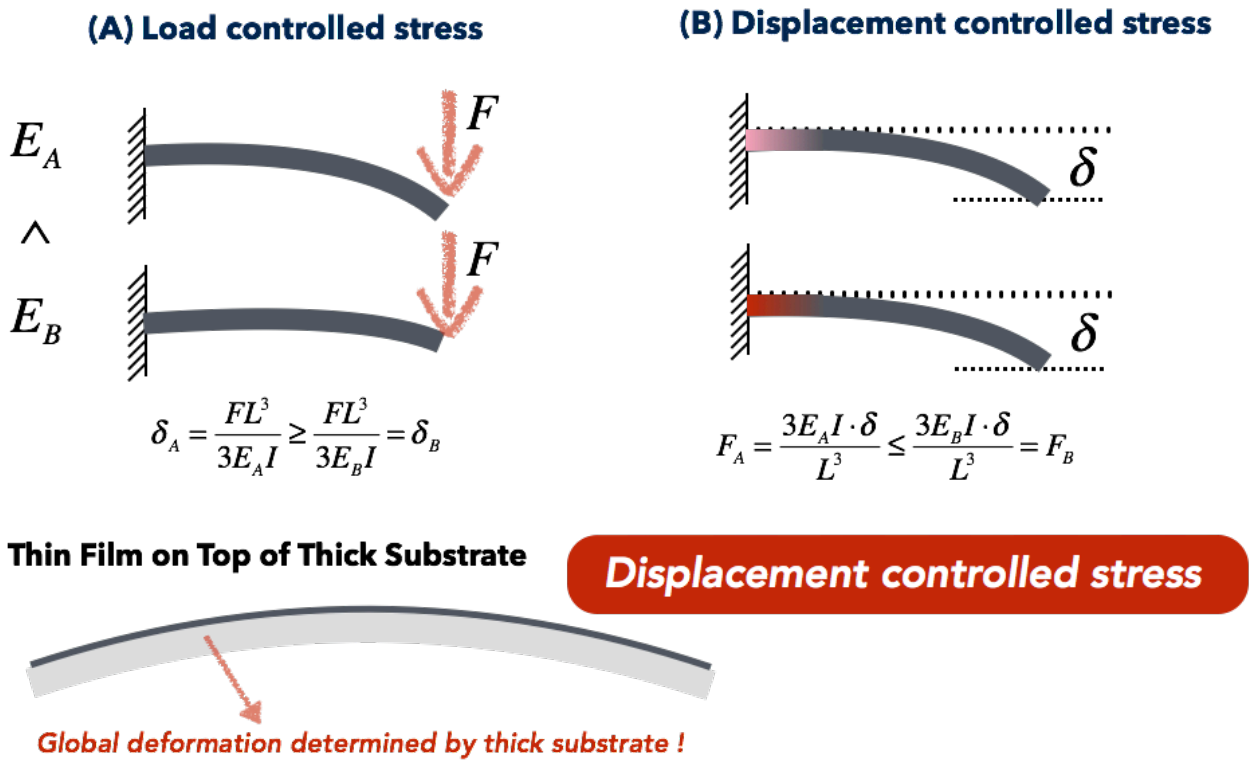

Figure 3.8 Schematic of mechanical behavior of thin films under various loading conditions.

In the previous section, we measured the elastic modulus and the hardness of solution processed ATO thin films using nanoindentation and it is found that elastic modulus of the solution processed ATO thin films is about 4X smaller than that of vacuum processed TCO thin films (ITO, IZO). The influence of the low elastic modulus of the material can be interpreted under two different load condition. When the same amount of force is applied to two materials with different elastic modulus (E_A<E_B) as shown in **Fig. 3.8 (A)**, the amount of deflection for the material with lower elasticity (A) is larger than that of the stiffer material (B). This difference in deflection is attributed to the elastic modulus since the amount of deflection is inversely proportional to the elastic modulus of the material. On the other hand, when the deformation of the materials is controlled by the displacement as shown in **Fig. 3.8 (B),** the mechanical stress will be higher in the material with higher elastic modulus since the applied force is linearly proportional to the elastic modulus of the material. Therefore, the elastic modulus plays a pivotal role in understanding of the mechanical flexibility and the stress responses under the various load conditions.

3.3.2. Standard test methods for the flexural properties of the material

There are two different types of bending test according the American Standard Test Method (ASTM D6272, ASTM D790): three-point bending and four-point bending test. The main differences between these two test methods are the position of the maximum stresses and the bending moment. For the four-point bending test, a pure maximum bending moment exists and produces a uniformly distributed maximum stress in the considered length of the beam. However, for the three-point bending test, the maximum stress occurs at the point where the load is located and decreases elsewhere. For this reason, the four-point bending test is more suitable for investigating mechanical properties or verifying numerical models, while the three-point bending test is appropriate for testing the stress of a specific area on the specimen [16]. The conventional four-point bending test is shown in **Fig. 3.9 (A).** The test sample rests on two fixed supports and the force is applied at two points. The two mechanical loads at the center portion of the beam are typically driven by a motor with a constant velocity. The distance between the two loads, called load span, is one half of the overall support span. **Fig. 3.9 (B)** shows the shear diagram in which the shear force is a constant for the segment between the first fixed support and the first central load. Shear force in this segment is equal to the force applied by the first central load because the beam does not resist shearing. On the other hand, the bending moment is directly proportional to the distance from the support such that it varies linearly as shown in **Fig. 3.9 (C)**. Similar reasoning applies to the opposite site. At any arbitrary point between two central loads, no shear force is required to maintain the equilibrium of a segment in this zone and only a constant bending moment exists in this segment. This pure constant bending moment allows for robust analyses of the stress responses of the material.

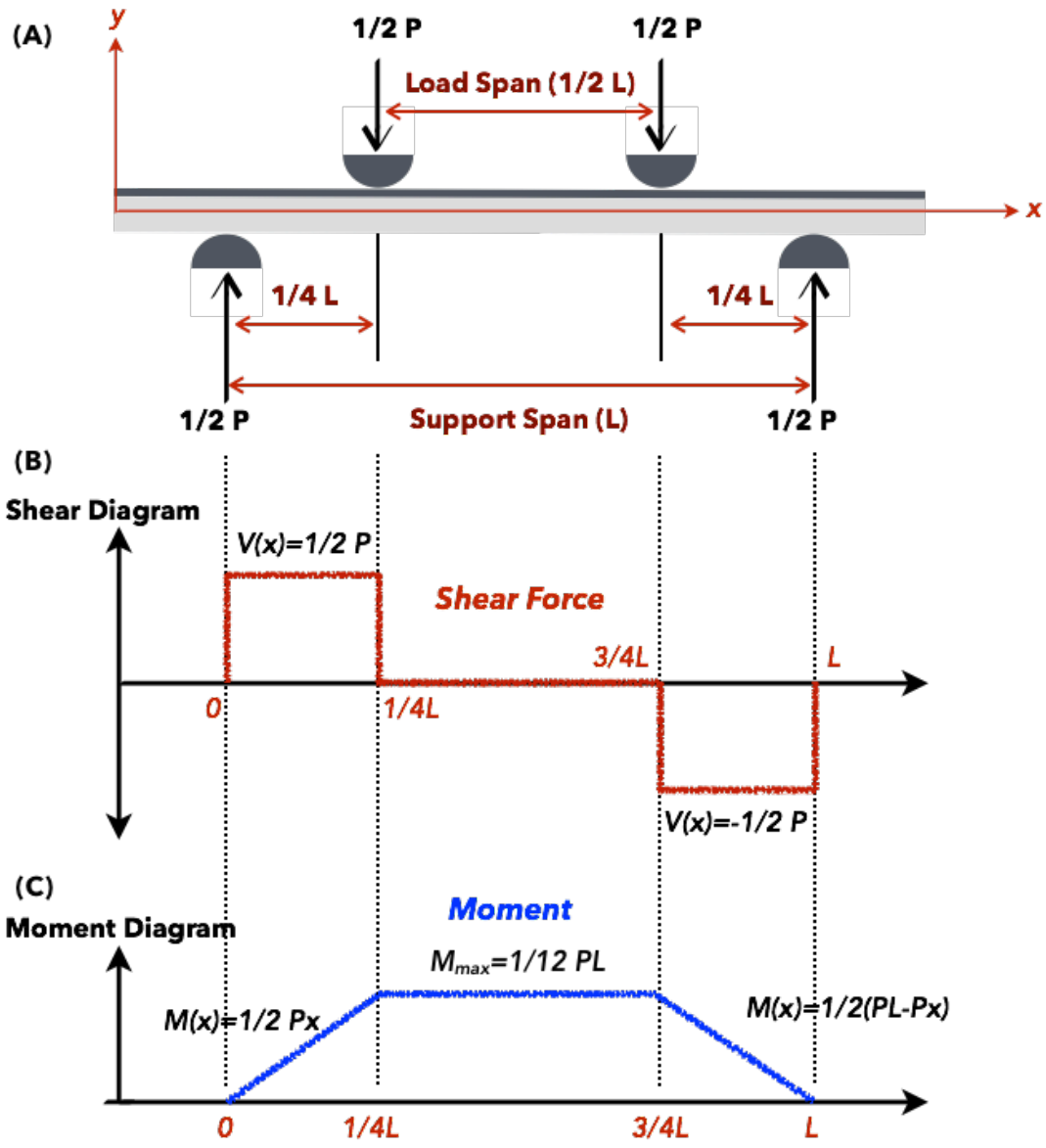

Figure 3.9 Schematic of four-point bending test for the beam loaded with the forces.

3.3.3. Finite Element Analysis

The mechanical flexibility of solution processed ATO thin films is analyzed by the finite element analysis (FEA) using a four-point bending test under both strain-controlled and force-controlled conditions. The elements were modeled using linear elastic material and shells with 100 μm in thickness. For the shell element, the Belytschko-Lin-Tsay type was applied to reduce the mathematical operations [17]. All components were composed of quadrilaterals with good mesh qualities. For the boundary conditions, two moving loads and two fixed supports are modeled using rigid body material and force/displacement load condition are applied in the normal direction on the surface of the moving loads. The more precise contact behavior between the loads and the thin films is analyzed using a penalty method to this model. In this penalty method, normal interface springs are implemented between all penetrating nodes and the contact surface, such that the sliding and impact along the interfaces can be implemented with low computational expense [18]. **Fig. 3.10** shows the generated finite element (FE) model, boundary conditions and basic model information.

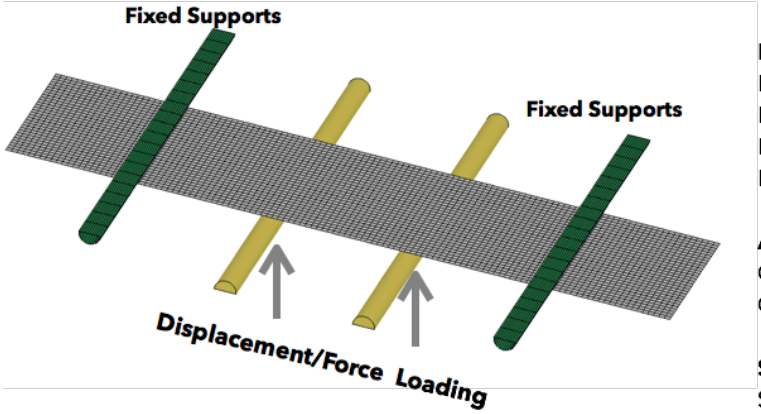

FE Model
Plate-Shell (Quad 2000)
Support and Moving Jig - Shell (Quad 2000)

Mesh Quality
Max. Warpage-0.0366
Max. Aspect Ratio - 5.0
Max. Skew - 0.04
Min. Jacobian -1.0

Analysis
Quasi-Static Explicit Code
Calculation Time 1.0 Sec.

Shell Properties
Shell Thickness 0.01mm (10um)
Element Formulation: Belytschoko Tsay
Shear Correction Factor: 0.8333

Figure 3.10 FE model of four-point bending test and boundary conditions.

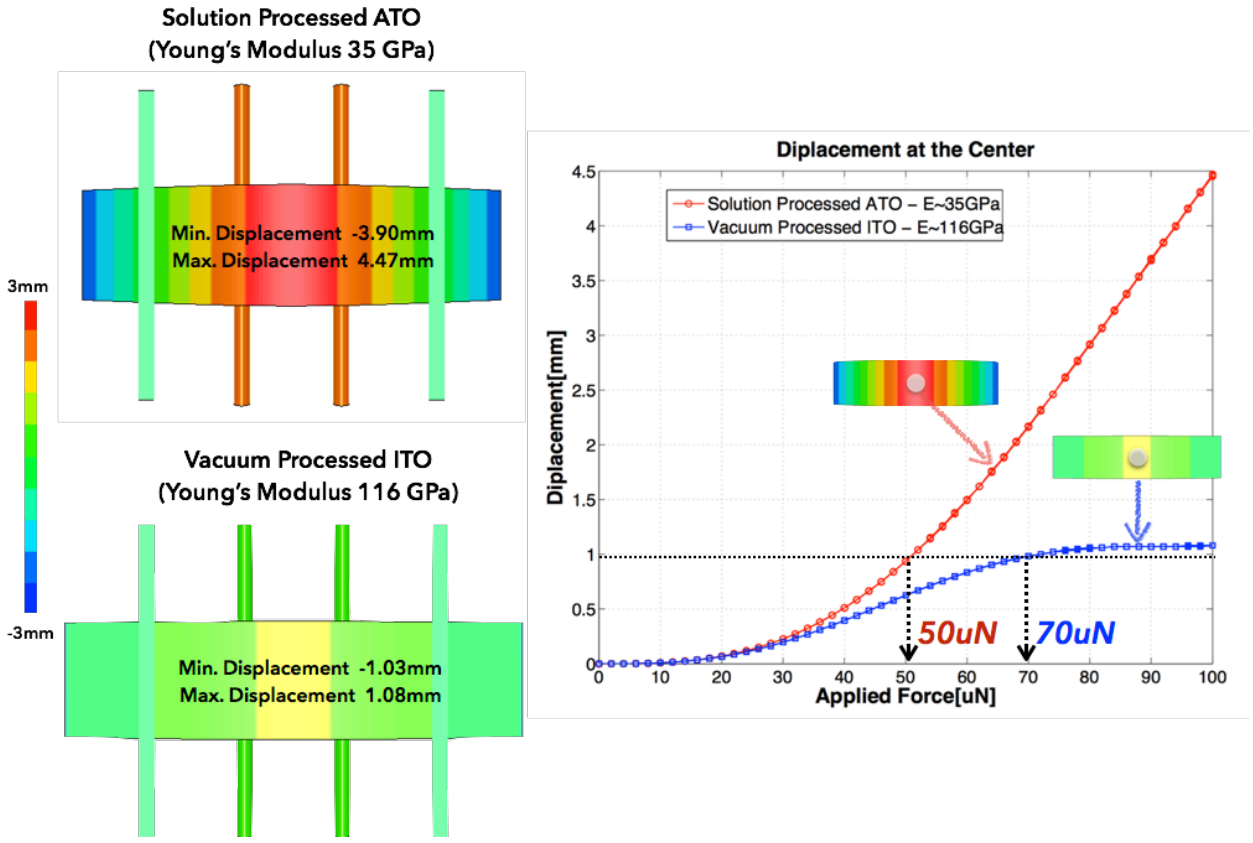

Figure 3.11 Comparative 3D finite element analysis (FEA) showing the deflection of the thin films under the force controlled four-point bending test.

Fig. 3.11 illustrates the 3D-FEA results that compares the deformation of two different TCO thin films under the force-controlled four-point bending test. This analysis indicates that the solution-processed ATO thin films (E=35 GPa) has a larger deformation than that of vacuum-processed TCO films (E=116 GPa) under the same amount of applied force. Consequently, **Fig. 3.11** indicates the maximum deformation of 4.47 mm for the solution-processed TCO and 1.08 mm for the vacuum-processed TCO under the same load condition of 100 μN (maximum deformation is observed at the center). When the applied load is small, the deflection at the center point increases quadratically for both cases. When the applied load is beyond 60 μN, the incremental deflection for the vacuum-processed thin films becomes smaller and reaches a plateau due to its stiffness while the deflection for the solution processed thin films increases linearly to 4.5 mm. Under the load of 100 μN, about 4x larger deflection is observed for the ATO sample than that of the vacuum-processed film.

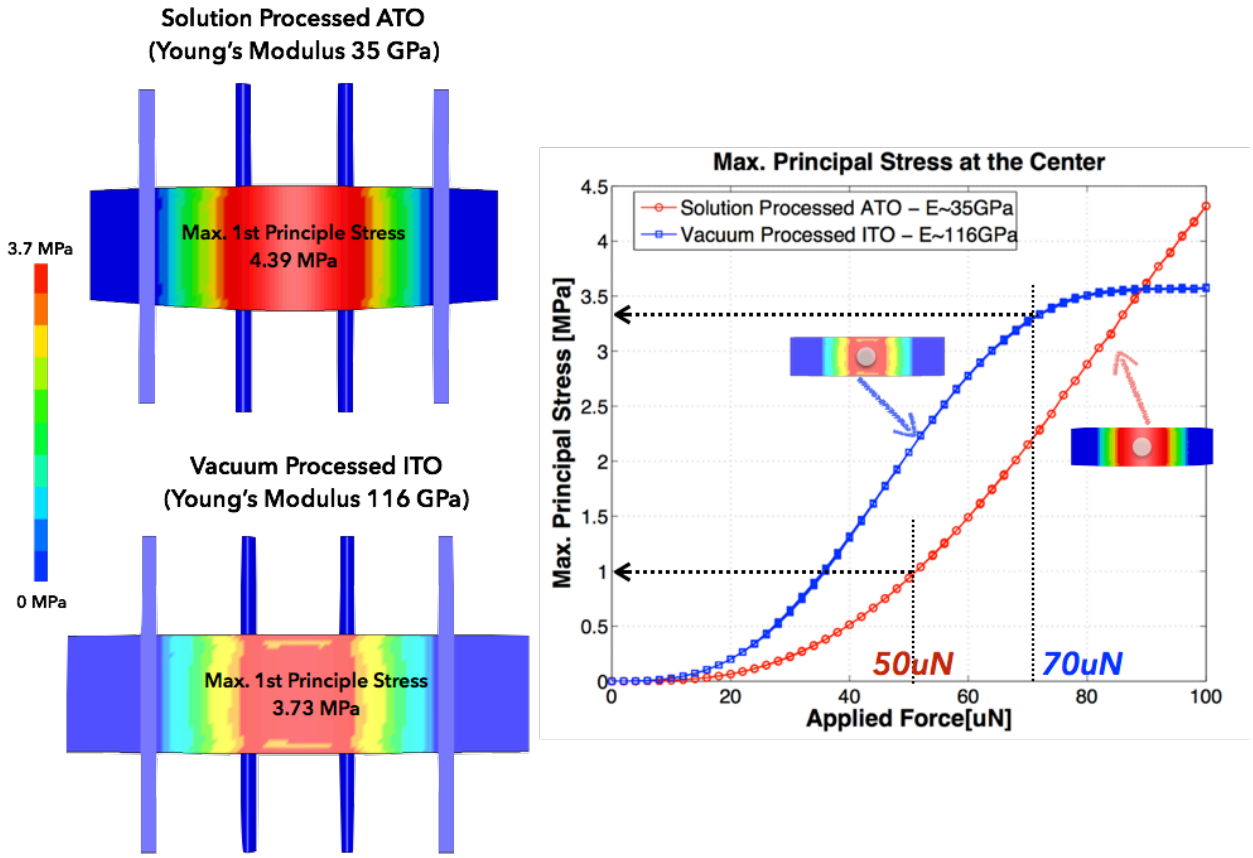

Figure 3.12 Comparative 3D finite element analysis (FEA) showing the maximum principle stress of the thin films under the force controlled four-point bending test.

For brittle materials such as TCO films, the maximum stress/strain criterion is generally used to estimate their mechanical failure. Under this criterion, a material failure occurs when the maximum principal stress (σ_1) in a material exceeds the ultimate tensile strength of the material. Thus, the comparison of the maximum principle stress distribution is the standard stress criterion for brittle materials [19]. **Fig. 3.12** illustrates that the stress level of the solution processed ATO films is found to be lower than that of the vacuum-processed films at the center until the applied force reaches 90 μN. The low maximum principal stress of the solution-processed TCO film is attributed to its high elastic modulus. To evaluate the maximum principal stress under the same amplitude of deflection, the applied force for each film at 1 mm displacements are extracted in **Fig. 3.11** and mapped on to the force-stress curve in **Fig. 3.12**. It is found that about 3.3x larger maximum principal stress is observed for the vacuum-processed thin film as compared to that of the solution-processed thin film. These results show improved mechanical flexibility and stable stress levels under the identical displacement for solution-processed ATO thin films as compared to those of vacuum-processed TCO films.

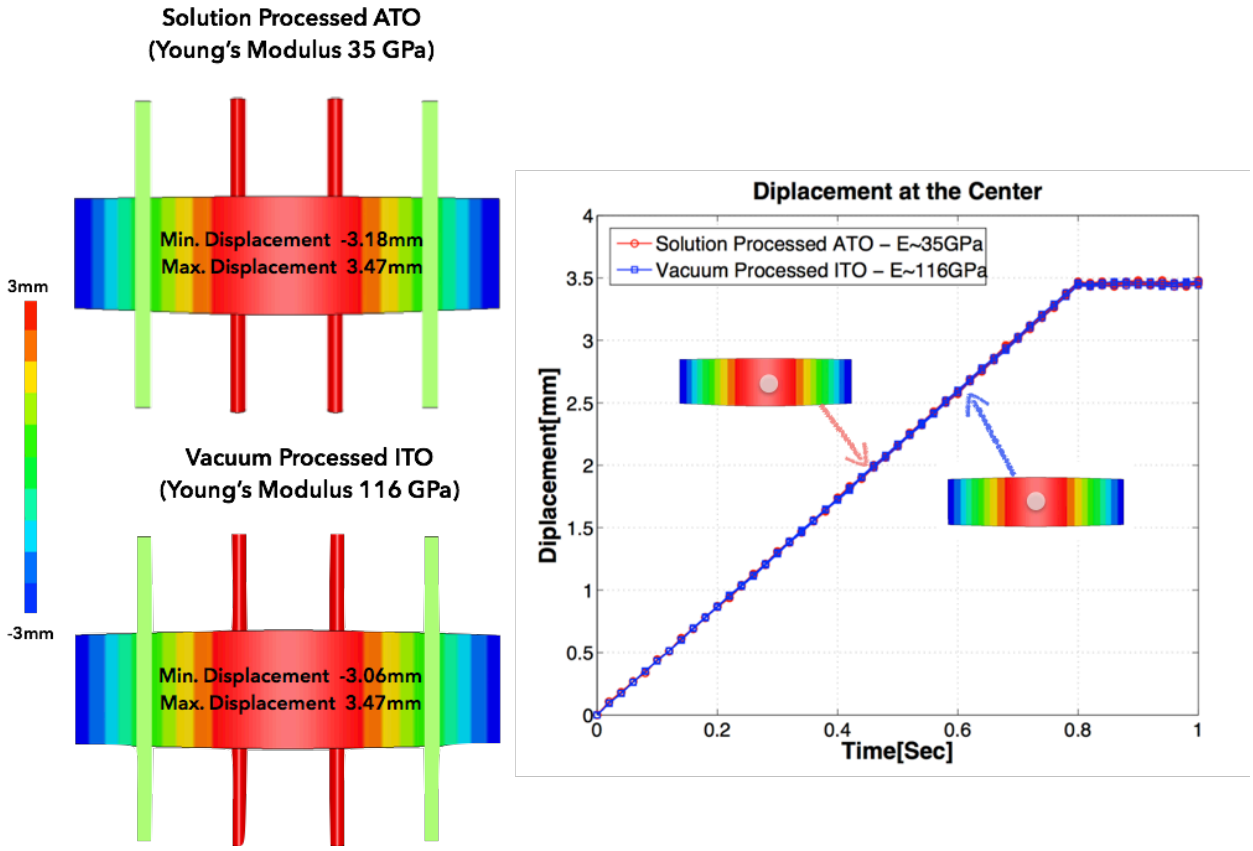

Figure 3.13 Comparative 3D finite element analysis (FEA) showing the deflections of the thin films under the force controlled four-point bending test.

Fig. 3.13 displays the 3D FEA results that present almost identical deflection of the two films under the displacement controlled four-point bending. This result is reasonable because the bending of the thin films is controlled by the same amount of displacement with two applied central loads. In the FE model, a 3 mm of displacement by the two central applied loads is applied for 0.9 sec while maintaining the position for 0.1 sec to minimize the dynamic effects of the FE model. The simulation result reveals that the dynamic effect of the thin films is negligible and the model is quasi-static. A maximum displacement of 3.47 mm was evaluated for both thin films under an applied displacement of 3 mm.

Fig. 3.14 clearly shows that the maximum principle stress of thin films varies linearly as the displacement loading increases and the peak stress directly depends on the elastic modulus. Unlike the maximum principle stress distribution under the force-controlled four-point bending simulation, no clear slope changes in the stress versus time plot are found in the FEA results. Specifically, a value of 3.59 MPa for the maximum principle stress is found for the solution processed ATO thin film (E=35 GPa) and 11.63 MPa is estimated for the vacuum based TCO thin film.

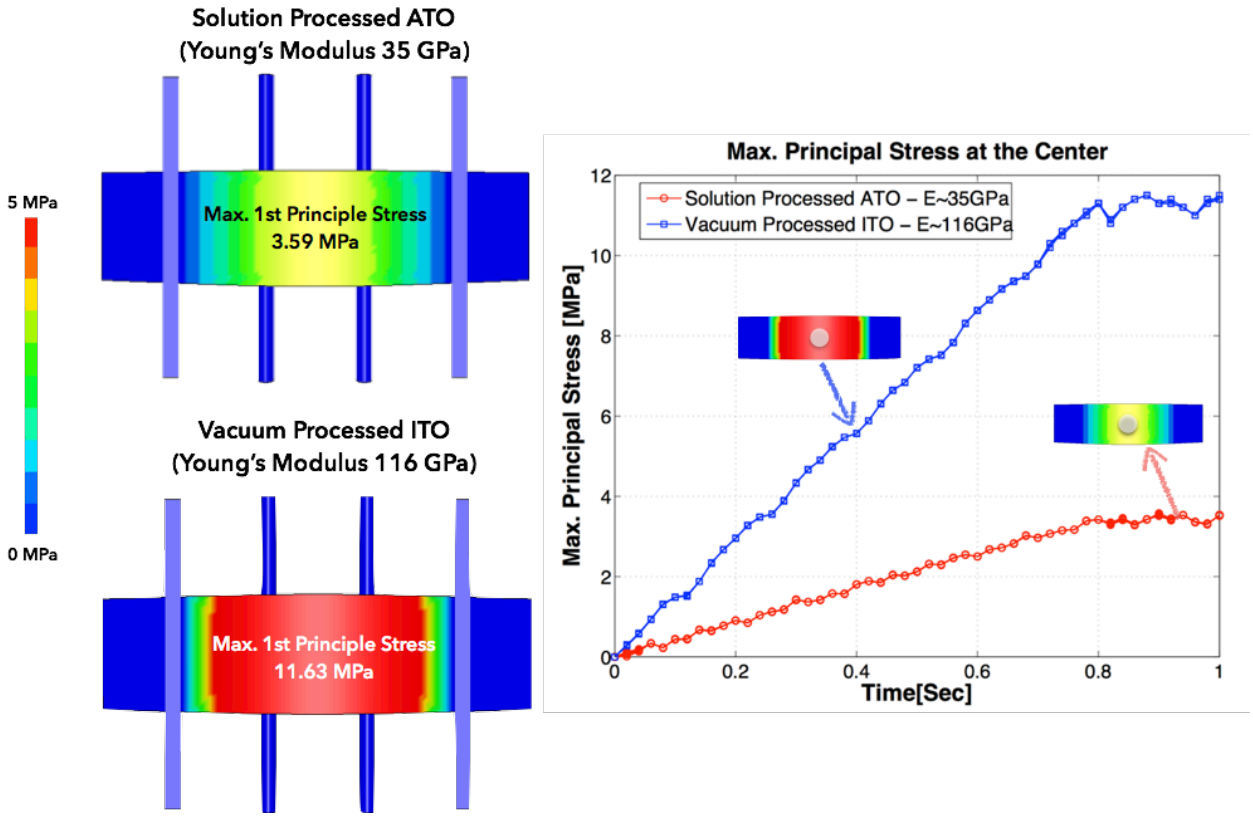

Figure 3.14 Comparative 3D finite element analysis (FEA) showing the maximum principle stress of the thin films under the displacement controlled four-point bending test.

3.4. Electrical performance changes of the solution processed ATO thin films under mechanical loading

3.4.1. ATO deposition on top of a flexible glass substrate

There has been a growing interest in the flexible optoelectronic devices using graphene [20]–[22] and metal nanowires [23]–[26] as the interconnection materials. However, these materials are limited by their uniformity and long-term stability issues. TCOs could be a viable alternative in flexible optoelectronic devices such as touch screens and interactive electronics. As we discussed in the previous sections, solution processed ATO thin films show improved flexibility and mechanical stress tolerance as compared with that of vacuum processed TCO thin films. They are, therefore, compelling candidates for bendable optoelectronic devices.

Measuring the electrical performance changes under the mechanical loading is important for the bendable optoelectronic devices. To investigate the electrical resistance variations under the displacement controlled four-point bending test, we use the 10 wt% ATO coating solution on top of a flexible glass substrate (Corning Willow Glass) with the multiple spin coating process.

Silver electrode patterns are printed using a nanoparticle-based silver ink (EMD 5730, Sunchemical) on top of an ATO thin film. Subsequently, silver nanoparticles are sintered 180ºC on a hotplate for 30 minutes. Inkjet printing is conducted by using a Fujifilm Dimatix materials printer (DMP-2831) with a Fujifilm Dimatix cartridge delivering a 10 pL droplet volume. **Fig. 3.15** shows the ATO thin film on top of the flexible glass with silver electrode patterns.

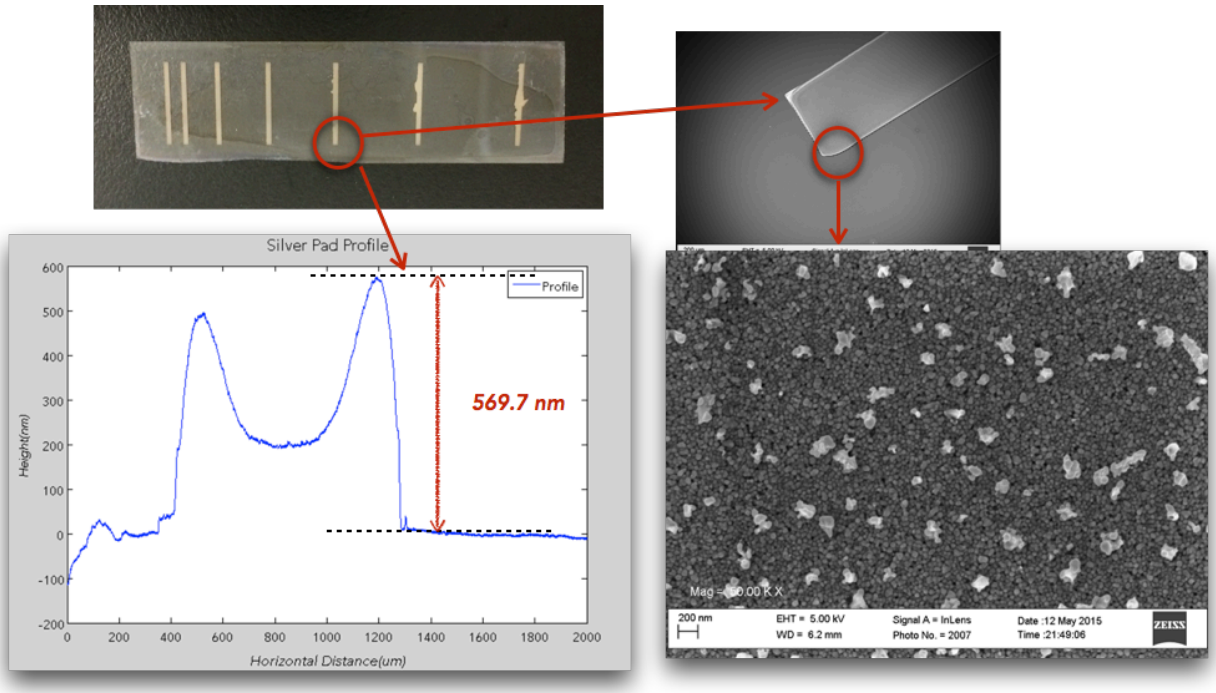

Figure 3.15 A 150 nm-thick ATO thin film on top of a flexible glass substrate and inkjet-printed silver electrode patterns on the ATO thin film.

Silver electrodes printed on the ATO thin film with 1 mm widths, 18 mm lengths with 0.5 Ω/sq. show 570 nm of pattern thickness, as obtained from the depth profiler. Nano particle sintering was investigated using SEM as shown in **Fig. 3.15**. After the first pair of silver electrodes are printed on the ATO thin film with a gap of 3 mm, more electrodes are printed with increased gap distance up to 18 mm. **Fig. 3.16** depicts that the prepared ATO sample for the four-point bending mechanical measurements with measured electrical resistance between the silver electrodes before applying the mechanical loads.

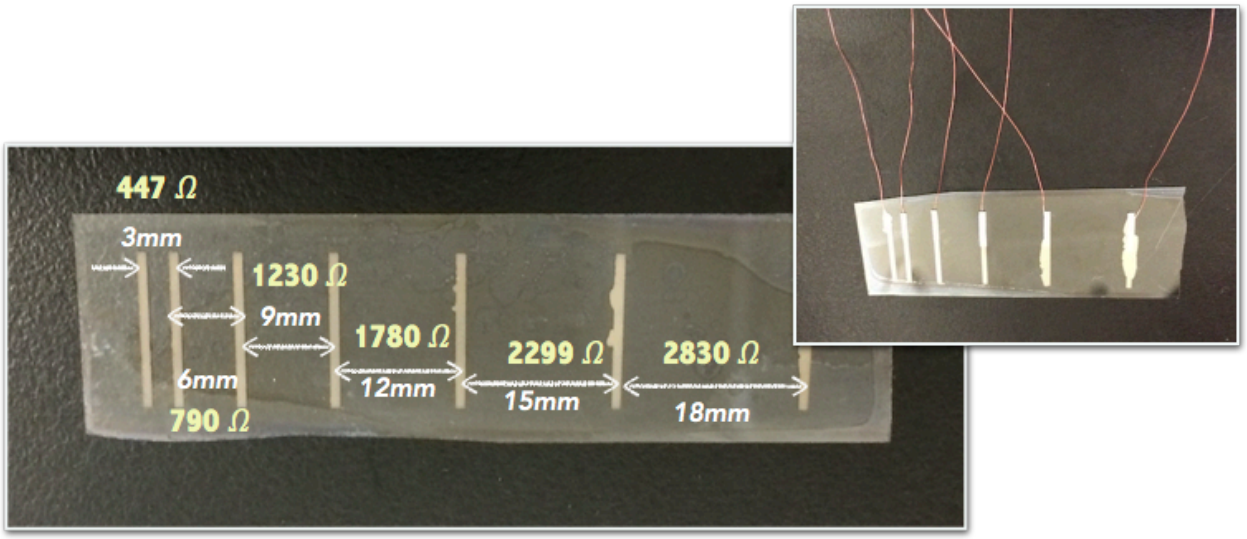

Figure 3.16 Silver electrodes are patterned on top of the ATO sample with increasing pattern spacing showing the electrical resistance between electrodes.

This transmission line method (or transfer line method, TLM) is widely used to evaluate the series resistance in the contact between the metal electrode and semiconductor [27], [28]. In the transistor, the contact resistance is one of the critical factors that can affect the performance of the transistor. Although contact resistance for metallic conductors is not an important factor, it could have a large value for the electrode patterns made by nanoparticles in this case. The contact resistance values of the inkjet-printed silver electrode patterns were extracted using the transmission line method. The resistance values were plotted as a function of distance between electrodes. When the spacing between electrodes is zero, the extrapolated resistance is equal to the contact resistance. **Fig. 3.16** presents the resistance between inkjet-printed silver electrode pads as a function of the electrode spacing. The resistance values were measured from 3 mm to 18 mm of electrode spacing and the extracted contact resistance was approximately 1.89 Ωcm^2. Thus, the contact resistance does not affect the resistance changes of the ATO thin film under the mechanical loading tests.

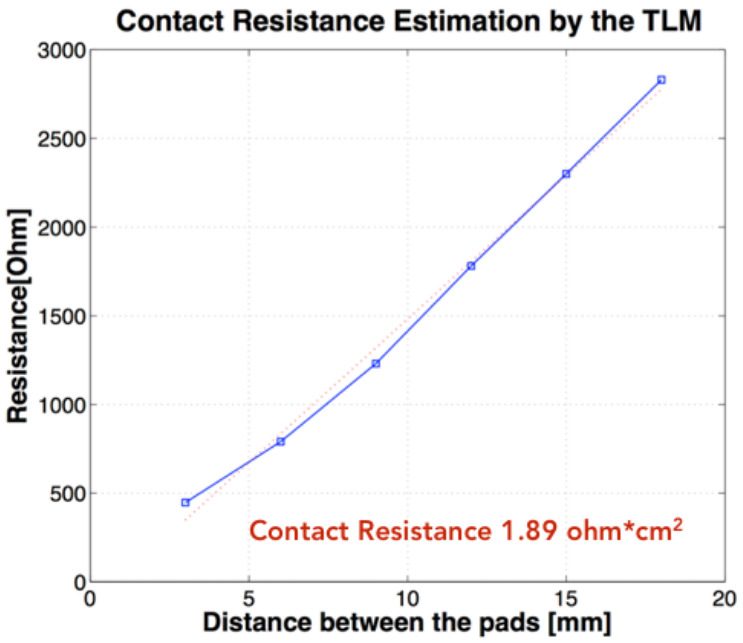

Figure 3.16 Evaluated contact resistance using the transmission line method.

3.4.2. Electrical resistance changes under the mechanical loading test

Fig. 3.17 depicts the experimental set-up mimicking a four-point bending test to measure the electrical resistance changes. A commercially available force transducer (OMEGA Eng., LC305-100lb) is used to measure the applied force. Silver electrodes patterned on the ATO thin film are mounted on top of the two glass loading rods on the lifting frame. In order to change the displacement loading, the lift frame is controlled by a rotating loading knob and the force is transmitted to the two glass loading rods placed on the groove of the loading frame to make a line contact between the loading rods and the ATO thin film. While the two glass loading rods are lifting the ATO thin film upward, a fixed frame is blocking the outer part of the ATO thin film to make the four-point bending load condition. **Fig. 3.17** clearly shows the ATO thin film on the flexible glass substrate is bendable under the mechanical loading. The force transducer was placed between the lifting frame and the loading knob and the applied force was evaluated by the force transducer. In order to record the electrical resistance changes, two probe tips were placed on the silver electrode patterns to measure the resistance.

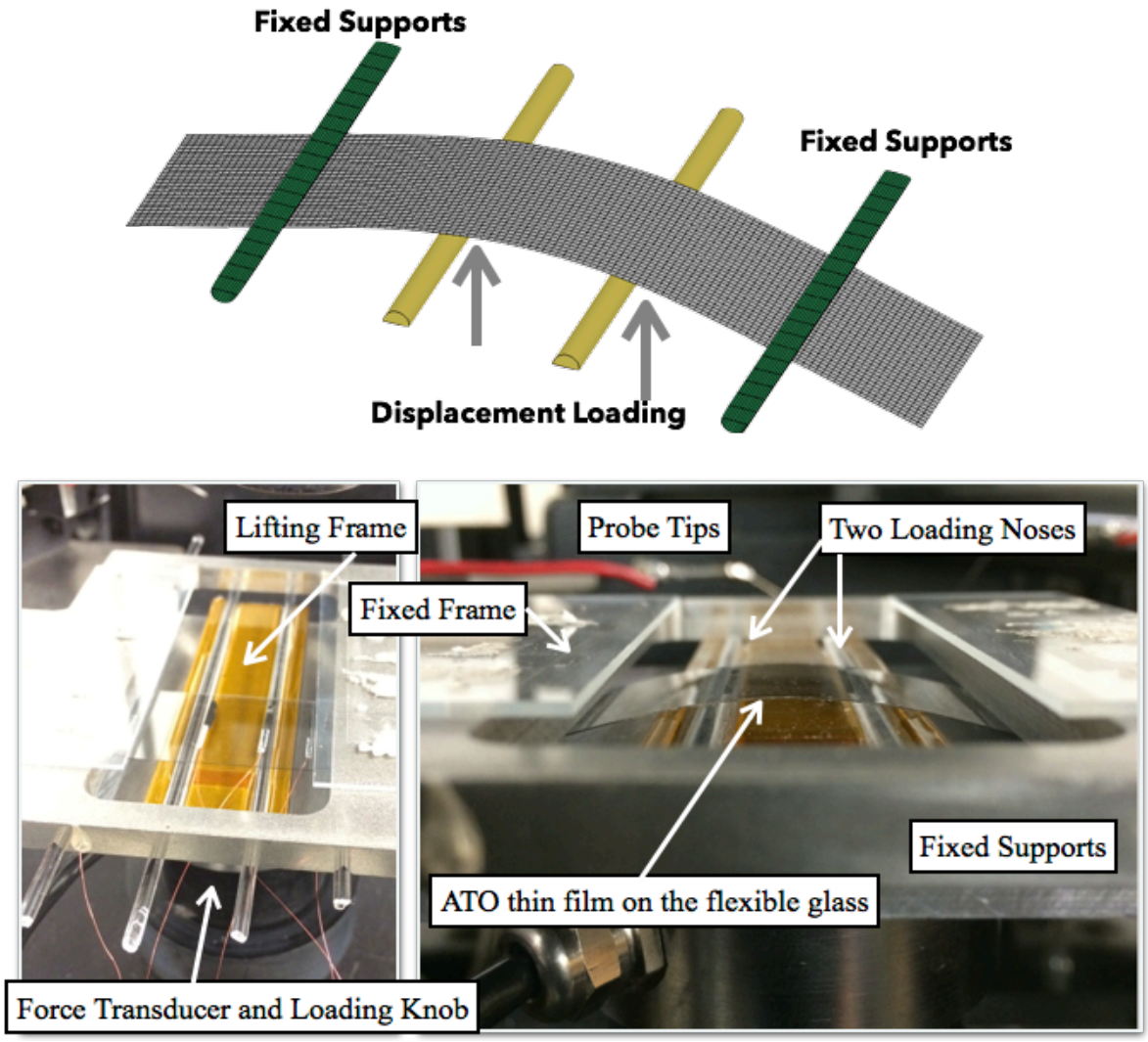

Figure 3.17 Schematic view and the experimental test set-up for the electrical resistance measurements under the applied loads.

Fig. 3.18 shows the measured electrical resistance changes under the applied loads. For the sample with electrodes with 15 mm in gap distance, the initial electrical resistance is 2.3 kΩ and the variation in resistance is less than 8% as the applied force increases to 6 N. In the ATO sample of electrodes with 12 mm in gap distance, the initial resistance is 1.76 kΩ and the resistance varies within 3% of resistance deviation when the force increased to 6 N. **Fig. 3.18** confirms that the resistance of the ATO thin film does not vary too much under the 6 N load or 30cm in radius of curvature in our setup for the bendable optoelectronic devices.

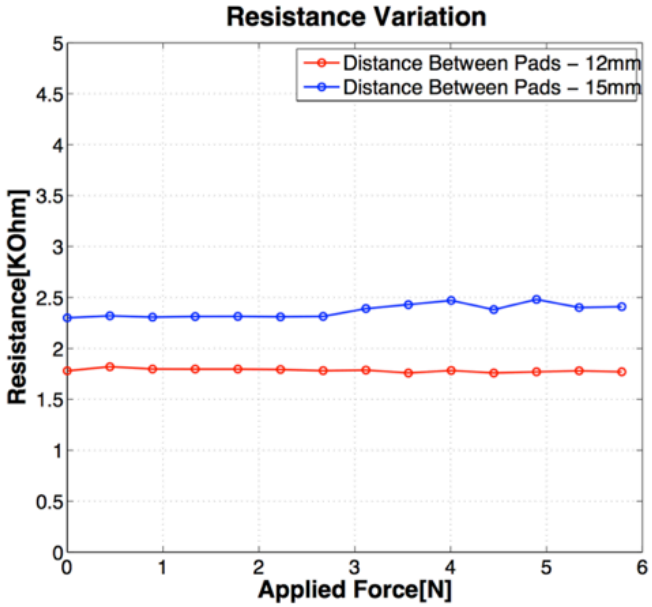

Figure 3.18 Resistance variation of the ATO thin film under the mechanical loading.

3.5. Summary

In summary, we successfully investigate the elastic modulus of the solution processed ATO films from the nano-indentation tests to be around 35 GPa, which is about one third of the elastic modulus of the commercial vacuum-processed ITO thin films. The 3D finite element analysis is developed for the mechanical four-point bending tests and the results show that about 4x larger deflection and 3.3x smaller maximum principal stress can be achieved for the solution-processed ATO samples as compared with those of the commercial vacuum-processed ITO samples. As such, the solution-processed ATO thin films could have the potential to be used in transparent, conductive electronic components with improved mechanical flexibility and stress for optoelectronic devices.

3.6. References

[1] W. Oliver, "Progress in the development of a mechanical properties microprobe," *MRS Bull.*, no. October, pp. 4–10, 1986.

[2] W. D. Nix, "Mechanical properties of thin films," *Metall. Trans. A*, vol. 20, no. 11, pp. 2217–2245, 1989.

[3] W. C. Oliver and C. J. McHargue, "Characterizing the hardness and modulus of thin films using a mechanical properties microprobe," *Thin Solid Films*, vol. 161, no. C, pp. 117–122, 1988.

[4] P. J. Burnett and D. S. Rickerby, "The mechanical properties of wear-resistant coatings. I: Modelling of hardness behaviour," *Thin Solid Films*, vol. 148, no. 1, pp. 41–50, 1987.

[5] L. Wu, X. Guo, and J. Zhang, "Abrasive Resistant Coatings—A Review," *Lubricants*, vol. 2, no. 2, pp. 66–89, 2014.

[6] G. M. Pharr and W. C. Oliver, “Measurement of Thin Film Mechanical Properties Using Nanoindentation,” *MRS Bull.*, vol. 17, no. 7, pp. 28–33, 1992.
[7] N. A. Sakharova, J. V. Fernandes, J. M. Antunes, and M. C. Oliveira, “Comparison between Berkovich, Vickers and conical indentation tests: A three-dimensional numerical simulation study,” *Int. J. Solids Struct.*, vol. 46, no. 5, pp. 1095–1104, 2009.
[8] L. Min, C. Wei-min, L. Nai-gang, and W. Ling-Dong, “A numerical study of indentation using indenters of different geometry,” *J. Mater. Res.*, vol. 19, no. 1, pp. 73–78, 2004.
[9] D. Tabor, “A simple theory of static and dynamic hardness,” in *Royal Society A*, 1948.
[10] N. A. Stilwell and D. Tabor, “Elastic Recovery of Conical Indentations,” *Proc. Phys. Soc.*, vol. 78, no. 2, pp. 169–179, 1961.
[11] M. F. Doerner and W. D. Nix, “A method for interpreting the data from depth-sensing indentation instruments,” *J. Mater. Res.*, 1986.
[12] I. N. Sneddon, “The relation between load and penetration in the axisymmetric boussinesq problem for a punch of arbitrary profile,” *Int. J. Eng. Sci.*, vol. 3, no. 1, pp. 47–57, 1965.
[13] K. Zeng, F. Zhu, J. Hu, L. Shen, K. Zhang, and H. Gong, “Investigation of mechanical properties of transparent conducting oxide thin films,” *Thin Solid Films*, vol. 443, no. 1–2, pp. 60–65, 2003.
[14] M. S. Pradeepkumar, K. P. Sibin, N. Swain, N. Sridhara, A. Dey, H. C. Barshilia, and A. K. Sharma, “Nanoindentation response of ITO film,” *Ceram. Int.*, vol. 41, no. 6, pp. 8223–8229, 2015.
[15] C. Oliver and M. Pharr, “An improved technique for determining hardness and elastic modulus using load and displacement sensing indentation experiments,” *Journal of Materials Research*, vol. 7, no. 11. pp. 1564–1583, 1992.
[16] R. D. Heap and R. H. Norman, *Flexural Testing of Plastics*. The Plastic Institute, 1969.
[17] T. Belytschko, J. I. Lin, and T. Chen-Shyh, “Explicit algorithms for the nonlinear dynamics of shells,” *Comput. Methods Appl. Mech. Eng.*, vol. 42, no. 2, pp. 225–251, 1984.
[18] J. O. Hallquist, G. L. Goudreau, and D. J. Benson, “Sliding interfaces with contact-impact in large-scale Lagrangian computations,” *Comput. Methods Appl. Mech. Eng.*, vol. 51, no. 1–3, pp. 107–137, 1985.
[19] R. T. Qu and Z. F. Zhang, “A universal fracture criterion for high-strength materials,” *Sci. Rep.*, vol. 3, p. 1117, 2013.
[20] F. Bonaccorso, Z. Sun, T. Hasan, and A. C. Ferrari, “Graphene Photonics and Optoelectronics,” *Nat. Photonics*, vol. 4, no. August, pp. 611–622, 2010.
[21] S. Bae, H. K. Kim, Y. Lee, X. Xu, J.-S. Park, Y. Zheng, J. Balakrishnan, D. Im, T. Lei, Y. Il Song, Y. J. Kim, K. S. Kim, B. Özyilmaz, J.-H. Ahn, B. H. Hong, and S. Iijima, “30 inch Roll-Based Production of High-Quality Graphene Films for Flexible Transparent Electrodes,” *Nat. Nanotechnol.*, vol. 5, no. August, pp. 1–5, 2009.
[22] K. S. Kim, Y. Zhao, H. Jang, S. Y. Lee, J. M. Kim, K. S. Kim, J.-H. Ahn, P. Kim, J.-Y. Choi, and B. H. Hong, “Large-scale pattern growth of graphene films for stretchable transparent electrodes,” *Nature*, vol. 457, no. 7230, pp. 706–710, 2009.
[23] S. De, T. M. Higgins, P. E. Lyons, E. M. Doherty, P. N. Nirmalraj, W. J. Blau, J. J. Boland, and J. N. Coleman, “Silver Nanowire Networks as Flexible ,” *ACS Nano*, vol. 3, no. 7, pp. 1767–1774, 2009.

[24] E. C. Garnett, W. Cai, J. J. Cha, F. Mahmood, S. T. Connor, M. Greyson Christoforo, Y. Cui, M. D. McGehee, and M. L. Brongersma, "Self-limited plasmonic welding of silver nanowire junctions," *Nat. Mater.*, vol. 11, no. 3, pp. 241–249, 2012.
[25] L. Hu, H. Wu, and Y. Cui, "Metal nanogrids, nanowires, and nanofibers for transparent electrodes," *MRS Bull.*, vol. 36, no. 10, pp. 760–765, 2011.
[26] H. Wu, L. Hu, M. W. Rowell, D. Kong, J. J. Cha, J. R. McDonough, J. Zhu, Y. Yang, M. D. McGehee, and Y. Cui, "Electrospun metal nanofiber webs as high-performance transparent electrode," *Nano Lett.*, vol. 10, no. 10, pp. 4242–4248, 2010.
[27] S. Luan and G. W. Neudeck, "An experimental study of the source/drain parasitic resistance effects in amorphous silicon thin film transistors," *J. Appl. Phys.*, vol. 72, no. 2, pp. 766–772, 1992.
[28] Y. Xu, R. Gwoziecki, I. Chartier, R. Coppard, F. Balestra, and G. Ghibaudo, "Modified transmission-line method for contact resistance extraction in organic field-effect transistors," *Appl. Phys. Lett.*, vol. 97, no. 6, 2010.

Chapter 4. High Aspect Ratio Titanium Dioxide Stabilized Zinc Oxide Nanowires for Photocatalytic Hydrogen Gas Harvester

4.1. Introduction

There have been growing interest in the field of hydrogen production through the photoelectrochemical (PEC) water splitting process because of its potential to passively convert solar energy into hydrogen gas [1]. After Fujishima and Honda's first report of water splitting using an n-type TiO_2 electrode [2], numerous studies have been conducted to achieve stable and efficient PEC systems using materials responsive to the solar spectrum [3]–[5]. However, the state-of-art devices show three major drawbacks: (1) low conversion efficiency due to recombination and poor quality of materials; (2) high onset voltages (requiring a voltage bias to begin the red/ox of water); and (3) poor material stability in the photocatalytic process [6]. Thus, research has focused on either the stabilization layers or the increase of conversion efficiencies [7].

In this research, we present a high aspect ratio Titanium Dioxide (TiO_2)/Zinc Oxide (ZnO) nanowire array (over 8 μm tall) based on a fabrication process using the hybrid hydrothermal process and the atomic layer deposition (ALD) process to construct a solar-powered hydrogen gas (H_2) harvester. TiO_2-stabilized ZnO nanowires show better chemical stability in aqueous solutions during the photocatalytic process. Furthermore, our PEC devices show good onset voltage due to enhanced charge separation induced by increasing the aspect ratio of the system to limit the traveling distance of the minority carriers into the solution.

4.2. Sustainable, renewable energy sources

4.2.1. Motivation

During the past century, the power consumption of the world has increased exponentially. In 2011, 15 TW of power was used for nearly 7 billion people over the world and 30 TW of power is estimated to be consumed for ~9 billion people by 2050 [8]. Even though fossil fuels can provide about 85% of the current energy supply, they will not be able to satisfy the future demand due to limited resources. Based on the current energy consumption rate, it is expected that oil will be depleted in 60 years. For this reason, there are many reports about the energy consumption paradigm shift from the oil and fossil fuels to renewable energy resources. Considering the current technologies for the renewable energy, a lot of research has focused on the electricity generation such as solar cells, wind power, and hydroelectricity as shown in **Fig. 4.1**.

Figure 4.1 Renewable energy sources. Image taken from *lifefreeenergy.com*

An important missing point in **Fig. 4.1**, an image depicting energy sources, is the production of chemical fuels from renewable energy sources such as the photoelectrochemical processes. Photoelectrochemical water splitting is not intended to replace the solar photovoltaics, but to generate chemical fuels using solar energy.

Interest in hydrogen as an energy source started from the surge in the oil price in the 1970s. **Fig. 4.2** is the chart for the West Texas Intermediate (WTI) oil price from 1960 to 2014 and the U.S. GDP (Gross Domestic Product). The values were normalized based on the real current dollar. This clearly indicates the correlation between the oil price and U.S. economic growth. When the oil price peaks, U.S. GDP growth becomes flat and periods of low or falling oil prices coincide with periods of GDP increase.

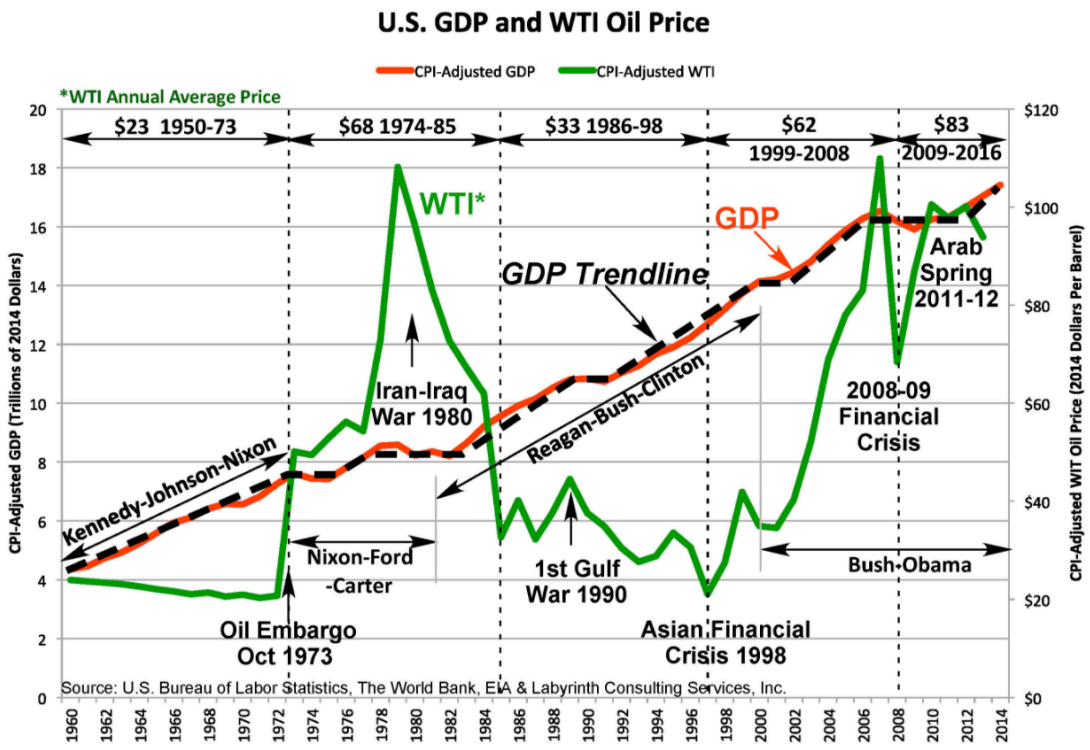

Figure 4.2 U.S. GDP growth versus WTI Oil Price. Image take from *Forbes*

During the oil price surge in the 1970s to 1980s, many researchers began to investigate hydrogen as a replacement for fossil fuels. Hydrogen is a highly versatile fuel that can be converted into the electricity using a fuel cell or directly drive an internal combustion engine. One main benefit is its high specific energy density (kJ/g), which is three times better than gasoline and seven times better than coal (**Table 4.1**). In addition, hydrogen is a clean energy source. The only product after the chemical reaction is pure water. Furthermore, the hydrogen extraction process from water using the solar energy is attractive because water is convenient to obtain and abundant. Just 0.01% of annual rain supply (~3.5×10^{13}L) can provide enough hydrogen to sate energy usage of the world in 1 year (4.7×10^{20}J). Conversion to electricity from hydrogen is easier than with other fuels because there are only the two-electron and four-electron transfer reactions involved for the reduction and oxidation processes whereas carbon-based fuels (methanol or methane) need more complex process of six or eight transfer steps.

One of the main drawbacks of hydrogen is the difficulty in storage. As shown is **Table 4.1**, hydrogen has only about a quarter of volumetric energy density of natural gas whereas its specific energy density is three times bigger than that of the natural gas. For this low volumetric density, considerable volume of storage is required for hydrogen. Thus, there has been a lot of research devoted to solving this issue, looking to conventional methods such as high pressure storage, liquid cryo-storage, and also the physisorption using metal organic frameworks (MOFs), and the clathrate hydrate cages. Recently, the formation of a chemical bond using metal hydrides has attracted a lot of attention since it has an easier route than the photochemical or electrochemical activations of CO_2. Furthermore, a lot of people believe that hydrogen is not

safe for its flammability. However, this is a misconception. Hydrogen flammability is lower than that of methane and is almost the same as natural gas. According to a Ford Motor Company report to the US Department of Energy, hydrogen fuel cell vehicle systems are potentially better than gasoline, propane, and natural gas in terms of fuel safety.

Fuel	***Energy Density***	
	Gravimetric(MJ/kg)	***Volumetric(MJ/L)***
Coal	24	-
Wood	16	-
Gasoline (Petrol)	44	35
Diesel	46	37
Methanol	20	18
Natural gas	54	0.036
Hydrogen	143	0.011

Table 4.1 Gravimetric and volumetric energy densities of several fuels at 1 bar [8].

4.2.2. Hydrogen production

As shown in **Fig. 4. 3**, about 96% of hydrogen of the world produced is from fossil fuels. Among various fossil fuels, most of the hydrogen production comes from the natural gas (48%) via steam-methane reforming (SMR), and the rest of the production derived from coal (18%) and oil (30%) [9]. Steam-methane reforming is a process in which high temperature steam reacts with natural gas at a high pressure with a catalyst to form a mixture of hydrogen and carbon monoxide. After the first reaction, the carbon monoxide from the first step reacts with additional steam to produce carbon dioxide and hydrogen. And this water gas shift reaction is followed by the pressure swing absorption to condense and remove all the carbon dioxide and impurities.

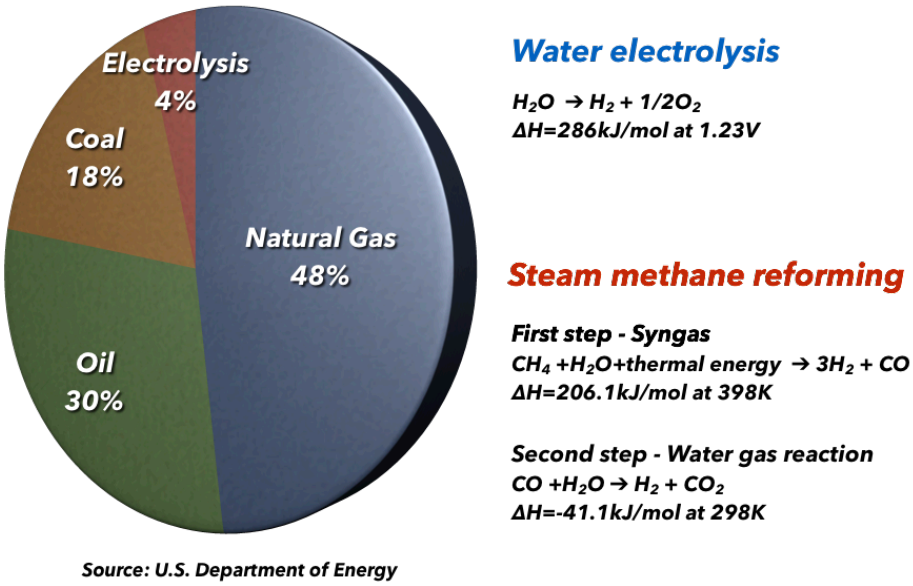

Figure 4.3 World hydrogen production [9].

Though billed as clean-fuel, hydrogen produced by fossil fuel sources for hydrogen production are not saving much green-house gas. Actually, 4% of raw hydrogen is produced from water (electrolysis). Most of the raw hydrogen is produced from the natural gas. The reason can simply be explained by comparing chemical reactions for the electrolysis and the steam-methane reforming. In electrolysis, hydrogen is much more tightly bonded in a water molecule than in methane. Therefore, the low portion of hydrogen production from the electrolysis looks reasonable in terms of economic production costs. But the idea behind photoelectrochemical water splitting is that the chemical reactions for producing the hydrogen source can be driven and supplied by solar energy. It would become economically meaningful to produce hydrogen from the water since we can obtain the input, solar energy, basically, for free.

4.3. Photoelectrochemical water splitting

4.3.1. Fundamentals of photoelectrochemical water splitting

As discussed in the previous section, the motivation of photoelectrochemical water splitting is as a viable renewable energy technology. There are several reasons why photoelectrochemical water splitting is attractive. First, hydrogen and oxygen can be produced in separate electrodes and, thus, the safety concern about explosion can be avoided. In addition, easy separation of hydrogen and oxygen can save costs of post-separation process. Second, since photoelectrochemical water splitting can be performed at room temperature, it does not require large-scale solar concentrators which can restrict the application to large facilities in sunny regions. Lastly, photoelectrochemical water splitting devices can be constructed using inorganic materials for robustness and good durability as compared with organic or biological systems [9].

In most photoelectrochemical cells, there are two electrodes immersed in an electrolyte. At least one of these electrodes is made of material to absorb light, typically a semiconductor (thus, a photo electrode or working electrode). If the photo electrode is made of an n-type semiconductor, it is a photo anode (because the oxidation of water molecules happens at the anode). Photo anodes are usually light absorbing materials and charge accumulation layers. On the other hand, a photo active material can also be as a cathode when the photo electrode is made of a p-type semiconductor. **Fig. 4.4** shows the typical photoelectrochemical cell design. In the photo-anode, the light excites the photo-active material and photo-anode will generate electron-hole pairs by absorbing the photo energy. The charge can be separated by the built-in field and the separated charges will be transferred by using different pathways. Holes will travel toward the surface of the photo anode whereas electrons will travel towards the cathode through an external circuit. When the holes reach the surface of the photo-anode, they can take part in the oxidation of two molecules of water thus producing one oxygen molecule. This is known as oxygen evolution reaction (OER). Meanwhile, the proton travels through the electrolyte, reaches the cathode and hydrogen evolution reaction (HER) can then take place. To split the water, a minimum theoretical voltage of 1.23V is required at room temperature. However, in order to make the reactions proceed with considerable rate, additional energy is required and it is called an activation energy. Obviously, the additional energy should be greater than the 1.23V and the 'overpotential' describes how much additional voltage must be supplied to obtain a given current density [10].

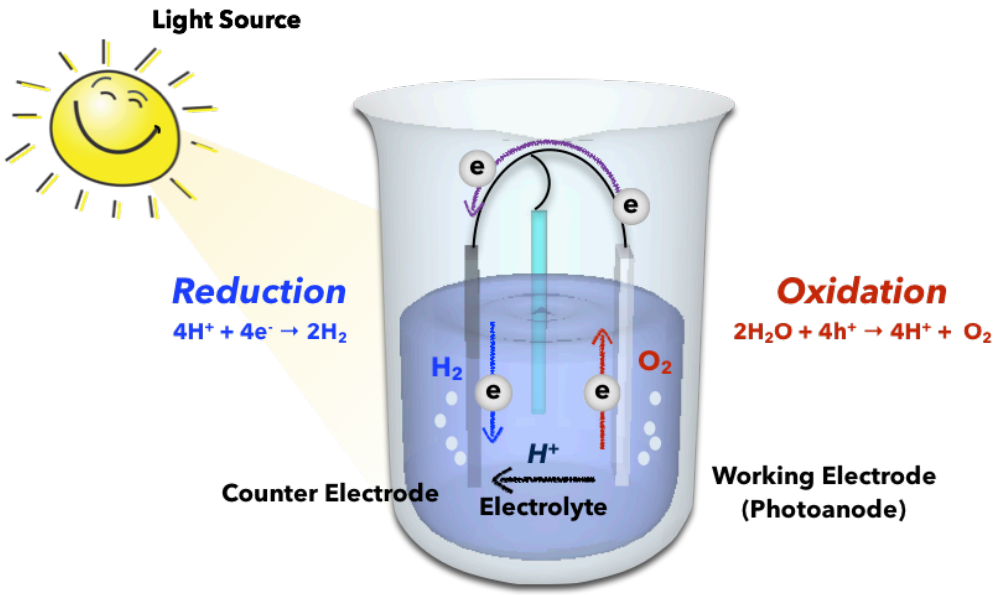

Figure 4.4 Photoelectrochemical cell design

4.3.2. Semiconductor-electrolyte interface

Looking at things more closely, most of the reactions in **Fig. 4.4** actually take place at the semiconductor and electrolyte interface. **Fig. 4.5(A)** shows the typical energy band diagram of the photo-anode, a semiconductor material, that has energy band gap, conduction band edge, valence band edge and Fermi level. In solid state physics, the space charge region (SCR) is formed by a contact between a metal and a semiconductor or a semiconductor and another semiconductor [11], [12]. When two materials have different Fermi levels, free carriers in a material with higher Fermi lever are transferred to another material until they reach the equilibrium. However, in the metal oxide semiconductors, built-in potential can be established at the surface without contact between materials. **Fig. 4.5** illustrates the formation of the space charge region of metal oxides in a moisture-rich environment. When a metal oxide is exposed to water molecules, they produce OH- termination groups by combining with metal oxides on the surface. These hydroxide groups form surface states in the band gap of the metal oxide semiconductor by breaking the metal lattice symmetry. Since the surface states are located below the conduction band edge, free electrons from the ionized donor will move from bulk to the surfaces states until the equilibrium is established. This is how the space charge region forms in the bulk without making a contact with another solid.

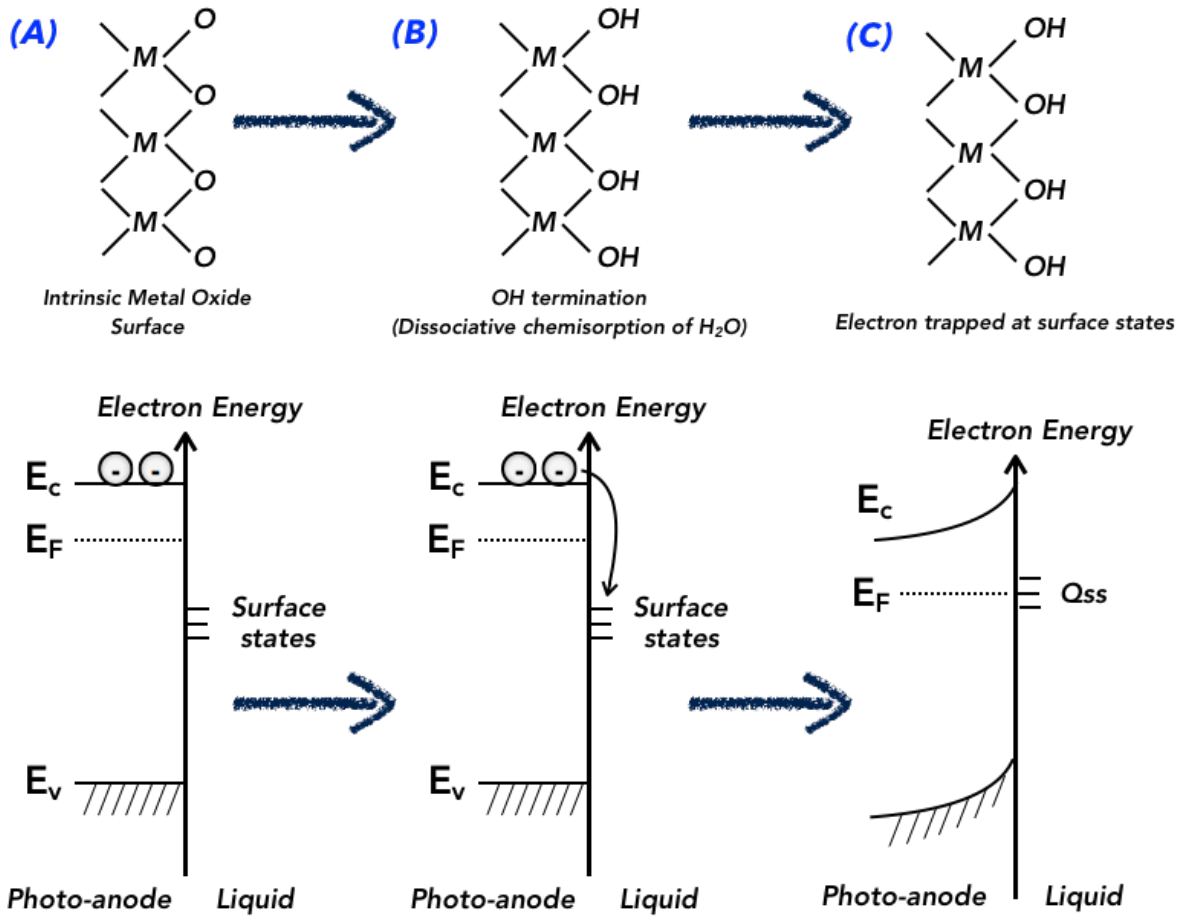

Figure 4.5 Simplified illustration of the formation of a space charge region (SCR) at a metal oxide semiconductor when exposed to moistures [8]

The behavior of mobile carriers in the liquid electrolyte is different from the carriers in solid semiconductors. For solid materials, atoms are confined with their neighboring atoms such that mobile carriers (electrons and holes) can travel through the atomic network. However, in a liquid electrolyte, only charged ions can travel through the material and carry charge. Therefore, when the ionic species are brought into contact with a metal or another semiconductor, the ionic species are oxidizing or reducing the solid material by transferring mobiles carriers. The tendency of reduction and oxidation is dependent on the ionic species. This tendency can be expressed as a corresponding electric potential and called standard electrode potential or redox potential (E^0_{redox}). More precisely, this redox potential is composed of coupled energy distribution functions which are located apart from each other; this concept is very similar to the Fermi level in solid state physics. **Fig. 4.6** illustrates the electrochemical reaction at the semiconductor-electrolyte junction. When the Fermi level of the semiconductor material is higher than the redox potential, electrons in the semiconductor move to the electrolyte. Thus, in the liquid electrolyte, the number density of polar ions increases due to the chemical reaction until they establish the equilibrium between the Fermi level of semiconductor and the redox

potential of the liquid electrolyte. Similar to semiconductor to metal contact, carriers in the semiconductor are depleted soon and band bending is formed over the space charge region.

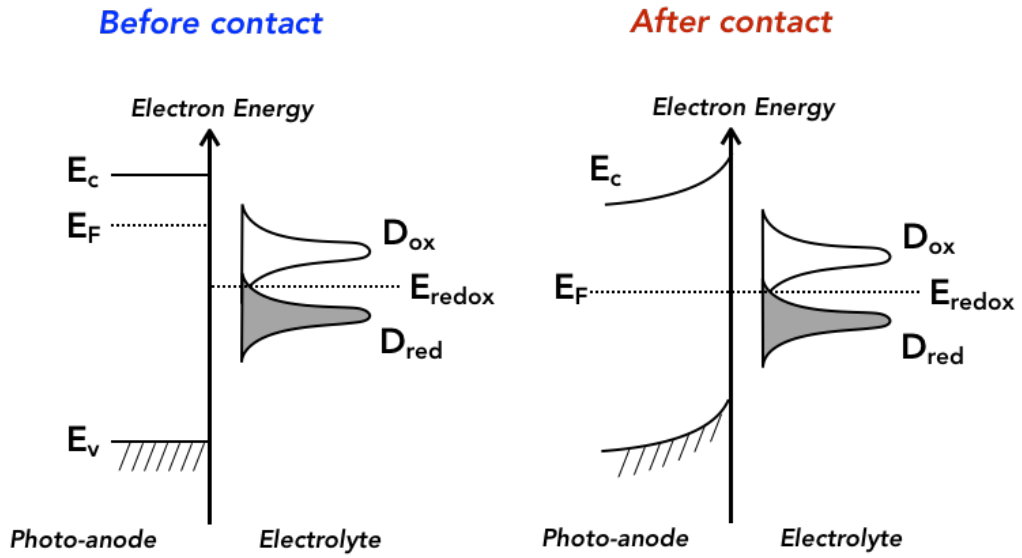

Figure 4.6 Semiconductor and electrolyte junction diagram (A) before contact (B) after contact

The potential distribution and the width of the space charge region (SCR) can be determined by the amount of charges transferred to the surface and the net donor concentration of the material (N_D). From the Poisson's equation,

$$\frac{d^2\varphi}{dx^2} = -\frac{d\boldsymbol{\varepsilon}}{dx} = -\frac{\rho(x)}{\epsilon_s} \tag{4-1}$$

where the φ, ε, ρ, and ϵ are the charge potential, the electric field, the charge concentration and the dielectric constant for the semiconductor material. By applying the Boltzmann distribution to describe the charge distribution in the SCR and Gauss's law relating the electric field through the charges in the region, the total amount of charge in the SCR can be described as [8]:

$$Q_{SC} = \sqrt{2\epsilon_s e N_D A^2 \left(\varphi_{SC} + \frac{kT}{e} e^{-e\varphi/kT} - \frac{kT}{e}\right)} \tag{4-2}$$

where the φ_{SC} is the amount of potential drop in the SCR due to the band bending and A, k, and T are the cross-sectional area of the band bending, Boltzmann's constant and the absolute temperature. Under the normal PEC operating condition, the potential drop in the SCR is at least 0.1V and **Eq. (4-2)** can be simplified to:

$$Q_{SC} = \sqrt{2\epsilon_s e N_D A^2 \left(\varphi_{SC} - \frac{kT}{e}\right)} \tag{4-3}$$

by using the relation between the total amount of charge and the depletion thickness,

$$Q_{SC} = eN_D AW \tag{4-4}$$

the width of the space charge region is given by

$$W = \sqrt{\frac{2\epsilon_s}{eN_D}\left(\varphi_{SC} - \frac{kT}{e}\right)} \tag{4-4}$$

For the p-type semiconductor material, this expression is still valid. By exchanging N_D to N_A, we can easily obtain the space charge width for photocathode material. An impedance measurement is typically used to obtain the actual values for the dopant density and the depletion width. The differential capacitance of the space charge, C_{SC}, can be extracted from the total impedance under the certain condition. The expression for C_{SC} is given by using Eq. (4-3) and rewritten as:

$$\frac{1}{C_{SC}^2} = \frac{2}{\epsilon_s e N_D A^2}\left(\varphi_{SC} - \frac{kT}{e}\right) \tag{4-5}$$

This equation is called "Mott-Schottky" equation and, from this equation, the value of N_D is conveniently found by plotting $1/C^2$ as a function of applied potential φ.

When a metal oxide is immersed into an aqueous solution, the situation is slightly more complicated due to the pH of the solution. Charge distribution at the semiconductor-electrolyte interface can affect the absorption of proton/hydroxide species. Absorption and desorption of H^+ and OH^- ions from the surface will continuously change its pH level of the aqueous solution until the dynamic equilibrium established. The following equations describe the protonation and deprotonation reactions [8]:

$$M - OH \overset{k_a}{\leftrightarrow} MO^- + H_{aq}^+ \tag{4-6}$$

$$M - OH + H_{aq}^+ \overset{k_b}{\leftrightarrow} M - OH_2^+ \tag{4-7}$$

The pH level of the solution determines the equilibrium of these reactions and the net total charge at the surface will be changed. Thereby, charge distribution and potential distribution is also affected. To understand the thermodynamics of PEC devices, the energy band diagram is essential and we can easily establish the energy band diagram by analyzing the potential distribution.

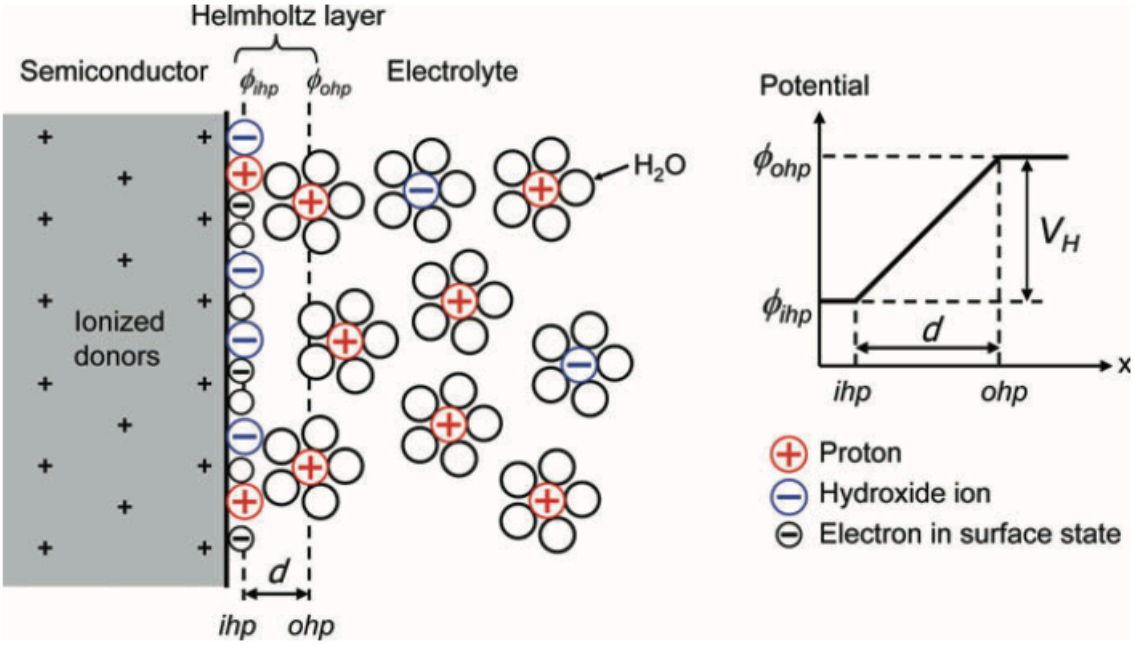

Figure 4.7 Schematic model of the semiconductor/electrolyte interface and the Helmholtz layer. Image taken from [8]

There is another interesting phenomenon at the interface between the semiconductor and the liquid electrolyte. When the electrons (or holes) are trapped at the surface states, both the counter charges provided by ionized donors or acceptors in the semiconductor and the oppositely charged ions in the liquid solution will accumulate on the surface. All ions in the solution will be surrounded by the water molecules due to their large dipole moment. These water molecule clouds are bigger than charged ions in size, thus, they prevent them from approaching the surface closer than a few angstroms as shown in **Fig 4.7**. Therefore, there exist a double layer of positive and negative charges one molecule thick in the solution and is called the *Helmholtz layer*. The potential drop across this layer is described as

$$V_H = \varepsilon d = \frac{Q_s d}{\epsilon_s} \tag{4-8}$$

The width of the Helmholtz layer is ~2-5Å, and on such a small length scale the dielectric constant of water is evaluated to be ~6, this value is much smaller than its bulk value of 80 [13]. **Fig. 4.8** shows the energy diagram for PEC with a n-type photo anode and the metal contact. The potential drop due to the Helmholtz layer is also presented at the metal/electrolyte interface.

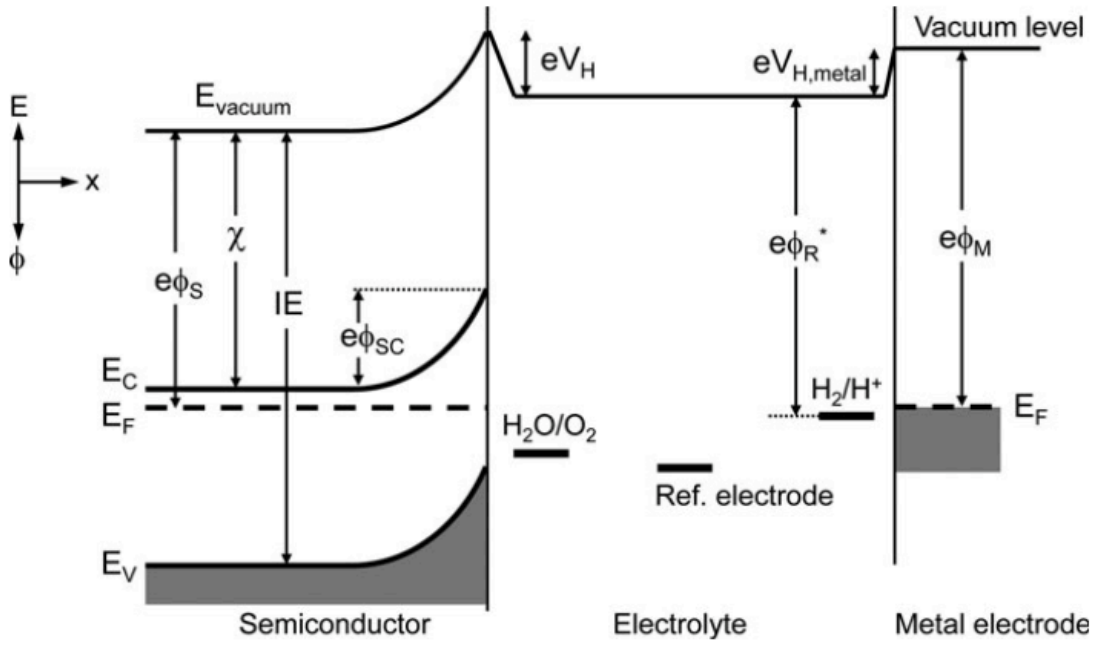

Figure 4.8 Energy diagram for a PEC with n-type photo-anode and a metal contact. Potential drop due to the Helmholtz layer is presented for both interface (semiconductor/electrolyte and metal/electrolyte). Image taken from [8].

4.3.3. Design criteria for PEC cells

There are basically several requirements for the photo anode. First, as shown **Fig. 4.9**, is the band position. The conduction band edge of the photo-anode should be above the hydrogen reduction potential and the valence band edge needs to be blow the photo-oxidation potential so the holes can move from the photo-anode to oxidize the water and electrons can move to the counter electrode through the external circuit.

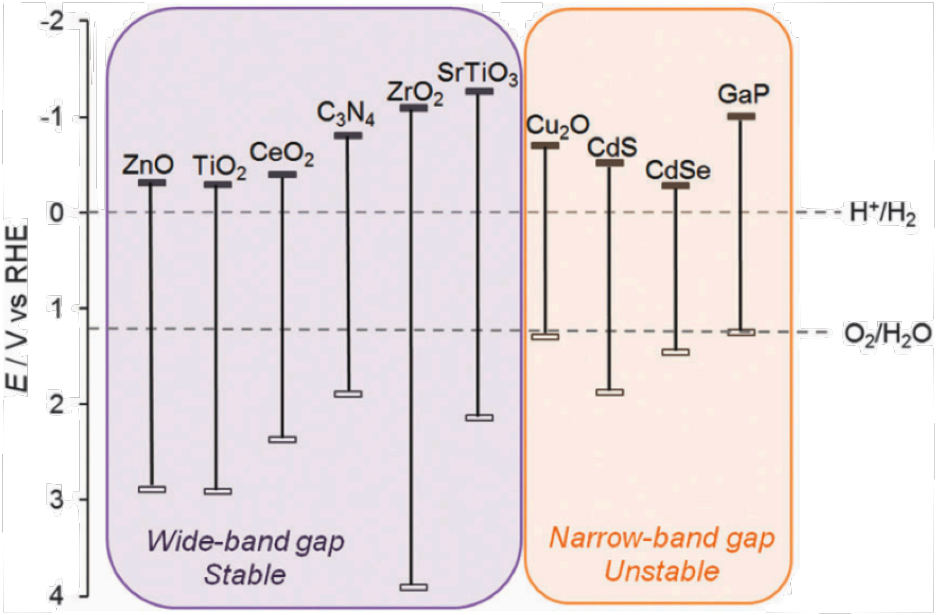

Figure 4.9 Band edge positions for various semiconductor materials. (in V *vs.* RHE) [14].

Second, the material obviously needs to be stable in the photoelectrochemical cell. This is an especially difficult criterion because the water splitting reaction creates highly oxidized species. The general trend is that stability against photo-corrosion reaction improves as the energy bandgap of the material increases. Even though the absorption of the visible light deteriorates in a material with a large energy bandgap, the chemical stability and a small energy bandgap do not need to be mutually exclusive. Thirdly, an efficient charge transport is also an important factor for good PEC performance. For the materials with the poor charge separation efficiency, electron-hole pairs generated by the photon energy can recombine and, thus, cannot contribute to the hydrogen evolution reaction and oxygen evolution reaction. The carrier life time, τ_R, or the minority carrier diffusion length, L_D, describe how easily the minority carriers can recombine in a material. Carrier life time and diffusion length are related as [8]:

$$L_D \sim \sqrt{D_{\tau R}} \tag{4-9}$$

The diffusivity of the free carriers, D, is related to their mobility, μ, via the Nernst–Einstein equation:

$$\frac{D}{\mu} = \frac{kT}{q} \tag{4-10}$$

Values of L_D are ranging from several nanometers to several hundred nanometers.

Ideally, we want the material to be cheap and abundant for low cost production and the material with high visible light absorption is required for better PEC performance. Therefore, all

of those requirements will determine the materials needed for a PEC cell. In addition, charge separation efficiency and the amount of light absorption can be improved by changing the geometry of the material.

4.4. Nanostructured metal oxides for PEC cell

4.4.1. Metal oxide for photoelectrochemical water splitting

A high mobility and a large band gap are generally desirable for PEC water splitting cells. This is because materials for PEC cells require enough thickness for absorbing all the incident light, so electrons and holes generated from the photo absorption have to travel a long distance to reach the interface. In order to achieve better stability against the photo-corrosion reaction of the material, a large band gap is favorable.

The bonding in metal oxide is very different from that in Si semiconductors where hybridized sp^3 σ-bonding and sp^3 anti σ-bonding states consists of the valence band edge and conduction band edge as shown in **Fig. 4.10**. Since the electronegativity of oxygen is much higher than metal, the valence band is composed of occupied *2-p* oxygen anti-bonding states and the conduction band is primarily composed of unoccupied *ns* metal bonding states. Hence, the nature of bonding states in metal oxides is highly polar or even ionic. Typically, materials with strong ionicity shows the large energy bandgap. This is why metal oxide materials exhibit large energy band gap. **Fig. 4.11** shows an example for rutile and anatase TiO_2.

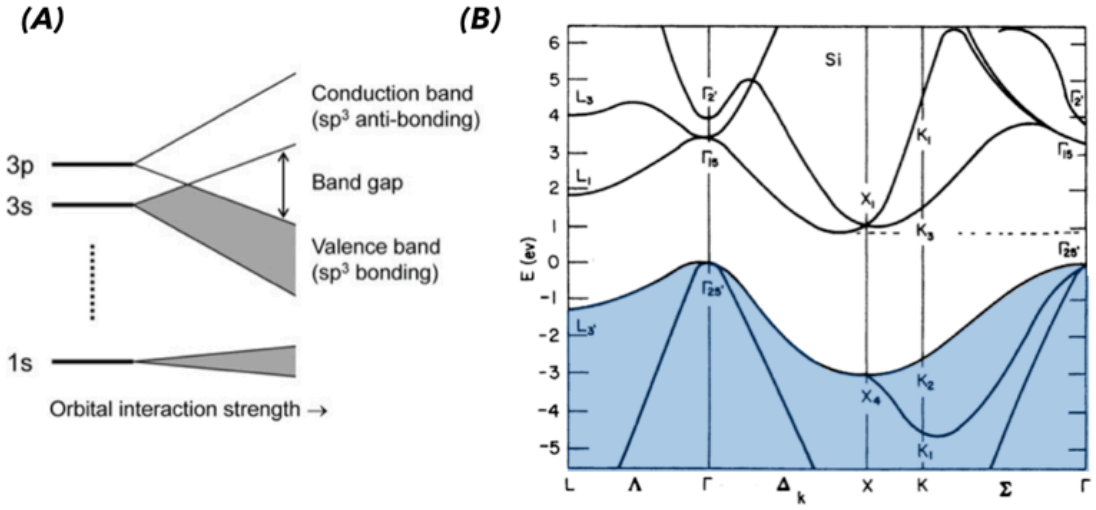

Figure 4.10 (A) Formation of the valence and conduction band in covalent semiconductors. (B) Calculated energy band structure of silicon (diamond-cubic crystal structure, the bluish area indicates the occupied states in valence band of the material [15].

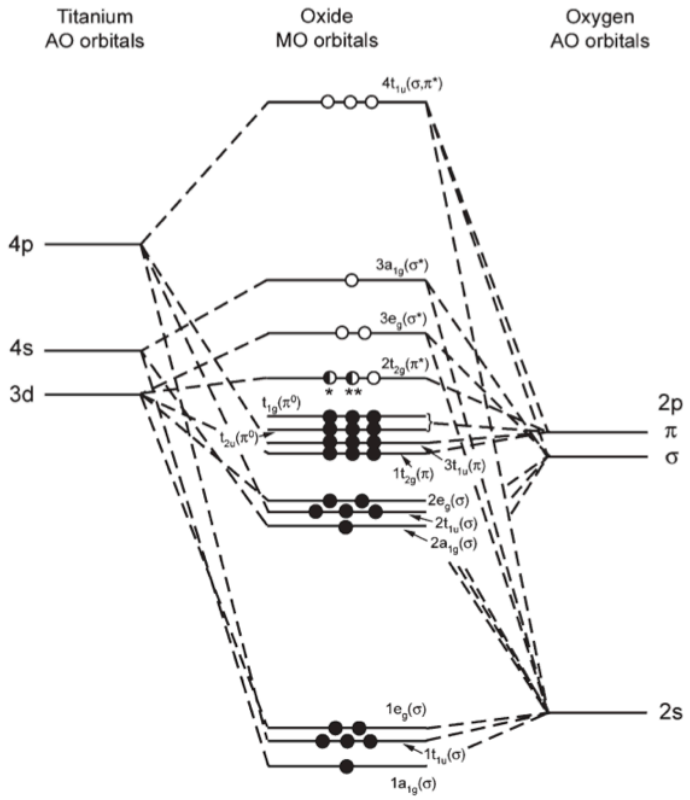

Figure 4.11 Molecular-orbital diagram for rutile and anatase of Ti_xO_y [16]

As we discussed in Chapter 2, metal oxide materials show a higher electron mobility even in the amorphous phase because they are insensitive to the lattice distortion due to the spherically symmetrical *ns*-orbital overlapping with neighboring metal *ns*-orbital in metal oxide materials. This is the reason why metal oxides became the most popular material for PEC cells.

4.4.2. Nanostructured materials

Nanostructured materials can be employed to address some intrinsic limitations of material. Obviously, nanostructured morphology greatly improves the specific surface area and thereby enhances the overall charge transfer kinetics at the semiconductor/electrolyte interface. Another benefit is the reduced minority carrier distances for the photo-generated charge carriers. **Fig. 4.12** illustrates the nanowire array for the photo-electrode where the minority carriers only need to travel half the diameter of the nanowires to reach the semiconductor/electrolyte interface [4].

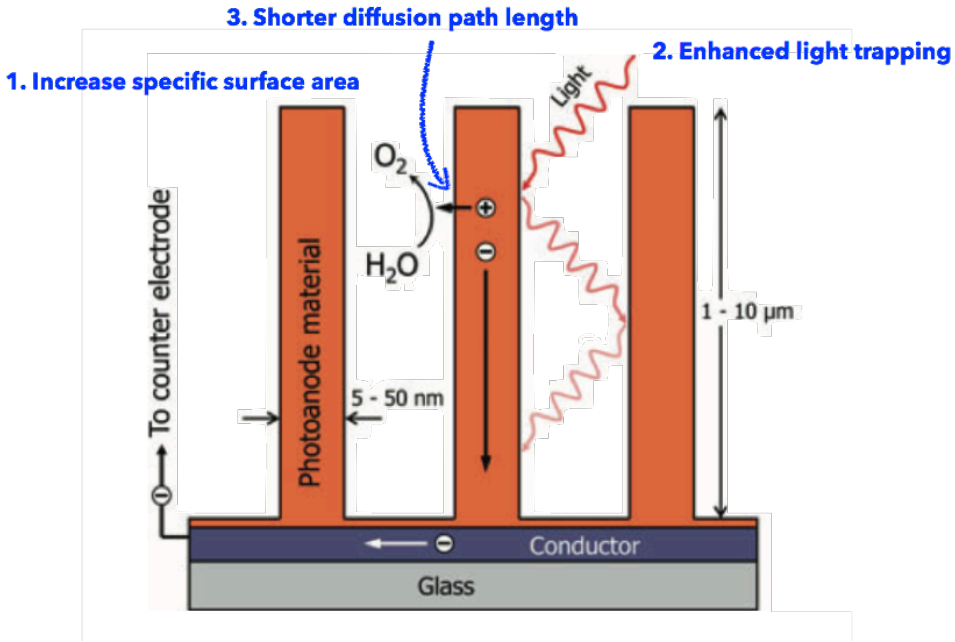

Figure 4.11 Geometry of photoelectrode using nano wires and advantage of nanowires [8]

In nanowires, light absorption can be improved by increased light trapping. When the diameters of nanowires are smaller than or comparable to the radiation wavelength, optical interference and guiding effects plays a pivotal role regarding reflectivity and absorption spectra. For direct bandgap material such as GaAs, resonances are mainly attributed to increasing the total absorption. However, in indirect bandgap material such as silicon, wave-guiding effects are dominant [17], [18].

4.5. Concept and experiments of high aspect ratio TiO_2 stabilize ZnO NWs for photocatalytic hydrogen gas harvester.

4.5.1. Concept and material selection

Fig. 4.12 shows the conceptual schematic of photocatalytic H_2 gas harvesting system. In this research, we introduce high aspect ratio ZnO nanowires with a TiO_2-coated stabilizing active layer for improved stability during photocatalysis and increased hydrogen production at low bias potentials. The photocatalytic H_2 gas harvesting system consists of a photoelectrode and a counter electrode submerged in an aqueous electrolyte solution. In the photoelectrode, light absorption generates electron-hole pairs to promote electrons from the valence band to the conduction band. A Schottky barrier is formed at the photoelectrode-electrolyte interface. With properly chosen electrolyte solution (potential) and photoelectrode (Fermi level), minority carriers move into the electrolyte and begin reduction/oxidation (depending on whether the photoelectrode is p- or n-type) of water. Majority carriers oxidize/reduce water at the counter

electrode-electrolyte interface. **Fig. 4.13** shows the energy band diagram for photocatalytic system using a TiO_2 photoanode.

TiO_2 is an intrinsically n-type semiconductor material with an energy band gap of 3.2 eV [19]. Its band edge positions straddle water redox potentials as shown in **Fig. 4.13**. Moreover, the TiO_2 production is cheap, scalable, while TiO_2 is chemically stable in aqueous solutions. However, the state-of-art TiO_2 is plagued by lower photocurrent due to poor light absorption and previous work on texturizing TiO_2 is not able to produce high aspect ratio TiO_2 nanowires. Instead, undesirable compact layers are observed at the bottom of the wire arrays [20]. In this work, we fabricate high aspect ratio TiO_2 nanowire arrays using a hybrid hydrothermal/atomic layer deposition (ALD) process. After growing the high aspect ratio ZnO nanowires using the hydrothermal method, a uniform coating of TiO_2 was applied by ALD.

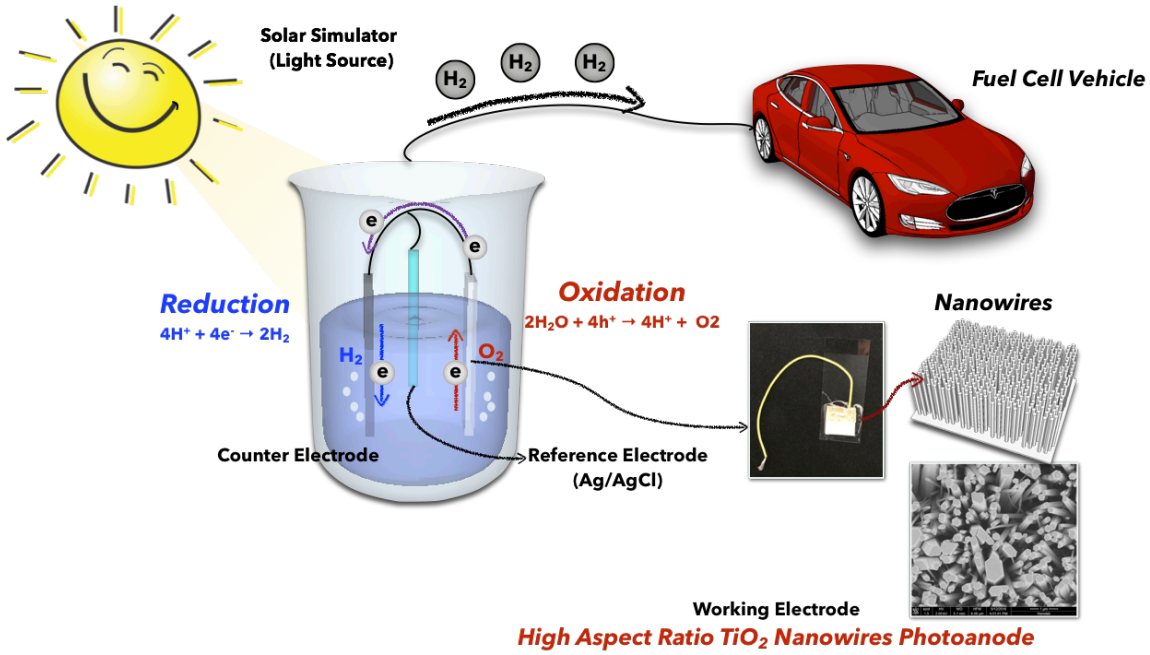

Figure 4.12 Conceptual illustration of a photocatalytic system. Light induces electron-hole pair generation at the photoanode, oxidizing water to produce hydrogen ions and oxygen gas. The generated electrons reduce the hydrogen ions at the photocathode producing hydrogen gas.

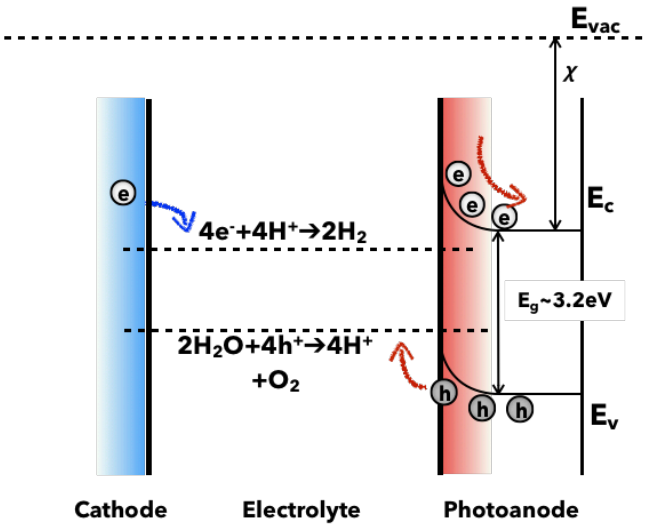

Figure 4.13 Band position and band bending of TiO_2 at the interface between semiconductor and electrolyte

4.5.2. Fabrication process and sample preparation

A two-step hybrid process was used to fabricate the PEC water splitting devices. First, zinc oxide (ZnO) nanowires were fabricated by a hydrothermal process. Second, atomic layer deposition (ALD) was used to deposit 40 nm-thick TiO_2. **Fig. 4.14** illustrates the fabrication process of high aspect ratio TiO_2/ZnO nanowires.

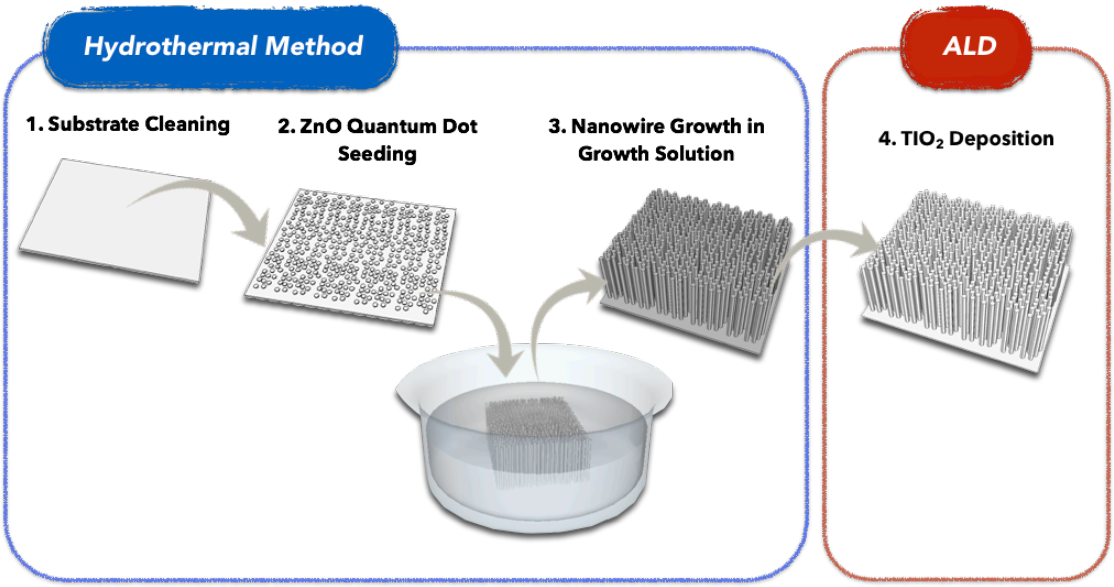

Figure 4. 14 Schematic of fabrication process of high aspect ratio TiO_2/ZnO nanowires.

To fabricate ZnO nanowires, a seed solution of zinc acetate (Sigma Aldrich) and ethanol were drop-casted onto n-type Si (100) wafers. The solution was left to form a quantum dot network on the surface of the Si wafers, rinsed with ethanol, and dried under nitrogen environment. The process was repeated 3 times to ensure adequate quantum dot formation. The wafer is annealed at 350ºC for 30 min to ensure the seed layer is adhered onto the wafer. The wafer is then submerged in a growth solution containing zinc nitrate hexahydrate at 90ºC for 8 hrs. The wafer is removed from the solution and cleaned with deionized water. After drying the samples, the uniform deposition of TiO_2 over ZnO nanowires was performed using the atomic layer deposition (ALD), which is a highly precise chemical vapor deposition method to create uniform and conformal coverage of a polycrystalline TiO_2 using the self-limiting reactions. To deposit TiO_2, a precursor, Tetrakis(dimethylamido) titanium (TDMAT), is introduced into the deposition chamber through an argon carrier gas and is allowed to be adsorbed onto the substrate surface for 0.6 s. Excess (unabsorbed) TDMAT is removed from the chamber with Argon gas for 5 s. Next, H_2O is introduced for 0.25 s to begin a self-limiting reaction with adsorbed TDMAT. The excess H_2O and reaction byproducts are removed with Argon gas for 5 s, leaving a single layer of TiO_2. In the way, gaseous precursors are introduced in a systematic and cyclic manner to create a self-limiting reaction—one layer of TiO_2 is deposited per cycle. This makes ALD an ideal deposition method with high quality, Ångström-level precision over very high aspect ratio substrates. The ZnO nanowire array was coated by 800 cycles of thermally grown ALD TiO_2 (~0.4Å/cycle) at a process temperature of 250ºC.

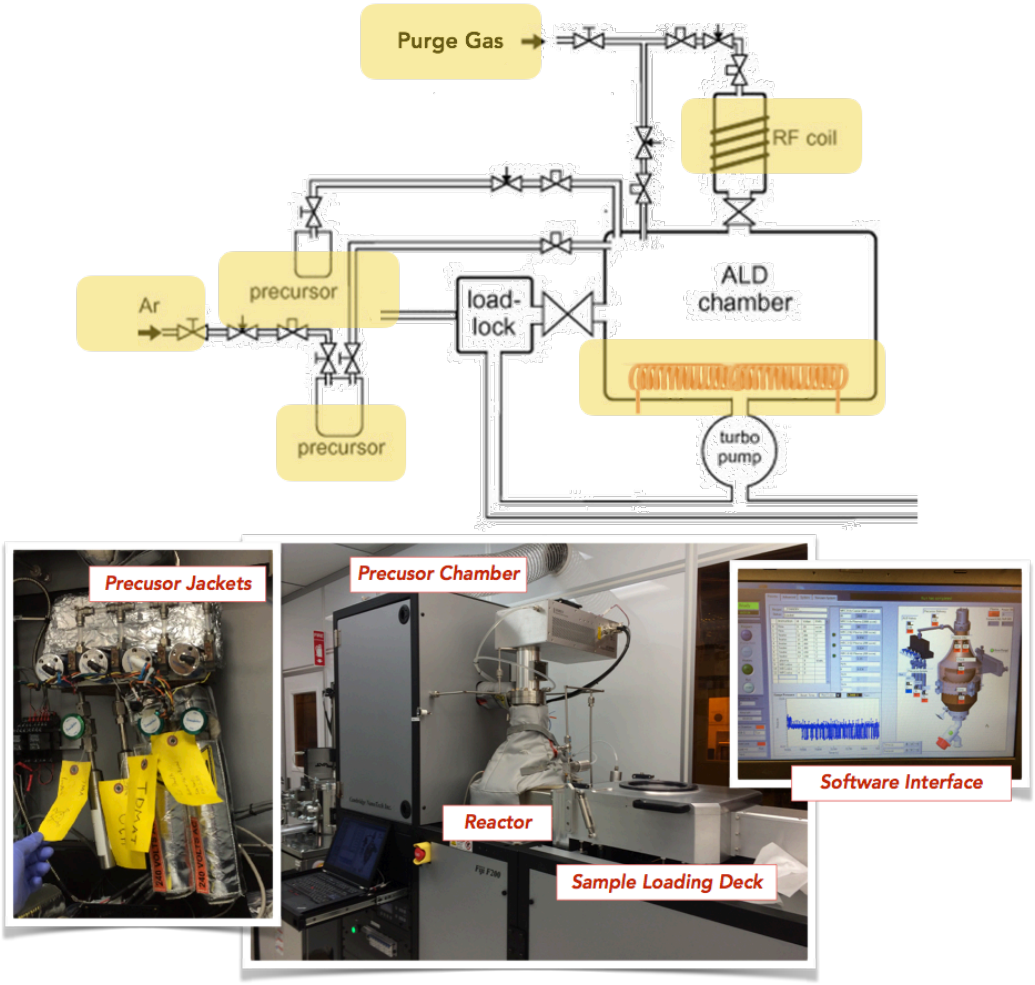

Figure 4. 15 Atomic layer deposition system for the TiO_2 coating process.

Electrical contact is established using a copper tape and insulated tin wire. To isolate the active material, electrodes are passivated onto a glass substrate using the epoxy glue. Photoelectrochemical water splitting experiment is tested using a 3-electrode set-up in 0.5 M H_2SO_4 solution vs. Ag/AgCl with platinum wire as the counter electrode. An Asahi Catec1, AM 1.5 Xenon lamp is used as the solar simulator; the system is enclosed in TB4 Thorlabs black-out hardboard (5 mm thick with foam core). Electrochemical measurements were conducted using a Gamry Ref. 600 potentiostat. **Fig. 4.16** illustrates the prepared photo-anode sample and the test set-up for PEC performance measurement.

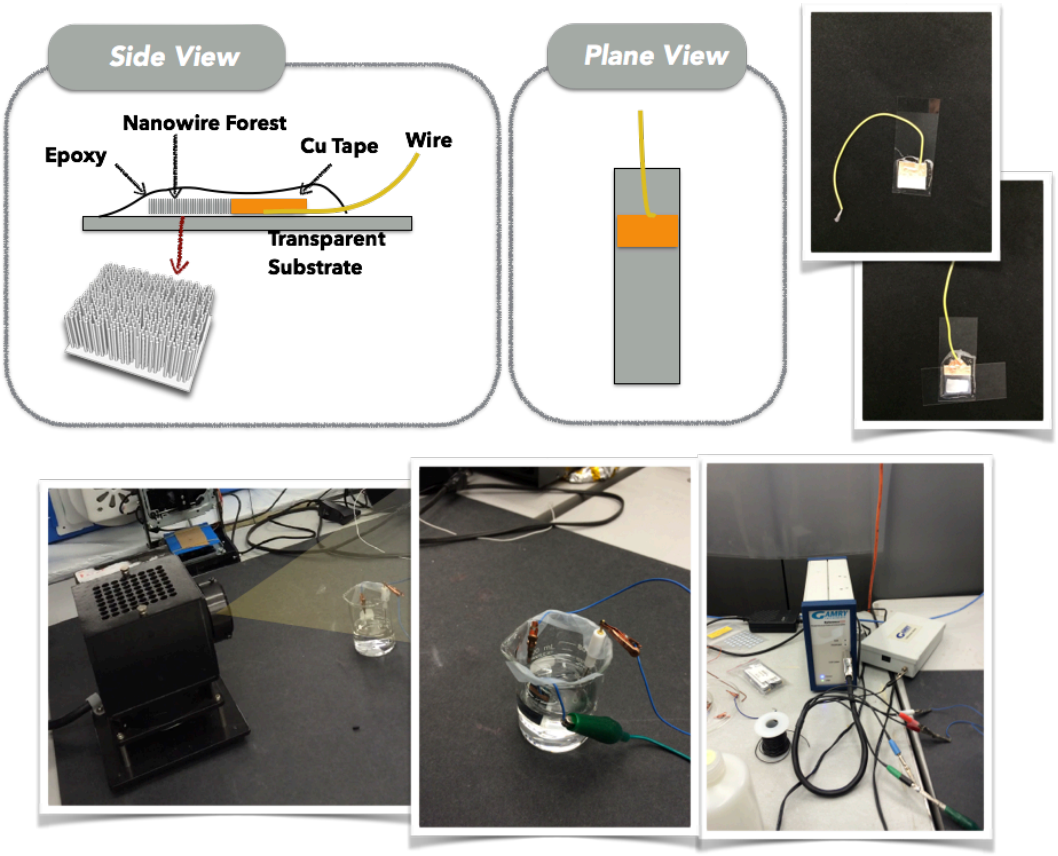

Figure 4.16 Illustration of photo-anode sample and the measurement set up.

4.5.3. Cell efficiency

The efficiency of the cell is represented by the solar-to-hydrogen efficiency calculation [21]:

$$STH = \frac{Representative\ H_2 output\ energy}{Energy\ of\ incident\ solar\ light} = \frac{r_{H_2} \times \Delta G}{P_{sun} \times S} \tag{4-11}$$

where r_{H_2} is the rate of hydrogen production; ΔG is the change in Gibbs energy; P_{sun} is the energy flux of irradiation; and 'S' is the area of the electrode. However, electrodes that require a bias voltage in order to produce measurable photocurrent require voltage compensation in order to calculate cell efficiency. Therefore, the solar-to-hydrogen efficiency and half-cell (to be used with a two-electrode cell) with the applied bias voltage is employed:

$$AB - STH = {|I| \times \eta_F \times (V_{th} - V_{bias})}/{P_{sun}} \tag{4-12}$$

where I is the photocurrent density, η_F is the faradaic efficiency, V_{th} is the theoretical voltage for water splitting (1.23 V), and V_{bias} is the applied bias potential. The half-cell STH for a photoanode is therefore:

$$HC - STH = \frac{|I| \times \left(E_{O_2/H_2O} - E_{RHE}\right)}{P_{sun}} \tag{4-13}$$

where E_{O_2/H_2O} is the theoretical standard electrode potential for the $O_2 + 4H^+ + 4e^- \rightarrow 2H_2O$ reaction vs. RHE; and E_{RHE} is the pH-dependent potential of the photoanode in the electrolyte:

$$E_{RHE} = E_{measured} - E^0_{Ag-AgCl} + \frac{RTln10}{F} pH \tag{4-14}$$

where $E_{measured}$ and $E^0_{Ag-AgCl}$ are the potential measured relative to an Ag/AgCl reference electrode and the standard potential of the Ag/AgCl reaction, respectively. *R, T, F* are the gas constant, temperature, and, Faraday constant, respectively. Therefore, the cell efficiency is not only dependent on the measured photocurrent density but also the applied bias potential. Furthermore, texturization, catalysts, and co-electrodes to promote the charge separation have been readily shown as methods to increase the photocurrent, while fewer works exist on methods to decrease the onset voltage, aside from the material choices.

4.6. Characterization

4.6.1. Surface morphology - SEM

The surface morphology of the nanowire array was analyzed using a field emission scanning electron microscopy (FESEM). The SEM images of the nanowire array after the ALD process show complete and conformal coverages. As shown in **Fig. 4.17 (A),** SEM images before the ALD process show highly ordered, 10 μm-tall nanowires with diameters less than 50 nm. Furthermore, nanowires show polygonal cross-sections, implying the single-crystalline nature. **Figs. 4.17 (B)** and **(C)** show that a single ZnO nanowire is uniformly coated by TiO_2 with 40 nm-thick TiO_2, as opposed to the 8 nm-thick coating of TiO_2, which shows incomplete coverage.

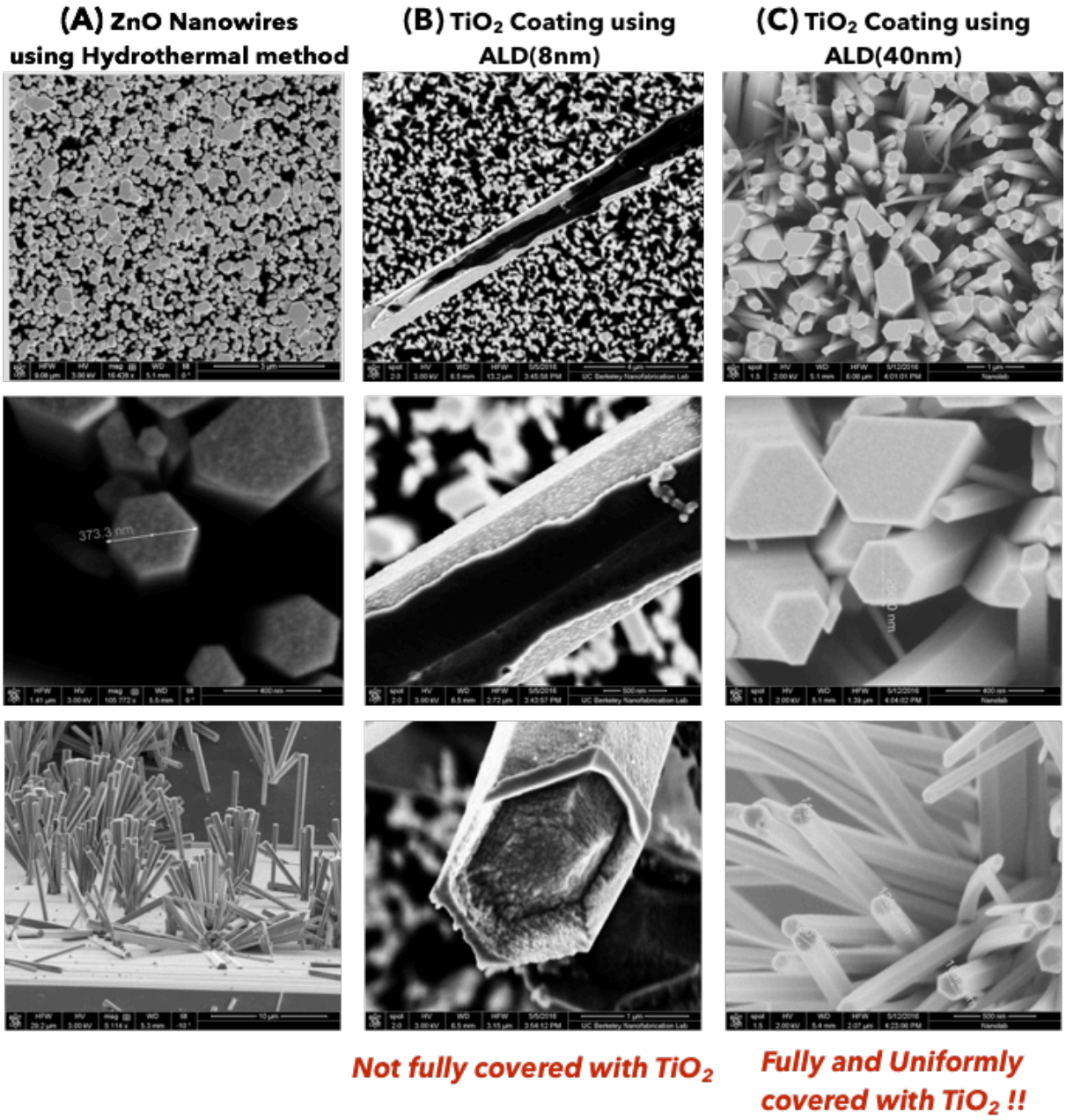

Figure 4.17 SEM image of (A) zinc oxide nanowires (ZnO NWs) by using the hydrothermal growth method; (B) 8 nm-thick of TiO_2 coating on the ZnO NWs showing partial coverages; and (C) 40nm-thick, uniformly coated TiO_2 on ZnO NWs using Atomic Layer Deposition (ALD).

4.6.2. Surface morphology - TEM

A transmission electron microscopy (TEM) was employed. **Fig. 4.18** shows the TEM characterization of a single nanowire removed from the array. **Fig. 4.18 (A)** is the image of a

single nanowire of ZnO before the ALD process and **Fig. 4.18 (B)** shows a TiO_2 coated ZnO nanowire with conformal coverage of the TiO_2.

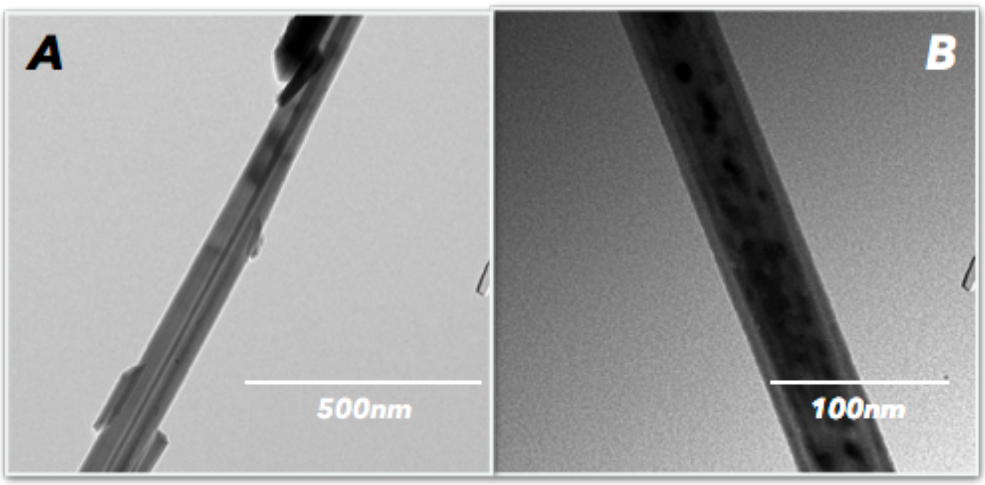

Figure 4.18 TEM images of: (A) ZnO NW grown by using the hydrothermal method; (B) TiO_2 coated ZnO NW using ALD.

The phase structure is characterized using powder X-ray diffraction (XRD). **Fig. 4.19** displays the X-ray diffraction peaks which confirm excellent crystallinity and hexagonal wurtzite ZnO phase (JCPDS card No. 36-1451). Furthermore, in contrast to previous works on TiO_2, we are able to achieve tall and highly ordered TiO_2 arrays around the ZnO nanowires. By using the ALD to deposit a thin coating of TiO_2, we have further limited the distance for the travel of minority carriers to minimize the recombination and ensure better charge separation. The favorable geometry and high quality coating of TiO_2 with ALD allows us to achieve stable devices with excellent onset voltage and photocurrent at a low bias voltage.

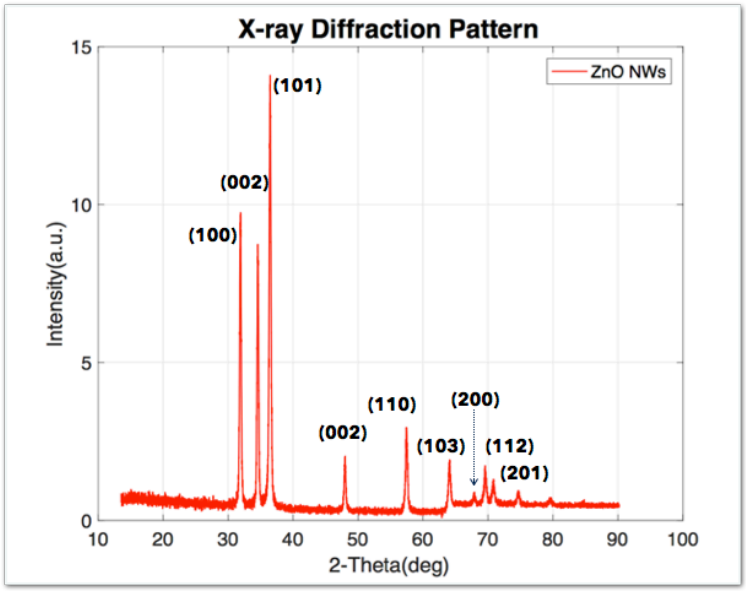

Figure 4. 19 X-ray Diffraction pattern of ZnO nanowires.

4.7. Results and discussion

The photoelectrochemical response is tested in a 3-electrode set-up with Xenon lamp. Linear sweep voltammetry is conducted from 0 V vs. Ag/AgCl to 1 V vs. Ag/AgCl, since the aqueous solution has an electrochemical voltage limit of 1.23 V (standard electrode potential of 1.23 V for the $O_2 + 4H^+ + 4e^- \rightarrow 2H_2O$ reaction). The tests are conducted in dark conditions (covered in a black-out cardboard housing) and under the simulated sunlight conditions, as well as chopped light–dark alternating conditions. As seen in **Fig. 4.20,** the PEC response of the bare ZnO nano-array is mostly obscured by the side reactions, despite cleaning the ZnO nanowires with ethanol and DI water. The side reactions cause local and sharp increases in the recorded current. However, after coating with the ALD TiO_2, the stability of the electrodes is significantly better. As shown in **Fig. 4.21**, the ALD TiO_2-coated ZnO nanowires in a chopped scan tests show significant differences in the photocurrent between the light and dark conditions, implying increased photocurrent generations with increased voltages. Although the signal-to-noise is poor due to the low photocurrent, **Figure 4.21** also shows that photocurrent is generated at very low voltages (low onset voltage). Furthermore, the electrode performance is measured in the absence of any surface catalysts which can greatly increase the detectable photocurrents. These results suggest that the hydrothermal growth method for ZnO nanowires results in impurities and instabilities that reduce the performances of ZnO nanowires in the photocatalytic water splitting process. However, these instabilities have been shown to be alleviated by the coating of the TiO_2 layer.

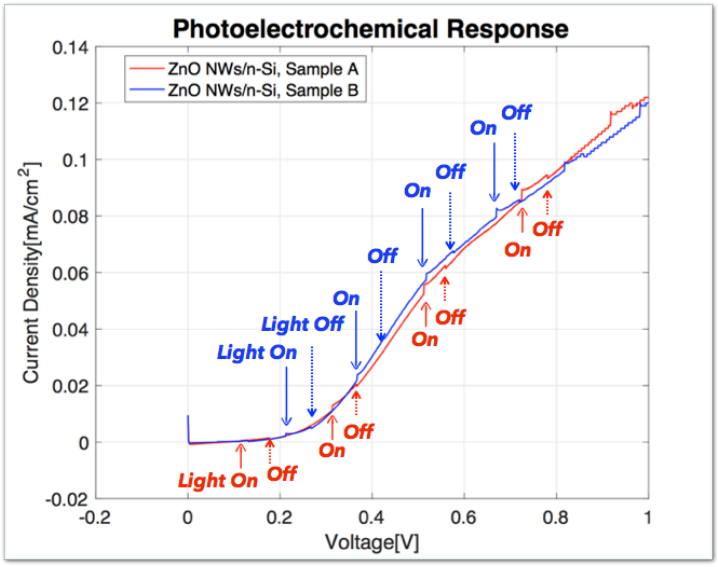

Figure 4.20 Photoelectrochemical responses of ZnO nanowires grown by the hydrothermal method.

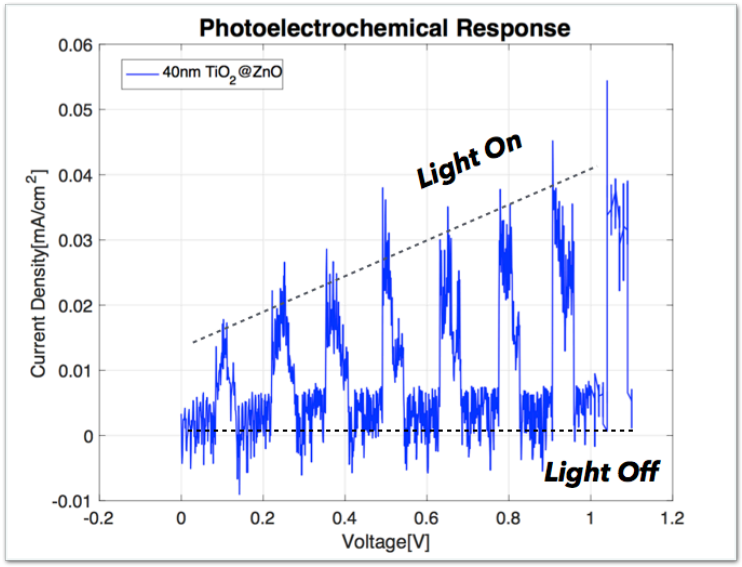

Figure 4.21, Photoelectrochemical response of the ZnO nanowires with coated TiO_2 layer using the hydrothermal and ALD deposition.

A thin TiO_2 shell material around the single-crystalline ZnO, as opposed to the bulky TiO_2 material, is the key concept to improving the photocatalytic performance. Since the ALD TiO_2 process deposits polycrystalline TiO_2, grain boundaries of the TiO_2 layer act as potential recombination sites to make the TiO_2 coating susceptible to low performance as a PEC electrode. In contrast, the ZnO nanowires are single-crystalline and are less vulnerable to recombination sites. Nevertheless, by limiting the TiO_2 to a 40nm coating thickness on the ZnO nanowire, the

travel distance of minority carriers is greatly reduced to promote better conductivity and reduce unwanted recombination.

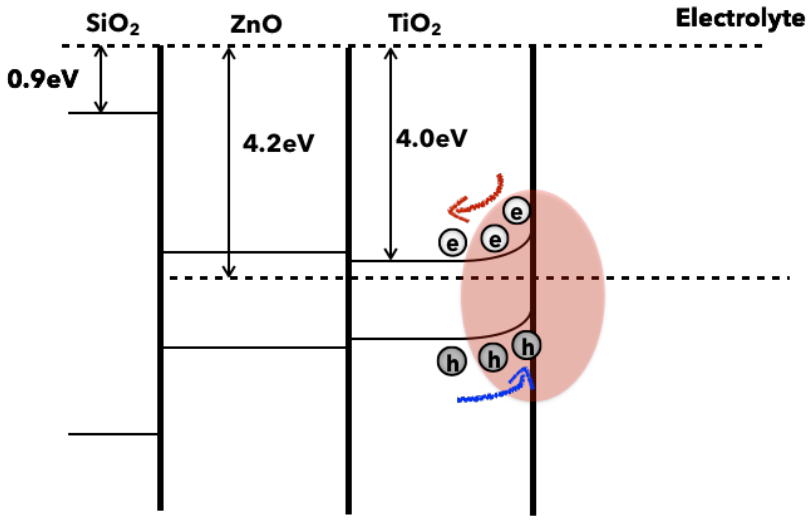

Figure 4.22, The band gap structure of the TiO_2/ZnO nanowires.

As shown in **Fig. 4. 22**, the theoretical band gap of TiO_2 is thought to encompass that of ZnO. Though the potential difference that electrons must overcome to transfer from TiO_2 into ZnO is small, electrons can still build-up at the semiconductor-semiconductor junction. However, the measurable photocurrent at low bias voltages indicate that the electron build-up does not significantly impede the detectable photocurrents. This could be due to the effect of quantum confinement: the phenomenon of band gap widening with decreasing thickness. In this case, the band gap of ZnO relative to TiO_2 is smaller such that the generated photoelectrons in TiO_2 would not experience the build-up of electrons (and subsequent recombination) at the junction.

4.8. Summary

High aspect-ratio and vertically ordered ZnO nanowires as long as 10 μm and less than 50 nm in diameter have been successfully synthesized with the conformal coating of a thin TiO_2 layer for applications in the solar-powered hydrogen (H_2) gas harvester. The hybrid hydrothermal and ALD process is used to achieve high aspect ratio and high quality nanowire arrays. Both the surface morphology and phase structure are analyzed to confirm that the TiO_2-coated ZnO nanowires are well constructed. The photoelectrochemical responses of synthesized nanowires are measured to investigate their performances as hydrogen gas harvesters. Nanowires with the coating of TiO_2 demonstrate improved stability over the bare ZnO nanowires in the photocatalysis tests with improved bias voltage. Results show that geometry and high quality nanowires could enhance the chemical stability but also lower the bias voltage for the generations of photocurrents.

4.9. References

[1] B. D. James, G. N. Baum, J. Perez, and K. N. Baum, "Technoeconomic Analysis of Photoelectrochemical (PEC) Hydrogen Production," *DOE Contract Number GS-10F-009J*, vol. 22201, no. December, pp. 1–128, 2009.

[2] A. FUJISHIMA and K. HONDA, "Electrochemical Photolysis of Water at a Semiconductor Electrode," *Nature*, vol. 238, no. 5358, pp. 37–38, 1972.

[3] T. Bak, J. Nowotny, M. Rekas, and C. C. Sorrell, "Photo-electrochemical hydrogen generation from water using solar energy," *Int. J. Hydrogen Energy*, vol. 27, no. 2002, pp. 991–1022, 2002.

[4] G. K. Mor, K. Shankar, M. Paulose, O. K. Varghese, and C. A. Grimes, "Enhanced photocleavage of water using titania nanotube arrays," *Nano Lett.*, vol. 5, no. 1, pp. 191–195, 2005.

[5] O. Khaselev and J. a Turner, "A Monolithic Photovoltaic-Photoelectrochemical Device for Hydrogen Production via Water Splitting R EPORTS A Monolithic Photovoltaic-Photoelectrochemical Device for Hydrogen Production via Water Splitting," *Science (80-.).*, vol. 280, pp. 425–427, 1998.

[6] M. Ni, M. K. H. Leung, D. Y. C. Leung, and K. Sumathy, "A review and recent developments in photocatalytic water-splitting using TiO2 for hydrogen production," *Renew. Sustain. Energy Rev.*, vol. 11, no. 3, pp. 401–425, 2007.

[7] A. Paracchino, V. Laporte, K. Sivula, M. Grätzel, and E. Thimsen, "Highly active oxide photocathode for photoelectrochemical water reduction," *Nat. Mater.*, vol. 10, no. 6, pp. 456–461, 2011.

[8] R. van de Krol and M. Grätzel, *Photoelectro-chemical Hydrogen Production*. Springer, 2012.

[9] C. A. Grimes, O. K. Varghese, and S. Ranjan, *Light, Water, Hydroge*. Springer, 2007.

[10] I. Roger, M. A. Shipman, and M. D. Symes, "Earth-abundant catalysts for electrochemical and photoelectrochemical water splitting," *Nat. Rev. Chem.*, vol. 1, no. 1, p. 3, 2017.

[11] S. M. Sze and K. K. Ng, *Physics of Semiconductor Devices*, 3rd ed. New York: Wiley, 2007.

[12] R. F. Pierret, *Semiconductor Device Fundamentals*, 2nd ed. Addiiton Wesley, 1996.

[13] J. O. Bockris, A. K. N. Reddy, and M. E. Gamboa-Aldeco, *Modern Electrochemistry 2A - Fundamentals of Electrodics*. New York: Springer, 2001.

[14] J. Willkomm, K. L. Orchard, A. Reynal, E. Pastor, J. R. Durrant, and E. Reisner, "Dye-sensitised semiconductors modified with molecular catalysts for light-driven H_2 production," *Chem. Soc. Rev.*, vol. 45, no. 1, pp. 9–23, 2016.

[15] J. R. Chelikowsky and M. L. Cohen, "Nonlocal pseudopotential calculations for the electronic structure of eleven diamond and zinc-blende semiconductors," *Phys. Rev. B*, vol. 14, no. 2, pp. 556–582, 1976.

[16] E. Stoyanov, F. Langenhorst, and G. Steinle-Neumann, "The effect of valence state and site geometry on Ti L3,2 and O K electron energy-loss spectra of TixOy phases," *Am. Mineral.*, vol. 92, no. 4, pp. 577–586, 2007.

[17] K. Seo, M. Wober, P. Steinvurzel, E. Schonbrun, Y. Dan, T. Ellenbogen, and K. B. Crozier, "Multicolored vertical silicon nanowires," *Nano Lett.*, vol. 11, no. 4, pp. 1851–1856, 2011.

[18] L. K. Van Vugt, B. Zhang, B. Piccione, A. A. Spector, and R. Agarwal, "Size-dependent waveguide dispersion in nanowire optical cavities: Slowed light and dispersionless guiding," *Nano Lett.*, vol. 9, no. 4, pp. 1684–1688, 2009.
[19] M. F. Weber and M. J. Dignam, "Splitting water with semiconducting photoelectrodes-Efficiency considerations," *Int. J. Hydrogen Energy*, vol. 11, no. 4, pp. 225–232, 1986.
[20] J. R. Bolton, S. J. Strickler, and J. S. Connolly, "Limiting and realizable efficiencies of solar photolysis of water," *Nature*, vol. 316, no. 6028, pp. 495–500, 1985.
[21] T. Hisatomi, J. Kubota, and K. Domen, "Recent advances in semiconductors for photocatalytic and photoelectrochemical water splitting," *Chem. Soc. Rev.*, vol. 43, no. 22, pp. 7520–7535, 2014.

Chapter 5. Annealing Temperature Effects on Solution Processed SnO_2 Thin Film Transistors (TFTs)

5.1. Introduction

Thin film transistors (TFTs) are the most fundamental electronic components in virtually all informative display devices ranging from smart phones to large flat TVs. TFT is a kind of field effect transistors (FETs) where the main application is large scale display devices with low processing temperatures. On the other hand, FETs are targeted for high performance analog circuit devices. TFTs consist of a semiconductor channel layer, a dielectric layer as the gate insulator and conductive three terminals (gate, source and drain). In TFTs, the current between source and drain electrodes (I_{DS}) can be controlled by varying the electrical potential between the gate and the source (V_{GS}). Unlike FETs, the channel is formed at the dielectric/semiconductor interface by inducing free carrier accumulation whereas the inversion layer due to the minority carriers is formed for the FET [1]. **Fig. 5.1** shows the schematic diagram of FET and TFT devices.

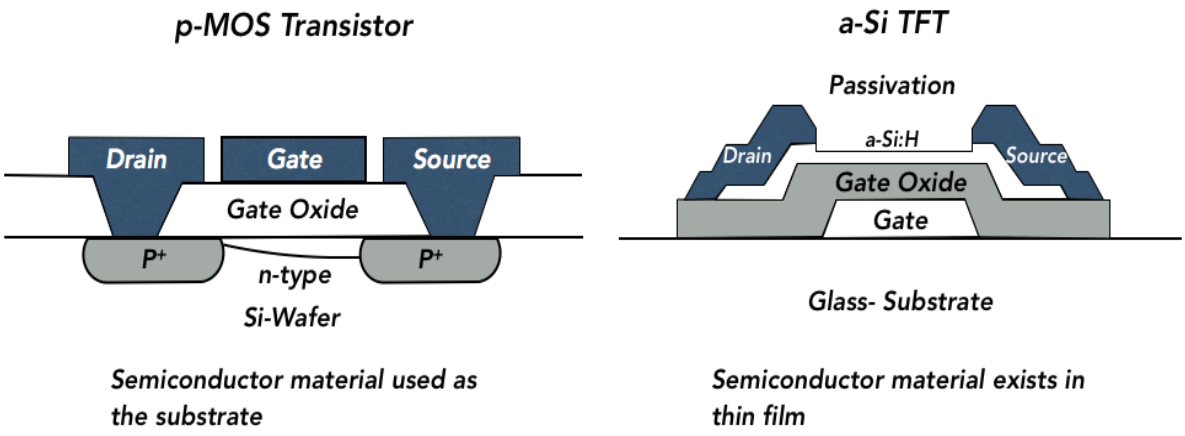

Figure 5.1 The simplified cross-sectional views of the p-bulk (n-channel) FET structure (left) and a typical bottom gate TFT (right).

TFTs based on hydrogenated amorphous silicon (a-Si:H) [2] have dominated the display market where the active matrix liquid crystal display (AMLCD) is the main product line. Even though its electron mobility is approximately 1.0 cm^2/Vs, this is sufficient to operate the switching of AMLCD devices. However, the low mobility is not suitable for devices that require high speed and large current applications such as pixel transistors for organic light-emitting diode (OLED) displays or column driving transistors in display devices. **Fig. 5.2** shows the TFTs in display devices.

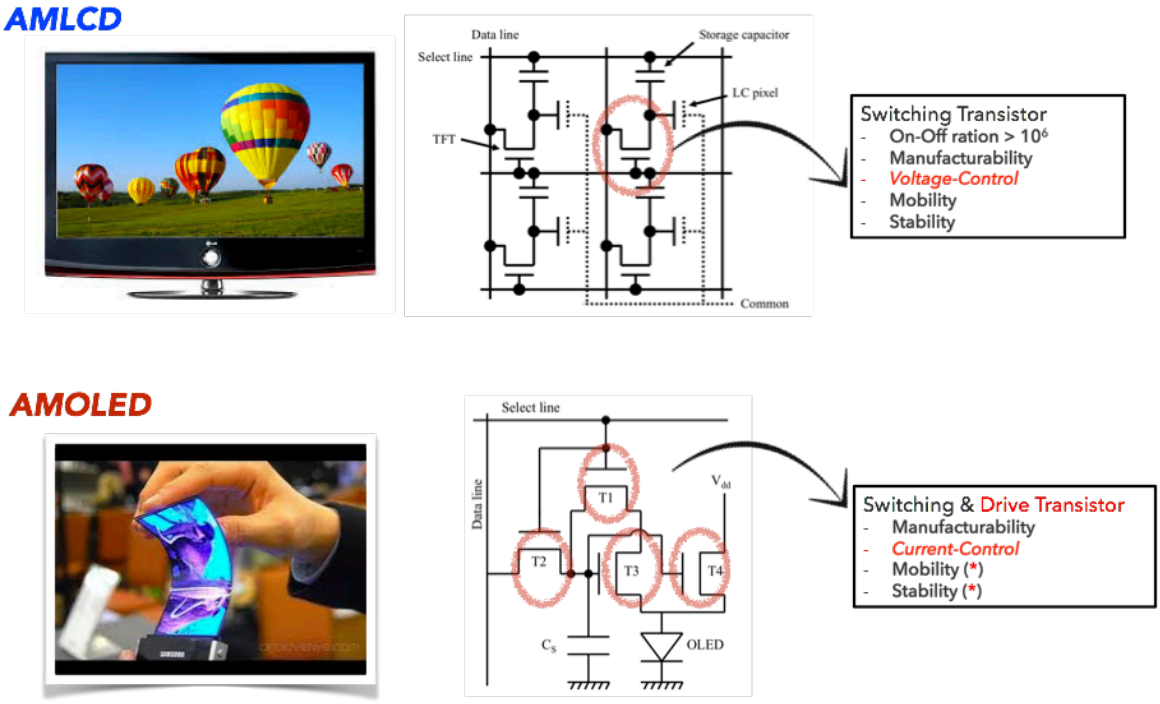

Figure 5.2 TFTs for AMLCD and AMOLED display devices as switching transistors and driving transistors.

In order to overcome this low mobility issue of a-Si:H TFTs, a poly-Si based technology has been introduced for high performance devices. In general, poly-Si deposition processes require high temperature and long process time which are not suitable for large area display devices with glass substrates [3], [4]. However, short pulsed laser techniques enable the melting and solidification of a-Si:H films with improved electron mobility by changing their crystallinity and grain sizes [5]–[9]. By irradiating an a-Si thin film with a pulsed laser tens of times, localized heating is generated in a limited depth of the a-Si films to induce recrystallization of a-Si. Even though this low temperature poly silicon (LTPS) is a good candidate for TFTs in modern display devices, its non-uniformity and high cost due to the recrystallization process by excimer laser annealing (ELA) and complicated process steps limit its usages only for small sized display devices. **Fig. 5. 3** illustrates the fabrication process of co-planar structure with LTPS TFTs.

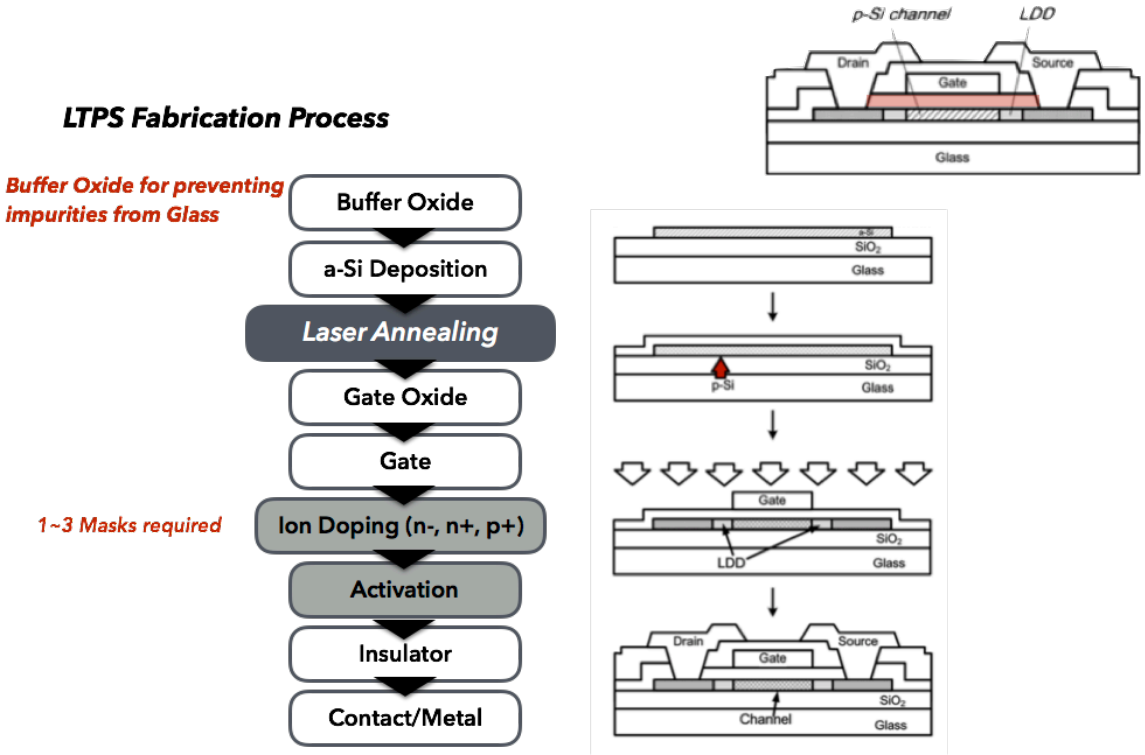

Figure 5.3 Typical fabrication process of LTPS TFTs with a co-planar top gate structure.

Recently, research on the oxide semiconductor has gained a lot of attention to overcome the issues in LTPS TFTs. For example, the first In-Ga-Zn-O (IGZO) TFT was reported in late 2014; extensive research based on IGZO has been conducted and many prototype displays have been demonstrated [10]. Even though the off-current of the oxide TFTs is relatively high (~10^{-11}A), their outstanding electrical properties and low fabrication cost have been repeatedly demonstrated [11], [12]. Furthermore, some companies have already begun a mass production of display panels by using indium-gallium-zinc oxide (IGZO) TFTs. Among the various fabrication processes, the solution-based process has become attractive due to its simple and low-cost process with high throughput.

In this research, we present tin oxide (SnO_2) TFTs based on a fabrication process using multiple spin-coating steps. In order to obtain a gate modulation characteristic of the solution processed SnO_2 TFT, various annealing conditions are investigated by changing both annealing time and temperature; their effects on the performances of TFTs is observed. In addition, we analyze the surface morphology using field effect scanning microscopy (FESEM) and investigate the bonding states of the thin films by X-ray photoelectron spectroscopy (XPS).

5.2. Process overview

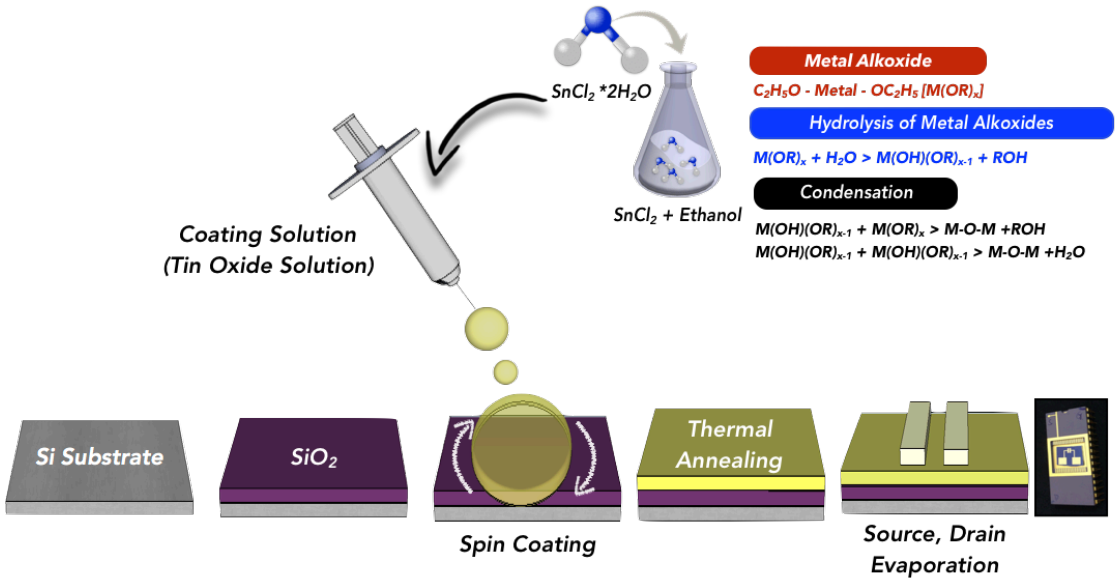

Figure 5.4 Schematics of solution process for making SnO_2 TFTs.

Fig. 5.4 illustrates the schematic of the fabrication process for the solution-processed tin oxide (SnO_2) TFTs. Similar to the previous chapters, the fabrication process starts by dissolving 0.001 mole of tin (II) chloride dehydrate ($SnCl_2$-$2H_2O$) precursor into the 10 ml of ethanol. Next, the 10 wt.% of tin chloride coating solution is prepared after hydrolysis and condensation of tin chloride alkoxide. A 100 nm-thick silicon dioxide (SiO_2) gate dielectric is deposited using the thermal oxidation process and the tin chloride coating solution is deposited on top of SiO_2/n-Si and p-Si substrates by using the multiple spin-coating method. Each time, a ~10 nm-thick layer is coated onto the SiO_2/Si substrate at 3000 rpm for 30 seconds and dried on top of a hot plate at 285º for 1 minute. The total thickness of SnO_2 thin films is controlled by repeating this spin coating process and measured using an Alpha-step IQ surface profiler. After depositing the final layer, a thermal annealing process is conducted in an air environment (Thermo Electron Corp., model Lindberg/Blue M® three-zone tube) to densify the films by decomposing the precursors and removing the organic solvents. Nonreactive metal (Au) is used as the source-drain contact and chromium is chosen as the adhesion layer between the Au electrode and the silicon substrate. To minimize the contamination of the semiconductor layer, we introduced an e-beam evaporation using a stencil mask without using the photoresist and developing process. The source-drain electrodes are defined with channel length ranging from L = 50 µm to 200 µm and the channel width of W = 500 µm to 2000 µm. The design of the stencil mask and the optical image of the final TFT device are shown in **Fig. 5. 5**.

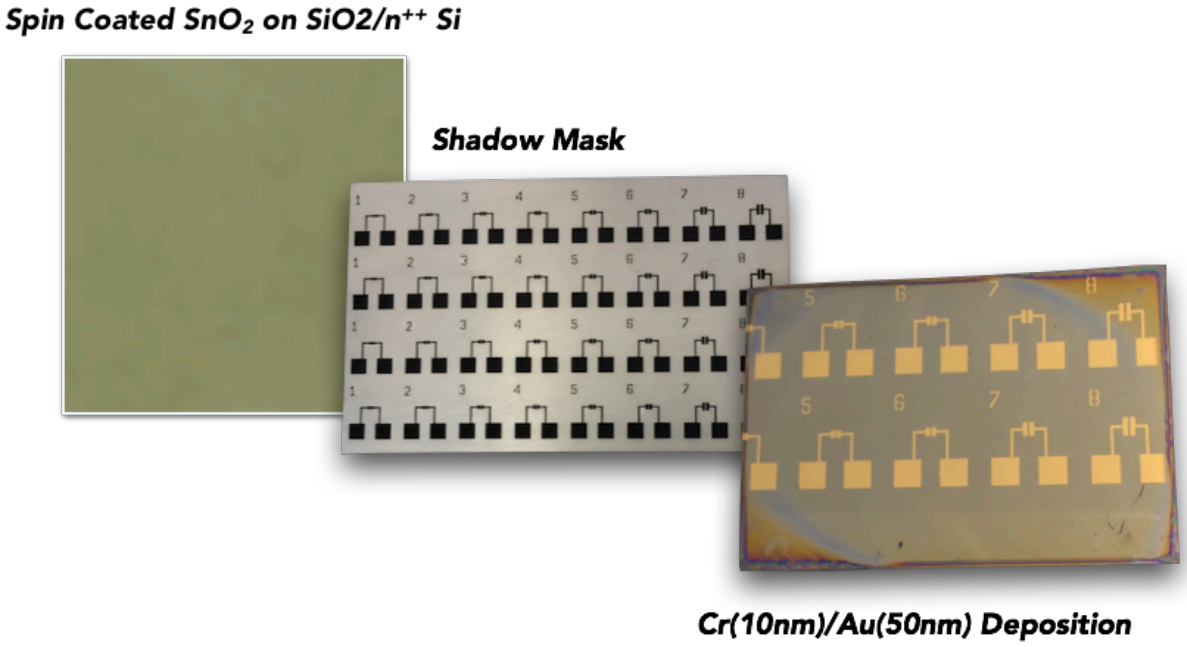

Figure 5.5 Optical images of spin coated tin oxide on top of SiO_2/n-Si substrate, laser processed shadow mask, and Au electrodes patterning on the semiconductor layer.

5.3. Material characterization

The surface morphology of the solution processed SnO_2 layers is analyzed using a field emission scanning electron microscopy (FESEM). As the thermal annealing duration increases (5 minutes, 10 minutes, and 20 minutes) and the temperature is fixed at 400ºC, the particle size slightly reduces with more densely packed surface morphology (**Fig. 5.6**). This surface morphology trend is consistent with a solution processed ATO sample in the previous chapter. This observation describes that the change in surface morphology is not coming from the grain size differences but from the densification of SnO_2 thin films. This results in higher conductivity for longer annealing duration and is verified by the electrical performance measurements.

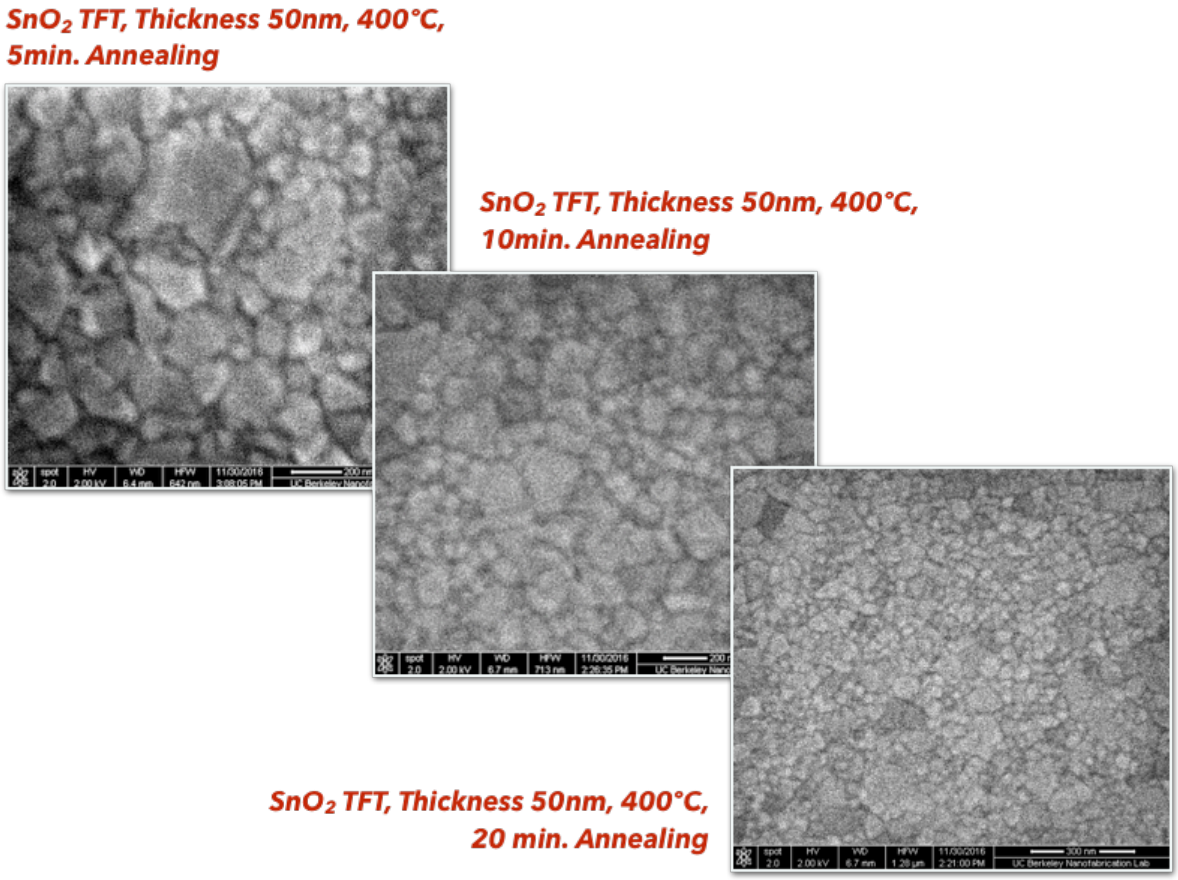

Figure 5. 6 SEM images of SnO_2 thin films annealed at 400ºC with different annealing duration.

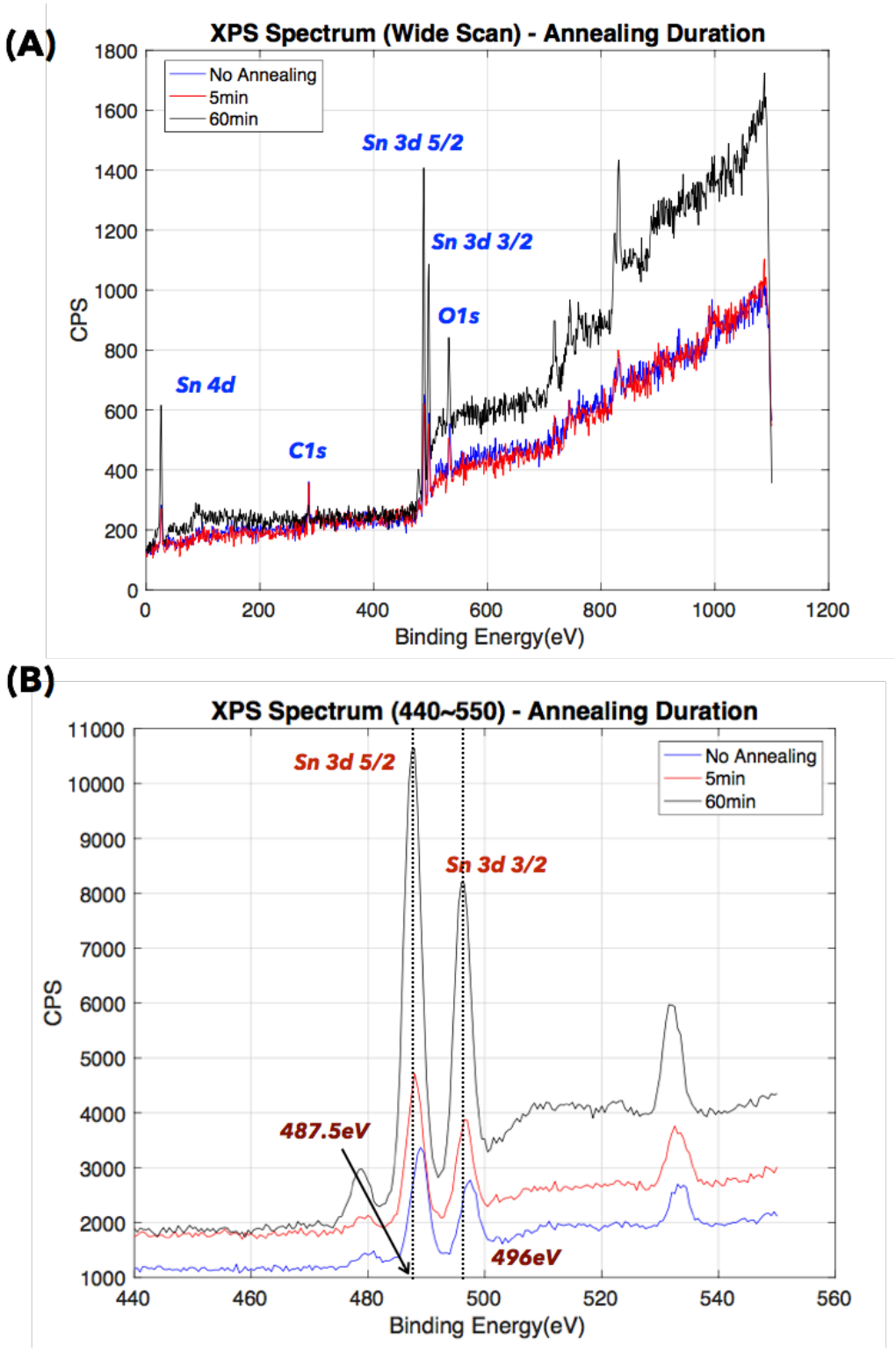

Figure. 5.7 (A) XPS survey scan of ATO thin films annealed at 400ºC with different annealing duration, **(b)** XPS core-level spectra of Sn 3d showing spin–orbit splitting.

X-ray photoelectron spectroscopy (XPS) is used to analyze the chemical compositions and bonding states. **Fig. 5.7(A)** shows the wide-energy range scan consisting of tin, oxygen, and carbon (surface impurities) peaks for the solution processed SnO_2 samples annealed at 400ºC with various annealing durations in a furnace. The binding energy scales have been referenced to the C1s orbital at 284.6 eV with the margin of error of ±0.6 eV. **Fig. 5.7(B)** also shows the spin–orbit splitting and chemical shift of the Sn 3d core levels. The intensity peaks are found at 487.5 eV for Sn 3d5/2 and 496 eV for Sn3d3/2 and this 8.5 eV of spin–orbit split for the Sn 3d core levels agrees well with those found in the literature. The material characterizations using XPS indicates that $Sn^{+4}(SnO_2)$ is successfully synthesized from the $Sn^{+2}(SnO)$ by confirming the 8.5eV of spin-orbit splitting in the Sn3d orbitals.

5.4. TFT performance characterizations

The electrical characteristics of TFTs were measured using a HP 4156A precision semiconductor parameter analyzer. The TFT parameters in this work are extracted from the third cycle of transfer curve after the device behavior has stabilized. **Fig. 5.8** shows the representative transfer characteristic curves of SnO_2 TFTs at V_D = 1.5 V, 2.0 V, and 2.5 V as a function of V_G sweeping from -20 V to 20 V. The transfer characteristic curves clearly indicate that not only the annealing temperature but also annealing time affect the gate modulation characteristics. TFT annealed at 500ºC for 30 minutes shows poor electrical performance because there is no on-off switching behavior due to the high electrical conductivity of the material. The measurement results also reveal that the thermal annealing time in the furnace is an important factor to obtain the desirable gate modulation property of TFTs. In this work, a thin film with 4 minutes of thermal annealing at 400ºC presents the best gate modulation characteristics for spin-coated tin oxide TFTs.

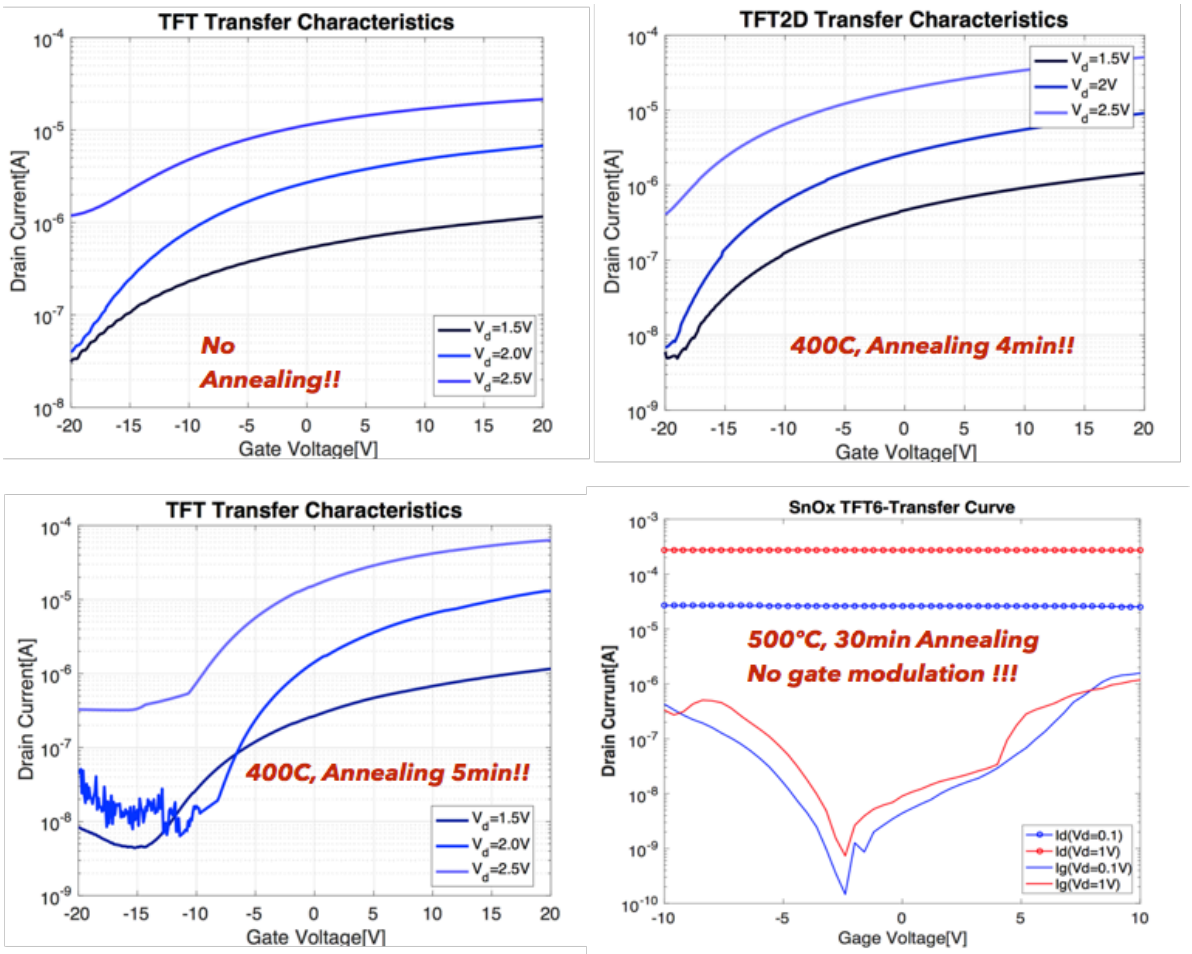

Figure 5.8 Effects of annealing temperature and duration on the gate modulation characteristics of solution-processed SnO_2 TFTs.

The field effect mobility (μ_{lin} for the linear region, μ_{sat} for the saturation region) of TFTs are extracted from the transfer characteristics curve and according to the reported equations [12], [13].

$$\mu_{lin} = \frac{L}{WC_iV_{DS}}\left(\frac{\partial I_D}{\partial V_G}\right) \tag{5-1}$$

$$\mu_{sat} = \frac{2L}{WC_i}\left(\frac{\partial \sqrt{I_D}}{\partial V_G}\right)^2 \tag{5-2}$$

where C_i is the dielectric capacitance per unit area and V_G is the applied gate voltage; L and W are the channel length and width, respectively; V_{DS} is the applied potential between drain to source; and I_D is the drain-to-source current.

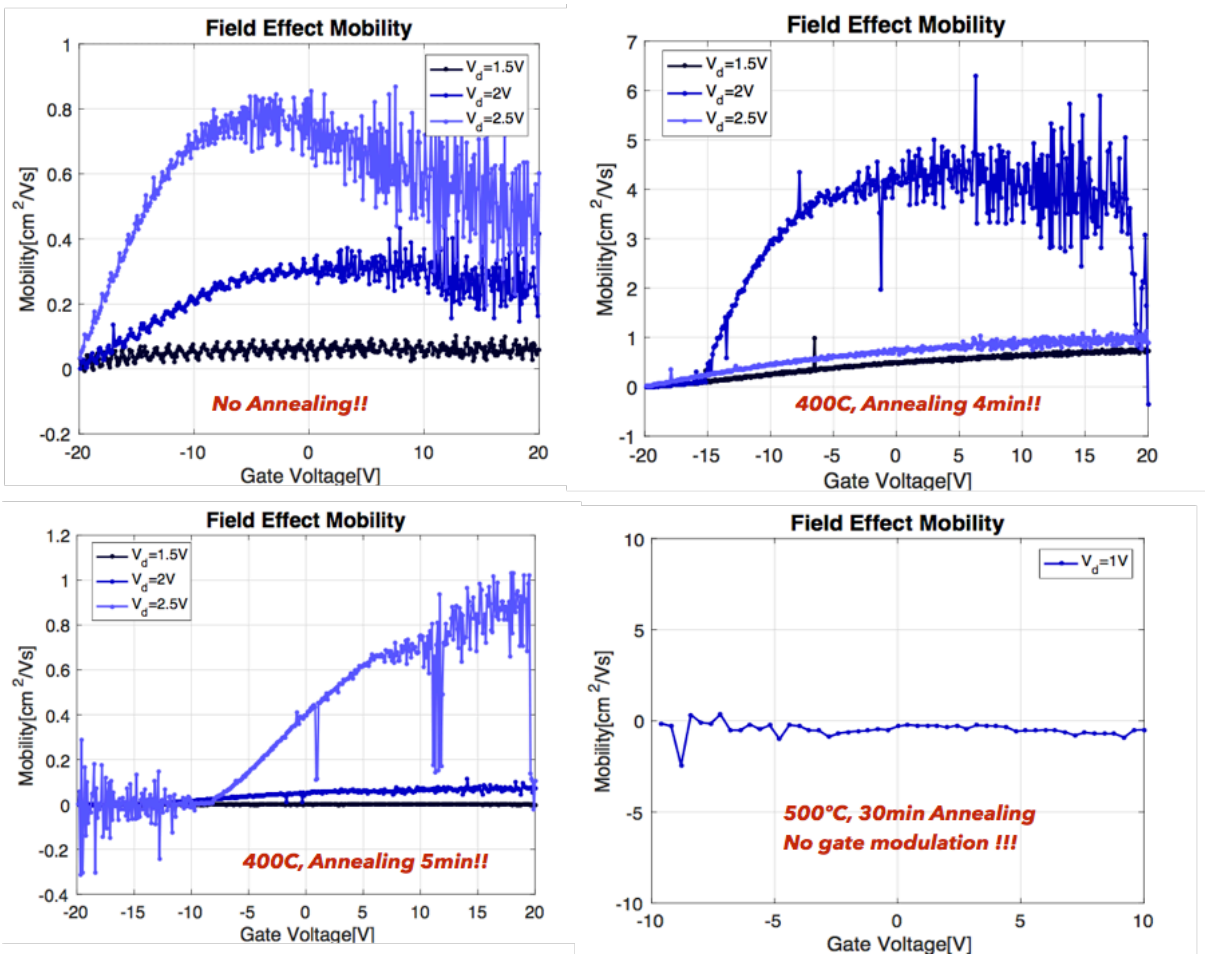

Figure 5.9 Effects of annealing temperature and duration on the field effect mobility characteristics of solution-processed SnO_2 TFTs.

Fig. 5.9 shows calculated field effect mobility from the transfer characteristics curves. TFTs annealed at 400ºC for 4 min exhibit the best performance than those from other TFT samples and the maximum value from the extracted field effect mobility is around 6.3 cm^2/Vs when V_{DS} is 2 V. This value is 6~7 times larger than that of a typical a-Si:H TFT device. This result also shows that both annealing temperature and duration are important factors for the mobility of TFTs.

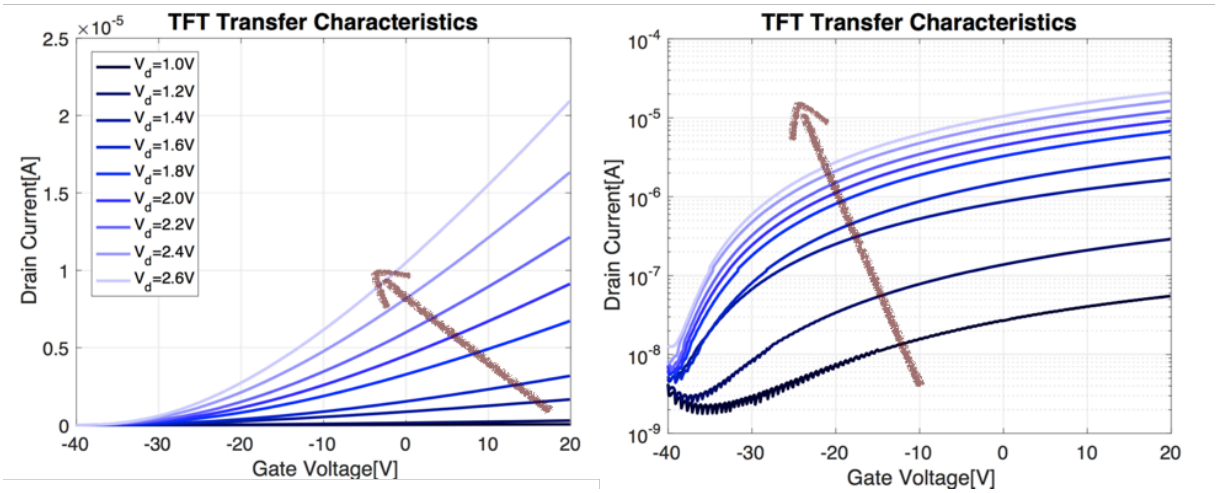

Figure 5. 10 Transfer characteristic curves of SnO_2 TFTs.

In order to find better gate modulation characteristics of TFTs, drain voltage (V_D) was swept with closely spaced intervals from 1.0 V to 2.6 V. **Fig. 5.10** presents transfer characteristic (I_D-V_G) curves of a TFT with a gate bias sweeping from -40 V to 20 V. The 50 nm-thick SnO_2 channel layer on top of 90 nm-thick SiO_2 is annealed at 400ºC for 4 min under ambient air with the channel length and width of 60 µm and 600 µm respectively. When the drain bias increases from 1.0 V to 2.6 V, the drain current also increases. The arrow indicates the direction of increasing V_{DS}. However, when the applied drain voltage is beyond 1.8 V, the increment of drain current becomes smaller. The measured on-off ratio of TFTs are from 10^2 to 10^4 and the best on-off ratio of 10^4 is measured when the drain voltage is 2.05 V as shown in **Fig. 5. 11**.

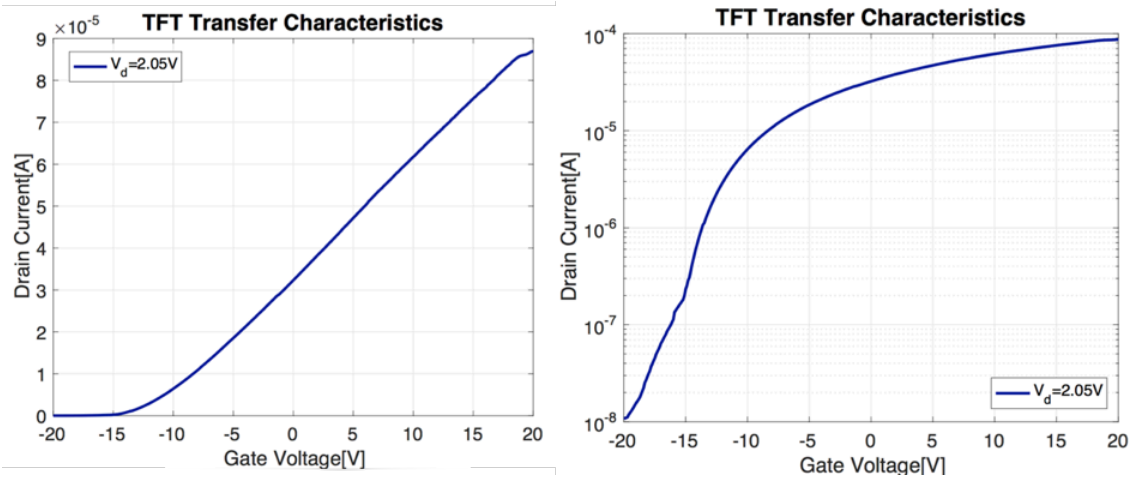

Figure 5. 11 Transfer characteristic curves of SnO_2 TFT in a linear scale and log scale showing the 10^4 on-off ratios.

Unlike the normal output characteristics of TFTs in which linear and saturation regions exist according to V_D as shown in **Fig. 5.12**, no saturation is found in the V_{DS}-I_D characteristic curves for the TFTs. Furthermore, sweeping the V_G value also does not significantly change the drain-to-source current. More interestingly, anomalous large rectification ratio (~10^9) of diode-like behavior is observed in the output characteristic curves, while they do not exhibit the hard saturation and the gate voltage control of the channel conductivity. It is observed that I_D is boosted anomalously when the V_{DS} is between 2.5 V and 3 V whereas steady increase of I_D occurs in other regions.

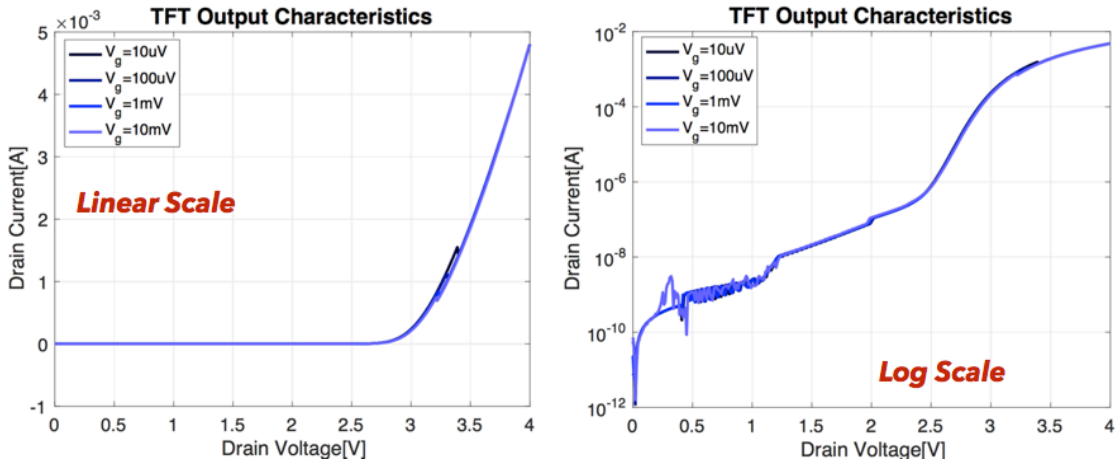

Figure 5.12 Output characteristic curves of SnO_2 TFT in a linear scale and log scale showing anomalous diode-like behaviors with a large rectification ratio of 10^9.

There are a few possible ways to explain this anomalous phenomenon. First, there is a Schottky barrier between the Au electrode and SnO_2 semiconductor layer. When the work function of metal (Au) electrode is bigger than that of the n-type semiconductor layer (SnO_2), electrons can transfer from the semiconductor to the metal. This charge transfer is due to the formation of band bending of the conduction and the valence band edges near the interface. Consequently, two electronic barriers, Schottky barrier height (φ_{BN}) and the built-in potential (V_{BI}), are established at the interface as shown in **Fig. 5.13**. This energy barrier will impede the carrier transfer in the opposing directions across the interface and be characterized by the rectifying current-voltage curves.

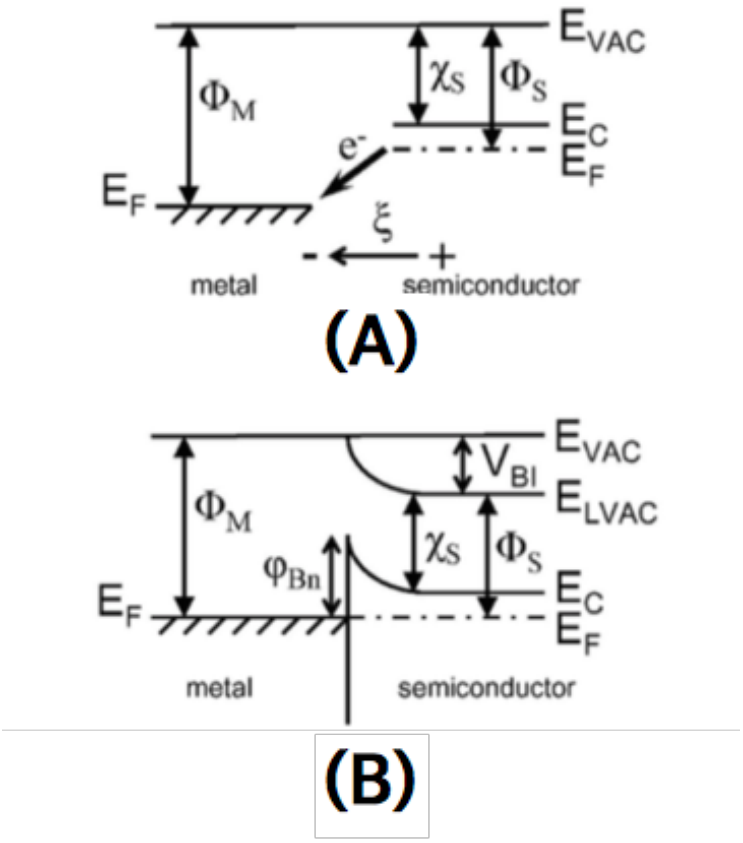

Figure 5.13 Energy band diagrams for: (A) before the metal and semiconductor contact; (B) the corresponding Schottky barrier band structure after the contact. Image taken from [14]

Another possible reason is that the current flowing from the source to drain can be shunted by a back interface. When the gate bias is applied to the insulator, a drain current can flow due to the accumulation charges at the channel layer and the passivation layer ($I_{D,\ Surface}$) but a shunted drain current can also flow, due to the induced carriers at the interface ($I_{D,\ interface}$), between the channel layer and gate insulator in the semiconductor layer as shown in **Fig. 5.14**. If the low resistance of shunt pass exists between the source and the drain regions, the current flow can be anomalously boosted.

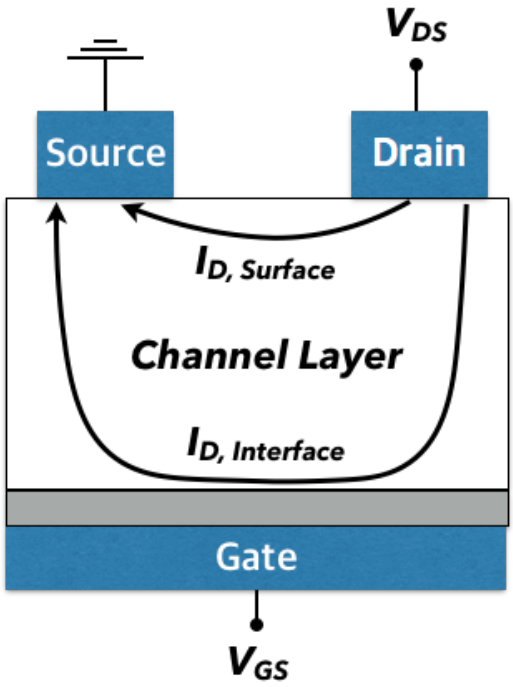

Figure 5. 14 Schematic of the bottom gate TFT describing the current paths that contribute to the overall current of the device. Image taken from [14]

Localized tail states and deep states in the band gap of the semiconductor are possible reasons for this anomalous current increase. When electrons are trapped in these trap states, they can be released by applying enough energy to the electrons and, thereby the drain current can be boosted. Even though there are several possible mechanisms to explain this phenomenon, there are unclarified points regarding this anomalous current and additional experiments and investigations are needed to investigate the exact mechanism.

5.5. Summary

In this chapter, we introduce the basics of thin film transistors and various types of TFT materials such as a-Si:H, poly-Si and metal oxide materials. We successfully fabricate the SnO_2 TFTs using solution process with the multiple spin-coating steps. A parametric study has been conducted to determine the influence of the film thickness, annealing temperature and annealing time on electrical performance (transfer and output characteristics). It is found that the samples annealed at 400ºC for 4 min have the best performance in our prototype tests. The surface morphologies and the chemical bonding states are investigated by using FESEM and XPS. The extracted field effect mobility of the solution-processed SnO_2 TFTs is around 6.3 cm^2/Vs under the V_{DS} at 2 V.

5.6. References

[1] A. C. Tickle, *A New Approach to Microelectronics*. New York: Wiley, 1969.

[2] P. G. le Comber, W. E. Spear, and A. Ghaith, "Amorphous-silicon field-effect device and possible application," *Electron. Lett.*, vol. 15, no. 6, pp. 179–181, 1979.

[3] S. D. Brotherton, "Polycrystalline silicon thin film transistors," *Semicond. Sci. Technol.*, vol. 10, pp. 721–738, 1995.

[4] Y. Kuo and P. M. Kozlowski, "Polycrystalline silicon formation by pulsed rapid thermal annealing of amorphous silicon," *Appl. Phys. Lett.*, vol. 69, no. 8, pp. 1092–1094, 1996.

[5] J. S. Im, R. S. Sposili, and M. A. Crowder, "Single-crystal Si films for thin-film transistor devices," *Appl. Phys. Lett.*, vol. 70, no. 25, pp. 3434–3436, 1997.

[6] J. S. Im, H. J. Kim, and M. O. Thompson, "Phase transformation mechanisms involved in excimer laser crystallization of amorphous silicon films," *Appl. Phys. Lett.*, vol. 63, no. 14, pp. 1969–1971, 1993.

[7] J. S. Im and H. J. Kim, "On the super lateral growth phenomenon observed in excimer laser-induced crystallization of thin Si films," *Appl. Phys. Lett.*, vol. 64, no. 17, pp. 2303–2305, 1994.

[8] J. S. Im, M. A. Crowder, R. S. Sposili, J. P. Leonard, H. J. Kim, J. H. Yoon, V. V. Gupta, H. Jin Song, and H. S. Cho, "Controlled Super-Lateral Growth of Si Films for Microstructural Manipulation and Optimization," *Phys. Status Solidi*, vol. 166, no. 2, pp. 603–617, 1998.

[9] R. S. Sposili and J. S. Im, "Sequential lateral solidification of thin silicon films on SiO_2," *Appl. Phys. Lett.*, vol. 69, no. 19, pp. 2864–2866, 1996.

[10] K. Nomura, H. Ohta, A. Takagi, T. Kamiya, M. Hirano, and H. Hosono, "Room-temperature fabrication of transparent flexible thin-film transistors using amorphous oxide semiconductors," *Nature*, vol. 432, no. 7016, pp. 488–492, 2004.

[11] B. Du Ahn, H.-J. Jeon, J. Sheng, J. Park, and J.-S. Park, "A review on the recent developments of solution processes for oxide thin film transistors," *Semicond. Sci. Technol.*, vol. 30, no. 6, p. 64001, 2015.

[12] E. Fortunato, P. Barquinha, and R. Martins, "Oxide semiconductor thin-film transistors: A review of recent advances," *Adv. Mater.*, vol. 24, no. 22, pp. 2945–2986, 2012.

[13] M.-G. Kim, M. G. Kanatzidis, A. Facchetti, and T. J. Marks, "Low-temperature fabrication of high-performance metal oxide thin-film electronics via combustion processing," *Nat. Mater.*, vol. 10, no. 5, pp. 382–388, 2011.

[14] J. F. Wager, D. A. Keszler, and R. E. Presley, *Transparent Electronics*. Springer, 2008.

Chapter 6. Conclusions and Future Work

6.1. Conclusions

Metal oxide materials have attracted much interest due to their versatility and simple fabrication process. Their potential applications can be applied in various fields such as opto-electronic devices, renewable energy products, and thin film transistors. In this dissertation, we demonstrate several applications of metal oxides with cost-effective fabrication processes.

First, we successfully fabricate a highly conductive (~15000 S/m) and optically transparent (~95%) ATO thin film using the solution-based process. For making high quality ATO thin films, the multiple spin-coating method is introduced. A parametric study has been performed on four key process parameters: doping concentration, thickness, ambient gas and temperature to achieve high electrical conductivity and transparency. Studies on the surface morphology, crystallinity, electrical, and optical properties of ATO films have also been conducted. The XPS results confirmed that the minimum annealing temperature for the formation of the Sb^{+5} species in the Sn^{+4} lattices is between 300ºC and 400ºC. We also demonstrate that solution-processed TCOs exhibits improved mechanical properties. The elastic modulus of the solution processed ATO films is investigated by using the nano-indentation tests and determined to be around 35 GPa, about one third of the elastic modulus of the commercial vacuum-processed ITO thin films. Results from the 3D finite element analysis show about 4x larger deflection and 3.3x smaller maximum principal stress for the solution-processed ATO samples as compared with those of vacuum-processed ITO samples under the same four-point bending simulations. As such, the solution-processed ATO films have the potential applications in transparent, conductive electronic components with improved mechanical flexibility and stress.

A different metal oxide material is introduced in Chapter 4 for the renewable fuel (H_2) production. We successfully synthesized high aspect-ratio, vertically ordered ZnO nanowires as long as 10 μm and less than 50 nm in diameter by using a hydrothermal process. These nanowires are coated with a layer of TiO_2 using ALD for use as a solar-powered hydrogen gas harvester. Nanowires with a layer of TiO_2 coating demonstrate improved stability over bare ZnO nanowires during the photocatalytic process with lower bias voltages. Results show that geometric design and high quality nanowires can enhance chemical stability but also improve the bias voltage to yield better photocurrents.

Finally, SnO_2-based TFTs for the display devices have been developed by using a solution-based process with a multiple spin-coating method. In order to obtain better gate modulation properties of TFTs, a parametric study has been performed on the annealing temperature and duration. It is found that samples annealed at 400ºC for 5 minutes exhibit the best performance than other samples with different annealing conditions. The surface morphology and the chemical bonding states are investigated by using FESEM and XPS. The extracted field effect mobility of the solution-processed SnO_2 TFTs is around 6.3 cm^2/Vs under the condition with V_{DS} at 2 V.

6.2. Future work

The electrical conductivity of optically transparent ATO thin films is still lower than that of commercially available ITO thin films and the high process temperature is still too high for flexible electronics. This shortcoming can be further addressed by using laser induced local heating and catalysts. By scanning pulsed UV laser beam onto the thin films, the carrier mobility of the thin film can be improved by the rapid local melting and recrystallization. This pulsed laser technique can also minimize the thermal damage of the substrate because most of the energy is absorbed by the surface to make the fabrication process compatible with flexible electronics. In a solution process, the phase change of precursors from sols to gel-like phase is the most critical process which determines its electrical performances. Larger inter-connected structures can be formed at low temperature by using catalysts; the carrier mobility can be enhanced by the inter-aggregation.

In the work of high aspect-ratio and vertically ordered ZnO nanowire with the stabilization TiO_2 coating process for solar-powered hydrogen gas harvesters, enhanced stability and lower bias voltage have been achieved. However, the exact mechanism for these improvements require further studies. One possible direction is to look into the quantum confinement effects. For example, the spatial confinement of charge carriers to a volume that is less than their De Broglie wavelength can induce a widening of bandgap and decrease the required bias potential. Further investigation is required to have better understanding in this area.

The solution-processed SnO_2 TFTs have been successfully demonstrated in chapter 5, there are issues to be further addressed. The TFT structure in this work is the simple bottom gate structure without gate and channel patterning. As such, the drain current can be overestimated due to the fringe fields between the source-drain electrodes. In order to measure the precise electrical performance, the gate and channel pattering will be required. Another issue is the long-term stability. To guarantee the reliability of the TFTs, passivation layer on the channel layer is critical. Negative and positive bias temperature instabilities must also be tested to secure their stability over time.